Title
Laboratory Experiments on Arched Magnetized Plasmas

Author
Sklodowski, Kamil Daniel

Publication Date
2023

Peer reviewed|Thesis/dissertation

UNIVERSITY OF CALIFORNIA
Los Angeles

Laboratory Experiments on Arched Magnetized Plasmas

A dissertation submitted in partial satisfaction
of the requirements for the degree
Doctor of Philosophy in Physics

by

Kamil Daniel Sklodowski

2023

ABSTRACT OF THE DISSERTATION

Laboratory Experiments
on Arched Magnetized Plasmas

by

Kamil Daniel Sklodowski
Doctor of Philosophy in Physics
University of California, Los Angeles, 2023
Professor Troy A Carter, Chair

The arched plasma structures found throughout the Sun's atmosphere can significantly impact the heliosphere and Earth through eruptive events like solar flares and coronal mass ejections. Coronal loops and solar prominences are examples of arched plasmas on the Sun. In this dissertation, we study arched plasma structures in the laboratory setting relevant to those found in the Sun. The current understanding of mechanisms leading to eruptions and general dynamics of arched solar plasmas remains limited. This is primarily due to a lack of extensive in situ diagnostics and, thus, a heavy reliance on remote imaging. Through proper scaling of relative plasma parameters, we can investigate the dynamics of arched plasma phenomena in a laboratory to better understand what is happening in the Sun. This research aims to contribute knowledge to the field and allow for the formulation of reliable predictive models.

This experiment was designed with the primary goal of producing and studying arched magnetized, current-carrying plasma. It is achieved with a hot lanthanum hexaboride (LaB_6) cathode and cold copper anode plasma source operated in a vacuum vessel filled with a neutral Helium gas (up to 9 mtorr). Two magnetic fields are produced in this experiment, of which direction and

magnitude can be tailored to experimental goals. The first is an arched guiding magnetic field connecting the footpoints and guiding the plasma along the arch. The second is a horizontal overlying (ambient) magnetic field of uniform magnitude, directed perpendicular to the plane of the arch. A three-dimensional probe drive has been constructed for this work, allowing for automated in situ measurements of plasma parameters with high spatial resolution along the customizable grid. The probe drive control software was written in Python and integrated with the main data acquisition LabView software. The appropriate coordinate transformations between the probe tip position and the probe drive's motors were determined and integrated into the control software. We have built four diagnostic in situ probes (magnetic field, 2- and 3-tip Langmuir, Mach), resistant up to 700°C temperatures. This high temperature-resistant construction allows for measurements very close to the hot cathode source (up to 5 cm away). The probes were used along with two fast cameras to better understand phenomena in experiments presented here. We have carried out multiple arched plasma source maintenance and upgrade routines, improving its duty cycle and stability over the course of this work. A power supply control system was developed for both background and arched plasma source heaters. This system allowed us to gradually raise the heaters' current in an automated and remote fashion. All data analyses were conducted in Python using the Jupyter Notebook environment. An extensive library of data analysis functions and procedures resulting from this work is tailored to this setup.

One focus of this dissertation is the effects of a nearly horizontal overlying (strapping) magnetic field on the evolution and morphology of the arched magnetized plasma. The electric current in the arched plasma was kept low enough to keep it kink stable. The experimental results show that the sigmoid plasma structures are naturally produced in a sheared magnetic field configuration. The magnitude and handedness of the writhe of the arched plasma strongly depend on the structure of the guiding magnetic field. We found that orienting the guiding magnetic field nearly parallel to the electric current in the arched plasma results in a reverse-S shape. For an antiparallel orientation, the arched plasma assumed a forward-S shape. Moreover, the magnitude of the writhe and twist was correlated with the strength of the shear in the guiding field (strength of strapping magnetic field

applied). These results are significant in light of the distribution of arched plasma structures on the Sun. Namely, the reverse-S shaped structures are more common in the Northern Solar Hemisphere, while forward-S shaped structures are characteristic of the Southern Hemisphere.

The presence of strong shear in the magnetic field was observed to cause an eruption of a transient jet structure out of the arched laboratory plasma. The detailed study of this phenomenon constitutes the second focus of this dissertation. Jet-like structures are commonly formed from arched plasma structures in the lower solar atmosphere (e.g., anemone jets and spicules). Due to our experiment's relatively high density of neutrals, we can simulate the highly collisional conditions of the photosphere and lower chromosphere of the Sun. This capability is very unique to our laboratory setup. The ion-neutral collisions significantly impact the dynamics of lower atmosphere solar structures and our laboratory plasma structures. We employed the diagnostics of the magnetic field, density, temperature, and ion flow to characterize the jet structure formed in these experiments. We found that in its early stages, the laboratory jet has a supersonic (around Alfvén speed) ion flow away from the arch, driven primarily by a large gradient in the magnetic field. On the Sun, structures like spicules are also found to carry an ion flow at velocities around the Alfvén speed. The jet under study carries the electric current, which returns to the arch gradually with distance through an ion-neutral charge transfer collision mechanism. The electron current returns to the anode via a path crossing the weakest magnetic field lines, making a sharp turn near the magnetic null.

The work presented here has contributed to our knowledge of the dynamics of arched magnetized plasmas relevant to similar structures in the lower solar atmosphere. The arched plasma's electric current in our experiments was naturally low enough to keep it kink-stable. This unique feature of our experimental setup allowed us to study the arched plasma's sigmoid shape morphology and the plasma jet eruption dynamics purely in terms of the pre-existing magnetic field configuration. Our studies show that strong shear in the vacuum magnetic field not only impacts the morphology of the arched plasma but can also drive a formation of a jet structure. The significant presence of neutrals in our plasma is yet another unique aspect of this experiment. At around

2% ionization level, the plasma studied here is relevant to solar plasma found in prominences, chromosphere, and photosphere. With the new insights and all hardware and software developed during this dissertation, we have established a platform for further research on these topics. We hope this dissertation is but a building block of a future predictive model of eruptive arched plasma structures on the Sun.

The dissertation of Kamil Daniel Sklodowski is approved.

Walter N Gekelman

Marco CM Velli

Shreekrishna Tripathi

Christoph Niemann

Troy A Carter, Committee Chair

University of California, Los Angeles

2023

To my grandmother Jadwiga Zych . . .

who sparked my passion for science,

and paved the way for me to become who I am today.

Dziękuję ci babciu z całego serca.

TABLE OF CONTENTS

LIST OF FIGURES

LIST OF TABLES

ACKNOWLEDGMENTS

This was definitely a journey that I will never forget. A journey full of obstacles and hardships that was made possible with the most supportive, understanding, and knowledgeable people I've ever met. I am forever filled with gratitude to each of them and the entire Ph.D. experience for helping me grow into who I am today.

Firstly I would like to thank my advisor, Troy Carter, for his limitless support. Words cannot express my gratitude for the group environment he cultivated. I am beyond lucky to have worked with such an inspiring, supportive, beyond-patient, and plasma-guru advisor. Thank you for guiding me through the past seven years. And thank you for getting me hooked on cycling in the meantime. The weekly Mandeville bike rides concluding with ceremonial bagels or donuts were always something to look forward to (I am yet to complete one in under 20 minutes). It was a pleasure and privilege to work with you.

I want to thank Doctor Shreekrishna Tripathi, who was always there for me when I had questions or doubts. He spent a vast amount of time helping me in the lab, reviewing my papers, discussing experimental results, and ensuring I was on track. Thank you for your endless patience with me and the support for me, without which I wouldn't be writing this dissertation. You have taught me diligence, carefulness, and persistence both at work and in life. I am forever grateful for it.

I thank the rest of my Ph.D. committee members - Walter Gekelman, Christoph Niemann, and Marco Velli - for their guidance, time, feedback, and review of this dissertation. Thank you for all the valuable discussions on my research over the past years.

I had no prior plasma physics background when I first joined this group. I was very fortunate to have older graduate students - Giovanni Rossi and Jeff Robertson - who helped me get up to speed. Thank you both for your mentorship and the golden vibes you brought to our research group.

The daily routine would be unbearable without the best people I shared it with. Thank you, Gurleen Bal (a.k.a. homie prime), Yhoshua Wug, and Phil Travis, for distracting me just the right

amount. It kept me sound and sane. I am truly grateful for all the laughs, banters, ping pong sessions, and everything that helped me decompress and carry on. I appreciate the friendships we have formed over these years, and I will cherish them forever. I am especially grateful to Gurleen for always being there for me, cheering me up, and her boundless support. I cannot imagine a safer space to talk than with you. Gurleen and I shared an apartment for over five years during grad school, where the amount of silly was over the roof. The best roommate, labmate, and friend I could ask for.

This work would not be possible without the contributions of the staff at BaPSF. Countless thanks to Zoltan Lucky for always knowing where everything is and how to solve any engineering issue I had; Marvin Drandell and Tai Ly for their manufacturing expertise - the amount of parts they have machined for me is beyond the count; Pat Pribyl and Avdit Kohli for being my electronics gurus - the support with any electronic circuit I received from them is immeasurable. Last but definitely not least, I would like to thank our office administrator, Meg Murphy, for the warmth and support she gave me over the years. I have enjoyed our chats and hikes beyond any measure. Thank you for being there for me and always cheering me up.

I am grateful to my undergraduate college advisor and mentor, Cherice Evans, who inspired me to pursue scientific research. While working in her group, I traveled to different states to work in synchrotron facilities and national labs. It was a truly remarkable experience for a first-generation college student like me. Thank you for guiding me along the way and helping me earn two dual degrees.

I absolutely have to mention my best friend from college, Davneet Kaur, who never failed to support me, endure me at my worst, and enjoy the time we spent together. I am extremely fortunate to have met you in Queens College Physics Club. Thank you for always being there for me and encouraging me to push forward. You are a true inspiration for me academically and in life.

I have been exceptionally fortuitous to have met my partner and the best travel companion, Dominic Hugo, during my grad school journey. He was absolutely crucial in ensuring my final success. Thank you for being the brightest ray of the Sun in my life, always putting a smile on my

face, and helping me become the best version of myself. Mahal na mahal kita.

I want to thank my family, both immediate and distant. I am forever grateful for all the support and encouragement I got from you. Special thanks to my grandmother Jadwiga Zych who planted the first science seed by gifting me a microscope and tons of slides in elementary school. I am thankful for the limitless love and support from my mom, Dorota Sklodowska, and brother, Konrad Sklodowski, which carried me through grad school and life. I extend my gratitude to my father, Artur Krynski, for his tireless work and commitment that led to our family's relocation to the United States. I will forever be thankful for the opportunities he has provided me. I absolutely love you all.

Finally, I would like to thank for the financial support from the National Science Foundation through award PHY-1619551; the United States Department of Energy through award DE-SC0022153; NASA (HERMES DRIVE Science Center) for partial support to Shreekrishna Tripathi under award 80NSSC20K0604. The experiments conducted for this dissertation were carried out at the Basic Plasma Science Facility (BaPSF) at UCLA, supported by the US DOE under Contract No. DE-FC02-07ER54918 and the NSF under Award No. PHY1561912.

Chapter 3 of this dissertation is an adaptation of my publication: Sklodowski, K., Tripathi, S., & Carter, T. (2021). Evolution of an arched magnetized laboratory plasma in a sheared magnetic field. *Journal of Plasma Physics, 87*(6), 905870616. doi:10.1017/S0022377821001239

Lastly, Chapter 4 is based on my most recent publication: Sklodowski, K., Tripathi, S., & Carter, T. (2023). Dynamic Formation of a Transient Jet from Arched Magnetized Laboratory Plasma. *in preparation for publication*

VITA

2013–2016 Research Assistant, Chemistry Department, CUNY Queens College

2016 B.A.-M.A. (Physics) and B.A.-M.A. (Chemistry), CUNY Queens College.

2016–2017 Teaching Assistant, Department of Physics and Astronomy, UCLA. Taught laboratory sections of Physics 5 series (Physics for Life Science Majors)

2017–2023 Graduate Student Researcher, Department of Physics and Astronomy, UCLA.

PUBLICATIONS AND PRESENTATIONS

Sklodowski, K., Tripathi, S., & Carter, T. (2023). Dynamic Formation of a Transient Jet from Arched Magnetized Laboratory Plasma. *in preparation*

Sklodowski, K., Tripathi, S., & Carter, T. (2021). Evolution of an arched magnetized laboratory plasma in a sheared magnetic field. *Journal of Plasma Physics, 87*(6), 905870616. doi:10.1017/S0022377821001239

AGU Fall Meeting (12/2018). *Three-dimensional evolution and formation of multiple current filaments in laboratory arched magnetized plasma*, poster presentation

SHINE workshop (08/2019). *Three-dimensional evolution and formation of multiple current filaments in laboratory arched magnetized plasma*, poster presentation

APS Division of Plasma Physics Annual Meeting (10/2019). *Current filamentation and eruption of a laboratory arched magnetized plasma*, poster presentation.

APS Division of Plasma Physics Annual Meeting (11/2020). *Writhe of a Laboratory Arched Magnetized Plasma evolving in a Sheared Magnetic Field*, poster presentation.

APS Division of Plasma Physics Annual Meeting (11/2021). *Evolution of an Arched Magnetized Laboratory Plasma in a Sheared Magnetic Field*, poster presentation.

AGU Fall Meeting (12/2021). *Ejection of Magnetic flux Ropes from an Arched Laboratory Plasma Evolving In a Sheared Magnetic Field*, poster presentation.

SHINE workshop (06/2022). *Laboratory Study of Arched Plasma Eruptions in a Sheared Magnetic Field*, poster presentation.

APS Division of Plasma Physics Annual Meeting (10/2022). *Laboratory Study of Arched Plasma Eruptions in a Sheared Magnetic Field*, poster presentation.

CHAPTER 1

Introduction

1.1 Motivation and Background

This dissertation aims to study laboratory arched magnetized plasma structures relevant to similar structures on the Sun. The Sun's atmosphere is abundant in diverse arched magnetized plasma configurations across its depth. The solar atmosphere consists of three layers, the lowest being the photosphere, the chromosphere, and the outermost solar corona [1]. The lower solar atmosphere (photosphere and lower chromosphere) is characterized by a temperature of 5000 – 6000 K, number densities of 1×10^{13} cm^{-3} – 5×10^{16} cm^{-3}, magnetic field ranging from around 1000 to 100 Gauss at a higher elevation, and ionization level (ion number density with respect to neutral number density) as low as 10^{-4} at lower altitudes, staying below unity at upper heights [1, 2, 3, 4]. On the other hand, the solar corona (upper solar atmosphere) is much hotter, reaching temperatures on the order of a Mega-Kelvin. The coronal number density is on the order of 10^{9} cm^{-3}; the magnetic field is around a few Gauss, and the plasma there is nearly fully ionized (almost no neutrals present). Even though the conditions substantially vary across the solar atmosphere, various types of arched plasma structures are found in all its layers [5, 6]. Due to physical limitations, current diagnostics of the solar structures rely solely on observational data. Despite advancements in measurements of the parameters of solar plasmas [5, 7, 8, 9], they are calculated from observational data using theoretical models that naturally come with limitations and assumptions (e.g., plasma homogeneity, force-free magnetic fields) [10, 11]. Consequently, this leads to varying results between different approaches [12, 10], and may not represent the true system [13, 14]. The laboratory plasma studied in this dissertation exhibits solar-relevant parameters and allows for reliable in situ

diagnostics. With high experimental reproducibility, we can conduct a systematic study of arched laboratory plasma structures to better understand the dynamics governing similar structures on the Sun.

1.1.1 Arched Plasmas on the Sun

Solar prominences are among the most commonly occurring solar arched plasmas (see figure 1.1a). They are arched magnetized plasma clouds protruding from the surface of the Sun [15]. When seen against the solar disk, they show up in absorption as a dark S-shaped (sigmoid) feature against the bright disk. In observations above the solar limb (figure 1.1a), the solar prominences appear bright against the background. There is a correlation between the chirality (left- or right-handedness) of the sigmoidal shape and the location where prominences occur [16]. Notably, the forward-S shape (left-handed) dominates in the southern hemisphere, while the reverse-S shaped prominences (right-handed) are predominantly found in the northern hemisphere. With its footpoints settled in the photosphere, a solar prominence can expand into higher altitudes of the corona, reaching heights of up to 10^8 m. Typically, a prominence plasma is partially ionized ($n_i/n_n \approx 0.7$, where n_i and n_n are ion and neutral number densities respectively [11]) and about a hundred times colder and denser than a corona. The plasma beta, $\beta = 2\mu_0 p/B^2$, (where p is the thermal pressure, mu_0 is the vacuum permeability, and B is the magnetic field) is a dimensionless ratio of plasma hydrodynamic pressure to its magnetic pressure. For prominences, $\beta \approx 10^{-1}$ – 10^{-3}, which means that magnetic forces dominate over the hydrodynamic ones. The Lundquist number (ratio of the diffusive timescale to the convective timescale) measures how well a magnetic field is frozen to the plasma. This ratio is on the order of 10^{10} [11] for prominences. Due to a high magnetization state, in equilibrium, a prominence is often approximated to be force-free [17, 18, 19]. In such a state, the electric currents are parallel to the magnetic field, or mathematically, $\mathbf{J} = \alpha\mathbf{B}$, so the magnetic force $\mathbf{J} \times \mathbf{B}$ vanishes. However, the force-free approximation is invalid for evolving, and dynamic arched flux ropes (prominences) [20]. These structures can be further categorized based on their morphology, spectrum, and activity level [6, 21, 15]; however, they still share the same

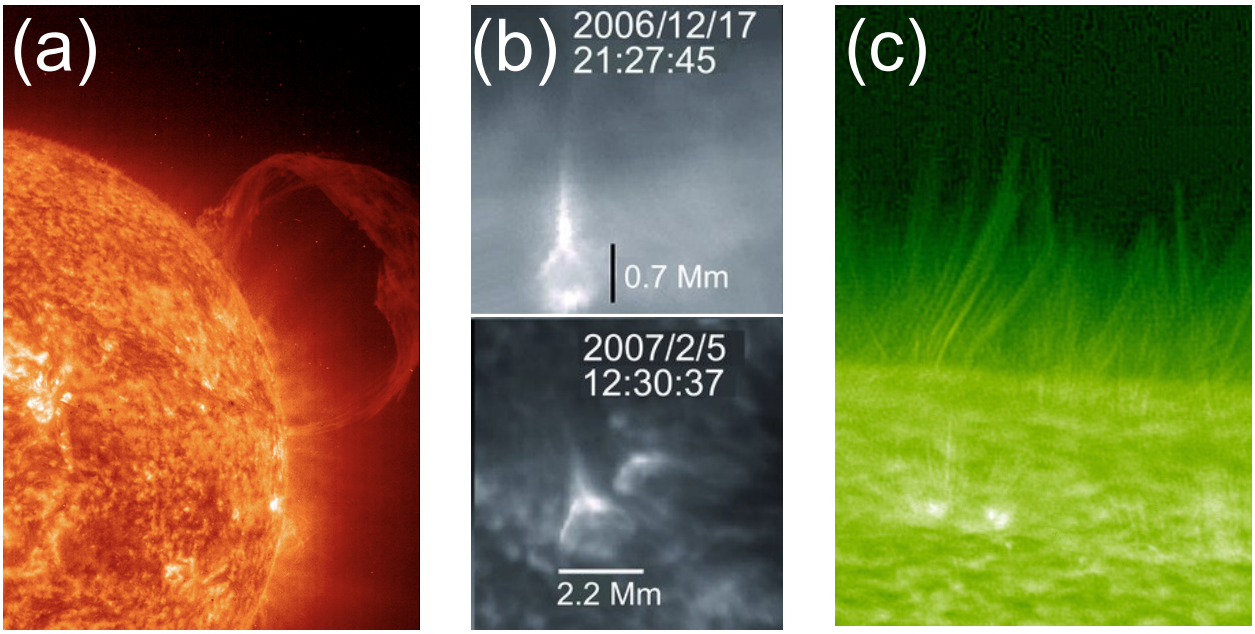

Figure 1.1: Observational data of some solar structures of interest. **(a)** Solar prominence observed in extreme ultraviolet [30.4 nm] by SOHO/EIT. **(b)** Anemone jets ejected from arched flux ropes in the chromosphere observed through Ca II *H* broadband filter [396 nm] by SOT/*Hinode* telescope. Times are shown in UT. **(c)** Solar spicules observed through Ca II *H* broadband filter [396 nm] by SOT/*Hinode* telescope. Courtesy of NAOJ/JAXA.

fundamental physics, and the regimes of important parameters [22].

Solar prominences have been observed to remain stable from a few days to up to a few months [23, 24, 25, 26, 15], most of them simply vanishing in the end. Occasional loss of stability, however, leads to eruptive events [27, 28, 29, 30, 15]. Solar flares and coronal mass ejections (CMEs) are examples of significant prominence-driven eruptions. A CME ejects a large amount of energy ($10^{23} - 10^{26}$ Joules) through fast-moving charged particles and/or radiation [20]. These eruptive events can trigger geomagnetic storms, damage power transmission lines, severely affect communication satellite systems, and be hazardous to astronauts in space [31]. The exact physical mechanisms driving such eruptions remain an open area of research. Some authors credit kink and/or torus instability as possible drivers (more discussion in section 1.4, while others look into mag-

netic reconnection between the emerging flux and the pre-existing magnetic field [32, 33, 34, 35]. A deeper insight into the dynamics of solar prominences and processes leading to their eruptions would allow for the development of a predictive model.

Many other smaller-scale arched plasma structures are also prevalent throughout the solar atmosphere. Often referred to as minifilaments, these coronal arched plasmas can erupt, resulting in jet-like structures (coronal jets) [36, 37, 38]. The minifilaments have been observed to be $\approx 8 \times 10^6$ m long, which is considerably smaller than solar prominences. The erupted jets have lengths on the order of 5×10^7 m and lifetimes of around 10 minutes. One of the suggested mechanisms for this eruption involves a magnetic reconnection between the emerging flux of the bipole filament (arch) and the open ambient magnetic field [39, 40]. Others indicate the high shear in the arched magnetic field as the driver of these eruptions [37].

Phenomena like anemone jets (see figure 1.1b) have been observed in the chromosphere. Compared to coronal jets, these structures are shorter in length and time scales (length: $\approx 2 \times 10^6$ m, lifetime: 100 – 500 s) [2]. The anemone jets are thought to erupt due to flux emerging in a bipole region (arched plasma) reconnecting with the pre-existing magnetic field [2].

Solar spicules are perhaps one of the most elemental constituents of the solar chromosphere. They can be observed as jets at the limb of the Sun in chromospheric spectral lines (Hα). A sample observation is presented in figure 1.1(c). Typically, spicules have lengths on the order of 10^7 m, lifetimes between 1 – 10 minutes, and outward flows with speeds comparable to local sound, and Alfvén speeds [41]. It was found that some spicules may form as a result of erupting microfilaments in the chromosphere [42]. Microfilaments are even smaller (≈ 300 km) arched plasma structures in the chromosphere. In that model, spicules are analogous to the coronal jets erupting from minifilaments. A significant presence of neutrals in partially ionized chromosphere was also proposed as a major driving force for solar spicules [43].

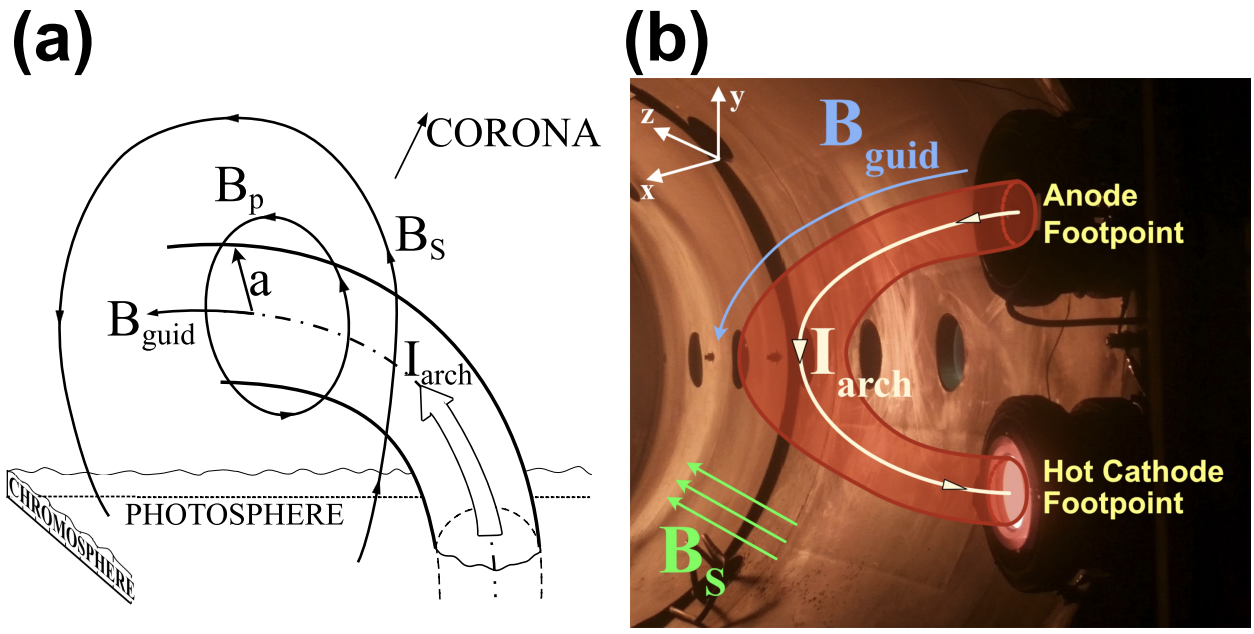

Figure 1.2: **(a)** Schematic of a flux rope model in the solar corona with overlying strapping field B_S. Minor radius a and flux rope current I_{arch} are indicated. The guiding magnetic field B_{guid} and the poloidal magnetic field B_p are also noted. [adapted from [20]]. **(b)** Photograph of the experimental setup depicting an arched current filament I_{arch}, guiding magnetic field B_{guid}, and the strapping (or ambient) magnetic field B_S. The experiment simulates the background conditions of a solar prominence shown in (a).

1.1.2 General Model

In laboratory and computer simulations, the solar prominences and other arched magnetized plasma structures are typically modeled with flux ropes. Those twisted magnetic plasma structures carry electrical current and follow an external magnetic field [44, 45, 46, 47]. A typical model of solar prominence is presented in figure 1.2(a). The arched flux rope carries electrical current I_arch along the arched guiding magnetic field B_{guid}. That electrical current produces the poloidal magnetic field B_p. There is an additional external large-scale magnetic field, B_S, called an ambient or strapping magnetic field. The pre-existing magnetic fields are produced by current channels beneath the arched structure [24]. Experiments presented here were designed [48, 49] to study

arched magnetized plasma structures in a laboratory setting. A photograph of the arched plasma source is presented in figure 1.2(b). The corresponding magnetic fields and features are sketched over the picture. The footpoints of the plasma are fixed on the electrodes (source described in detail in chapter 2), which imposes a line-tied boundary condition. We can adjust various parameters in this experimental setup and probe the arched plasma under different scenarios. The dimensionless plasma parameters are kept close to those found on the Sun to keep the physics of arched plasma solar-relevant. A significant presence of neutral background gas results in high ion-neutral collisionality which ties our experiment to the conditions of the lower solar atmosphere and the partially ionized solar prominences. Typical plasma parameters and a detailed discussion follow in the chapters below.

1.2 This Experiment in light of Previous Work

Several research groups have conducted experimental studies on arched plasmas in the past. The first laboratory experiment studying the solar-relevant arched plasmas demonstrated that an arched magnetic flux rope (AMFR) could be created by driving an electrical current along a guiding magnetic field [50]. The following generation of laboratory experiments on arched plasmas was developed in the early 2000s by the Caltech group [51, 22, 52, 49]. Their findings include explaining sigmoidal shapes and filamentation of the current channels via a force-free state equation and demonstrating that the strapping field can inhibit the eruption of solar prominences. The Caltech group also researched kink instability, identifying it as a poloidal flux amplification mechanism [53]. That work has been followed by AMFR experiments conducted at FlareLab [54, 55]. At Princeton, the MRX group investigated arched plasma stability in terms of kink and torus instability parameters [56, 32], where they identified the guiding magnetic field tension force as the key mechanism to suppress eruption. The MRX group also studied the low-β MHD forces in an arched laboratory plasma [57]. Dynamics of straight magnetic flux ropes, including magnetic reconnection and kink instability, have been extensively studied in laboratory experiments

[58, 59, 60, 61, 62]. In the above-mentioned laboratory research on arched magnetized plasmas, the electrical current rises to several kiloamperes within a few Alfvén transit times, t_A (time taken by the Alfvén wave to travel from one to another footpoint of the arched plasma). As a result, the outward hoop force (see discussion in section 1.3) and strong poloidal twist (section 1.4) dominate the arched plasma dynamics during the pre-eruption phase. This is unlike the pre-eruptive solar arched plasmas with less than two poloidal twists from one footpoint to the other [7, 63]]. A new approach to laboratory studies of solar-relevant AMFRs was introduced at UCLA to capture the essential features of solar AMFR eruptions [48, 64]. Due to a much lower electrical current ($<$ 200 A) and the poloidal twist of the magnetic field, the UCLA setup captures essential features of solar-relevant arched plasmas. Moreover, the experiment's substantial presence of the neutral background gas contributes to the high ion-neutral collisionality. This is unique to our experiment and consistent with the partially-ionized conditions of the lower solar atmosphere and solar prominences (see section 1.5).

The experiments at UCLA introduce two independent plasma sources, producing the arched magnetized and background plasma. The arched plasma's evolution can occur in the presence of a magnetized background plasma, which plays an important role in wave excitation and energy transport. Moreover, the relative magnitude of parameters in the arched and background plasma can be varied, and the magnetic field direction can be reversed. Most importantly, the electrical current in the arched plasma can be kept below the kink-instability threshold long enough ($> 50t_A$) to study the behavior and evolution of an arched plasma during the pre-eruption phase. The strapping magnetic field in our experiment is produced using electromagnets wound around a cylindrical vacuum chamber (see section 2.1.3). This field is spatially uniform and therefore has no decay index. Hence, the arched plasma is torus stable (see section 1.4). On the Sun, the strapping magnetic field is frequently on a much larger spatial scale than prominence; thus, locally, it can be viewed as nearly uniform. We aim to study the arched plasma's dynamics, stability, and eruptivity exclusively in terms of magnetic field configuration. The high reproducibility of this experiment and the ability to take measurements in three spatial dimensions allows for reconstruction and vi-

sualization of the magnetic field, current density, and other plasma parameters in three dimensions while resolved in time.

1.3 Forces on Arched Plasma

The total Lorentz force acting on the arched current-carrying plasma subjected to guiding and strapping magnetic fields can be decomposed into four major components. With a reasonable assumption of a half-torus shape, three forces act along the major radius: tension, hoop, and strapping [20, 24]. The fourth force is a pinch force acting along the minor radius of the arched plasma. These MHD (see section 1.6) forces are well known in the tokamak community and have been originally derived by Shafranov [65]. A simplified diagram of the forces acting on the arched plasma is presented in figure 1.3. The tension force F_t is a restorative force resulting from the poloidal currents interacting with the guiding magnetic field. The tension of the guiding magnetic field tends to prevent the expansion of the major radius of the arched plasma. Per unit length, this force can be expressed as,

$$\mathbf{F_t} = -\frac{\hat{R}}{R}\int \frac{1}{\mu_0}\left(B_{gv}^2 - B_g^2\right) dS, \tag{1.1}$$

where $\hat{R}$ is a unit vector pointing along the major radius R, μ_0 is the permeability of vacuum, B_{gv} is the vacuum guiding magnetic field, B_g is the total guiding magnetic field (includes the contribution from plasma), and S is the cross-section surface. In our experiment, we can control this force by adjusting the magnitude of the guiding magnetic field. The hoop force F_h is also directed along the major radius, and it assists in the outward expansion of the arch. This force results from a curvature of the current channel and, therefore, its self-inductance L. The latter can be expressed as:

$$L = \mu_0 R\left[\ln\left(\frac{8R}{a}\right) - 2 + \frac{l_i}{2}\right] \tag{1.2}$$

where a is the minor radius of the arched plasma, and l_i is the internal inductance per unit length. Typically this dimensionless parameter is on the order of unity [20]. For a hollow surface current distribution, $l_i = 0$; for a non-force-free distributed current in the arch, $l_i \approx 1$ (our experiment).

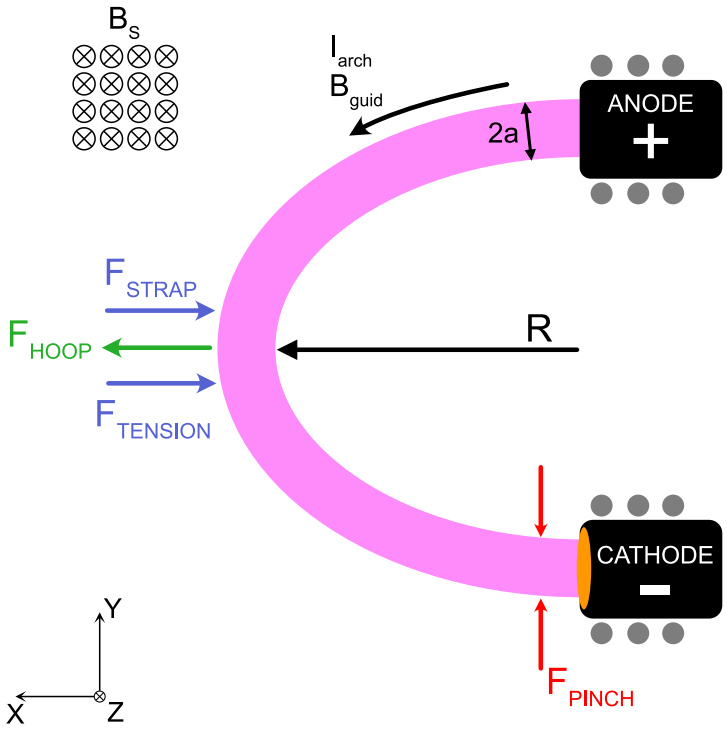

Figure 1.3: A diagram showing major MHD forces acting on the arched plasma. Here, the electrical current follows the guiding magnetic field, and the strapping magnetic field is oriented along the positive z-axis such that the resulting force inhibits the expansion of the arch. The major radius R and the minor radius a of the arched plasma are noted. The coordinate system is marked in the lower left corner.

With that in mind, the hoop force per unit arch length can be expressed as:

$$\mathbf{F_h} = \frac{1}{2\pi R} I^2 \frac{\partial L}{\partial R} \hat{R} = \frac{\mu_0}{2\pi R} I^2 \left[\ln\left(\frac{8R}{a}\right) - 1 + \frac{l_i}{2} \right] \hat{R}, \tag{1.3}$$

where I is the arched plasma current. In our experiment, we can control hoop force by adjusting the discharge current. The last major force acting along the major radius of the arched plasma is the strapping force F_S. This force is essentially a Lorentz force between the arched plasma current and the strapping (overlying) magnetic field B_S. Depending on the direction of the overlying magnetic field, the strapping force can be either inwards (for B_S along the positive z-axis) or outwards (for B_S along the negative z-axis). The strapping force (per unit length of the arched plasma) can be estimated by:

$$\mathbf{F_S} = -\frac{\hat{R}}{\pi R} \int \mathbf{J} \times \mathbf{B_S} 2\pi R dS = -2 I B_s \hat{R}, \tag{1.4}$$

where $\mathbf{B_S}$ is the strapping field, and $\mathbf{J}$ is the current density in the arched plasma. We have the most control over this force. By adjusting the direction and magnitude of the overlying magnetic field, we can manipulate the strapping force's strength and direction. The fourth force worth mentioning is the pinch force, F_p, acting along the minor radius of the arched plasma. It results from the plasma electrical current interacting with the poloidal magnetic field. It tends to decrease the minor radius of the arch with increasing current (hence the name 'pinch'). We can estimate this force as follows:

$$\mathbf{F_p} = -\hat{a} \int \mathbf{J} \times \mathbf{B_{pol}} 2\pi R dS = -\frac{\mu_0 I^2}{4\pi a} \hat{a} \tag{1.5}$$

where $\mathbf{B_{pol}}$ is the poloidal magnetic field due to arched plasma.

Relative magnitudes of these forces govern the dynamics of an arched magnetized plasma in the laboratory and on the Sun. For a typical solar prominence, the relative magnitudes of hoop, tension, and strapping forces are 1.0, 0.3, and 0.7, respectively [24]. The magnetic field configurations were chosen strategically for this experiment to keep its physics as close to the solar case as possible.

1.4 Kink and Torus Instabilities

Solar eruptions (e.g., flares, CME) are often accredited to be driven by a kink or torus instability in the arched plasma [66]. Even though the arched plasma in all of our experiments was both kink- and torus-stable, we think it is worth briefly describing each instability for the reader.

The solar prominences and similar arched solar plasma structures are commonly modeled as flux ropes. These magnetic plasma structures are twisted due to a significant poloidal magnetic field generated by the toroidal electrical current (along the arch) [44, 45, 46, 47]. That twist increases with the current carried by the flux rope and can lead to the development of an unstable kink when the total twist exceeds a critical value. Observational signatures of this instability are usually associated with helical deformations (i.e., writhe and twist) of filaments and prominences [45, 67, 68, 69]. Under ideal MHD assumptions (which are commonly employed for solar prominences), the magnetic helicity, $H = F^2(T + W)$, is nearly conserved [70]. Here, H is the relative helicity, F is the axial magnetic flux, W is the writhe, and T is the number of turns of the field line (twist). Qualitatively, the twist measures the turning angle of a bundle of magnetic field lines around its central axis. Writhe, on the other hand, is a measure of net self-coiling of magnetic field lines and is related to its total torsion (how sharply it is twisting out of the plane of curvature) [71]. A magnetic flux rope carrying an electrical current along an externally imposed toroidal magnetic field (guiding field) is expected to develop writhe due to the dominance of a self-generated poloidal magnetic field, B_p. Without a strapping magnetic field applied, the flux rope's writhe depends on the magnitude of electrical current and the strength of the guiding magnetic field. The twist and writhe are closely coupled to each other through magnetic helicity. The total twist, Φ, can be expressed as [72],

$$\Phi = \frac{lB_\phi(r)}{rB_z(r)}, \tag{1.6}$$

where l is the length of the flux rope, r is the minor radius, B_z is the axial magnetic field, and B_ϕ is the azimuthal magnetic field. For a large enough current in the flux rope, the twist exceeds the critical value Φ_c, and the system becomes kink unstable. At that point, the flux rope evolves to

reduce the curvature of the magnetic field lines to lower the net magnetic energy. Effectively, the twist is converted into writhe [73, 74, 75, 76]. For line-tied magnetic arches in our experiments and on the Sun (aspect ratio = major radius/minor radius ≈ 5), the critical value of the twist parameter, Φ_c, was estimated to be $\approx 3.5\pi$ [19]. The twist was calculated for all our experiments and was consistently below the critical value. We purposefully applied a relatively low discharge current to keep our arched plasma kink stable and investigate alternative eruption mechanisms, as discussed in the chapters following below.

On the Sun, the overlying coronal magnetic field (strapping magnetic field) naturally decays with distance from the arched plasma footpoints [77]. This decay can be quantified by a unitless decay index $n = -d\ln(B_S)/d\ln(R)$, where B_S is the strapping magnetic field, and R is the major radius [78]. The faster the magnetic field decays along the major radius of the arch, the larger the decay index. When the strapping magnetic field (and thus the strapping force) decays faster than the hoop force, the arched plasma is said to be torus unstable. The critical value for a line-tied arched plasma has been calculated to be $n_{crit} = 1.5$ [77]. Since the strapping magnetic field is nearly uniform in our experiments, its decay index is zero. Consequently, the laboratory arched plasma under study here is torus stable.

1.5 Consequences of High Neutrals' density

The solar corona amounts to the upper solar atmosphere and is characterized by its nearly complete ionization level. The ionization level refers to the fraction of ions relative to the neutrals, n_i/n_n, and it approaches ∞ in the corona [20]. In stark contrast, the lower solar atmosphere (photosphere and lower chromosphere) is not only much colder than the corona, it has a significant neutrals density which must be accounted for in physical models. The ionization level in that region varies with height, reaching as low as 10^{-4} in coldest regions and approaching unity at higher elevations [79, 4, 3]. The substantial presence of neutrals results in high ion-neutral collision rates and plays an important role in the dynamics of the photospheric and chromospheric structures. Namely, one

has to consider phenomena such as the non-ideal Hall effect and ambipolar diffusion. Because ions are affected by the neutrals to a greater degree, their drift velocity will be slowed down by the neutrals more than electrons (which are also more bound by the magnetic field). This disparity in drift velocities is called a Hall effect [80]. The Hall effect operates on very different spatiotemporal scales in partially ionized plasma compared to fully ionized plasma. Ambipolar diffusion has two definitions depending on whether one asks a physicist or an astrophysicist. In physics, this term refers to the diffusion process of positively and negatively charged particles occurring at an equal rate due to their Coulomb interaction. At scales above the Debye length, this process maintains charge neutrality. In the context of this work, we are interested in the astrophysics definition. Here, ambipolar diffusion is the decoupling between neutral and charged components leading to the diffusion of magnetic field via ion-neutral collisions [3]. The abundance of neutrals in the lower solar atmosphere has been shown to impact the propagation of MHD waves [81], excitation of Alfvén waves, and rate of magnetic reconnection [4], as well as dissipation of electric currents [82]. In solar prominences ($n_i/n_n \approx 0.7$ [11]), the ion-neutral collisions result in a frictional force contributing to the support of their structure against the gravity [83]. The presence of neutrals in partially ionized chromospheric plasma has also been suggested as a major driver of solar spicules [43]. Our experiments were conducted in a high presence of neutrals to stay relevant to the lower solar atmosphere. The average ion to neutral density ratio was $n_i/n_n \approx 2 \times 10^{-2}$. To calculate the collision frequency ν_{jn} between a charged species j and the neutral species n we use [84]:

$$\nu_{jn} = n_n \frac{m_n}{m_j + m_n} \frac{4}{3} \sqrt{\frac{8k_B T_j}{\pi m_j} + \frac{8k_B T_n}{\pi m_n}} \sigma_{jn} \tag{1.7}$$

where n_n is the neutral number density, m_n, m_j are the masses of neutrals and charged species respectively, T_n, T_j are their temperatures in Kelvin, k_B is the Boltzmann constant, and σ_{jn} is the collision cross section of the two species. For an elastic collision of a He+ ion with a Helium neutral atom, $\sigma_{in} = 0.1 \times 10^{-17}$ m^2 in the regime of our experiment [85]. The ion-neutral collision frequency in our experiments was determined to be $\nu_{in} \approx 5.4 \times 10^5$ Hz. For comparison, this collision frequency ranges between 10^5–10^9 with elevation in the photosphere and the chromosphere. To ensure that we access a similar physical regime, we look at a dimensionless ratio of ν_{in}

to the ion cyclotron frequency $\Omega_i = ZeB/m_ic$, where Z is the ion charge state (usually 1), e is the electron charge, B is the magnetic field, m_i is the mass of an ion, and c is the speed of light, all in cgs units. This parameter, Ω_i/ν_{in}, is about 2.1×10^{-2} in our experiments and varies between 10^{-1} – 10^{-4} in the lower solar atmosphere [86, 2]. The densities and particular collision rates in our experiments are listed in tables 2.1 and 2.2 of chapter 2. The comparison between relative experimental values and those found in similar photospheric structures is compiled in table 4.1 of chapter 4. Evidently, our experiments correspond well to the conditions existing in the lower solar atmosphere and solar prominences in terms of neutrals and their effects.

1.6 Relevance to the Sun in Terms of a Multi-Fluid Description

Solar phenomena are often modeled within a resistive magnetohydrodynamics (MHD) framework due to its relative simplicity [76, 87, 88, 20, 24]. MHD studies interactions between a conductive fluid (plasma) and a magnetic field [76]. In an ideal MHD model, the fluid has no resistance, is highly collisional, and the length scales of interest are larger than ion gyroradius. In such a case, the magnetic field is considered "frozen-in" to the plasma flow [89]. Otherwise, nonlinear effects like the Hall effect and resistive term are usually kept in the model for better accuracy. It is also important to note that MHD simplifies a more detailed two-fluid theory that treats electrons and ions separately [89, 22]. The two-fluid theory, on the other hand, is a simplification of a more correct Vlasov equation. In the following subsection 1.6.1, we discuss a two-fluid theory applicable to solar prominences and our laboratory arched plasma. We then estimate the magnitudes of the induction equation terms and compare the solar values to our experiment's. This model, however, ignores the presence of neutrals and, thus, their impact on the dynamics. In subsection 1.6.2 we consider a three-fluid description that is particularly relevant to the lower solar atmosphere. The resulting induction equation contains Hall and ambipolar terms, of which estimated magnitudes are compared between the lab and the Sun.

1.6.1 Two-fluid Induction Equation

Within a two-fluid theory, the main drivers of electron velocity are the Lorentz forces, the electron-ion collisions, and the hydrostatic pressure [22]. The electron fluid equation of motion (or second Newton's law) is:

$$\underbrace{m_e \frac{d\mathbf{u}_e}{dt}}_{\text{inertia}} = -\underbrace{e(\mathbf{E} + \mathbf{u}_e \times \mathbf{B})}_{\text{Lorentz}} - \underbrace{\frac{1}{n_e}\nabla P_e}_{\text{hydrostatic}} - \underbrace{\nu_{ei} m_e (\mathbf{u}_e - \mathbf{u}_i)}_{\text{collisional}} \tag{1.8}$$

where $\mathbf{u}_e$, $\mathbf{u}_i$ are the velocities of electrons and ions respectively, e is the electron charge, $\mathbf{E}$ is the electric field, $\mathbf{B}$ is the magnetic field, n_e is the electron density, P_e is the electron thermal pressure, m_e is the mass of electron, and ν_{ei} is the electron ion collision frequency. We obtain the latter using the expression [84]:

$$\nu_{ei} = \frac{n_i e^4 \ln\Lambda}{3\epsilon_0^2 m_{ei}^2} \left(\frac{2\pi k_B T_e}{m_e} + \frac{2\pi k_B T_i}{m_i} \right)^{-3/2} \tag{1.9}$$

where $m_{ei} = (m_e m_i)/(m_e + m_i)$ is the reduced mass, m_e and m_i are electron and ion masses respectively, n_i is the ion number density, e is the electron charge, ϵ_0 is the vacuum permittivity, k_B is the Boltzmann constant, T_e and T_i are the electron and ion temperatures respectively, and $\ln\Lambda$ is the Coulomb logarithm with Λ being:

$$\Lambda = \frac{12\pi(\epsilon_0 k_B T_e)^{3/2}}{n_e^{1/2} e^3} \tag{1.10}$$

where n_e is the electron number density. The electron-ion collision frequency can also be related to the plasma resistivity η through [89]:

$$\nu_{ei} = \frac{n_e e^2}{m_e}\eta \tag{1.11}$$

The current density can be expressed as $\mathbf{J} = -en_e(\mathbf{u}_e - \mathbf{u}_i)$. The main contribution to the plasma's bulk (center of mass) motion comes from the ions (since they are much heavier than electrons). We can then approximate $\mathbf{u}_i \simeq \mathbf{U}$, where the latter is the center of mass velocity. With that, the electron velocity in the Lorentz term of equation (1.8) can be expressed as $\mathbf{u}_e \simeq \mathbf{U} - \frac{\mathbf{J}}{en_e}$. In the inertia term of equation (1.8), we can ignore the perpendicular motion of the electrons (gyromotion) since

we are interested in phenomena on timescales longer than the electron cyclotron period. Because the electrons are much lighter than ions, they will accelerate much faster along the magnetic field lines. We can write:

$$\frac{d}{dt}\left(\frac{\mathbf{J}_{\parallel}}{en_e}\right) = -\left(\frac{d\mathbf{u}_{e\parallel}}{dt} - \frac{d\mathbf{u}_{i\parallel}}{dt}\right) \simeq -\frac{d\mathbf{u}_{e\parallel}}{dt} \tag{1.12}$$

With that, equation (1.8) can be rewritten as:

$$\underbrace{-\frac{m_e}{e}\frac{d}{dt}\left(\frac{\mathbf{J}_{\parallel}}{n_e}\right)}_{\text{inertia}} = -e\left(\underbrace{\mathbf{E}+\mathbf{U}\times\mathbf{B}-\eta\mathbf{J}}_{\text{MHD Ohm's law}} - \underbrace{\frac{1}{en_e}\mathbf{J}\times\mathbf{B}}_{\text{Hall}}\right) - \underbrace{\frac{1}{n_e}\nabla P_e}_{\text{hydrostatic}} \tag{1.13}$$

The MHD Ohm's law can be obtained from the two-fluid theory by dropping the electron inertial term, the Hall term, and the hydrostatic pressure term. We eliminate the electric field $\mathbf{E}$ by taking a curl of equation (1.13) and using the Faraday's law, $\nabla\times\mathbf{E} = -\frac{\partial\mathbf{B}}{\partial t}$, to obtain:

$$\begin{aligned}\underbrace{-\frac{m_e}{e^2}\nabla\times\left(\frac{d}{dt}\left(\frac{\mathbf{J}_{\parallel}}{n_e}\right)\right)}_{\text{inertia}} = \underbrace{\frac{\partial\mathbf{B}}{\partial t} - \nabla\times(\mathbf{U}\times\mathbf{B}) + \nabla\times\eta\mathbf{J}}_{\text{MHD induction equation}} + \underbrace{\nabla\times\left(\frac{\mathbf{J}\times\mathbf{B}}{en_e}\right)}_{\text{Hall}} \\ \underbrace{-\frac{1}{e}\nabla\left(\frac{1}{n_e}\right)\times\nabla P_e}_{\text{hydrostatic}}\end{aligned} \tag{1.14}$$

To estimate each term's magnitude, we will rewrite equation (1.14) in terms of characteristic quantities. For a given system, we consider B_0 a characteristic magnetic field, n_0 a characteristic density, and a characteristic length scale L. With that, we can introduce dimensionless quantities of order unity:

$$\begin{aligned}\overline{\mathbf{B}} &= \mathbf{B}/B_0 \\ \overline{n} &= n/n_0 \\ \overline{\nabla} &= L\nabla \\ \overline{\mathbf{U}} &= \mathbf{U}/v_A \\ \bar{t} &= t/t_A\end{aligned} \tag{1.15}$$

where $v_A = B_0/\sqrt{\mu_0 n_0 m_i}$ is the Alfvén speed, and $t_A = L/v_A$ is the Alfvén time. Furthermore, we use the Ampere's law, $\nabla\times\mathbf{B} = \mu_0\mathbf{J}$ to replace the current density $\mathbf{J}$, and then multiply

equation (1.14) by t_A/B_0 to obtain:

$$\underbrace{-\frac{c^2}{\omega_{pe}^2 L^2}\overline{\nabla}\times\left(\frac{d}{d\bar{t}}\left(\frac{\overline{\nabla}\times\overline{\mathbf{B}}}{\overline{n}}\right)\right)}_{\text{electron inertia}} = \underbrace{\frac{\partial\overline{\mathbf{B}}}{\partial\bar{t}} - \overline{\nabla}\times(\overline{\mathbf{U}}\times\overline{\mathbf{B}}) + \frac{1}{S}\overline{\nabla}\times\overline{\nabla}\times\overline{\mathbf{B}}}_{\text{MHD induction}} + \\ + \underbrace{\frac{c}{\omega_{pi}L}\overline{\nabla}\times\left(\frac{(\overline{\nabla}\times\overline{\mathbf{B}})\times\overline{\mathbf{B}}}{\overline{n}}\right)}_{\text{Hall term}} - \underbrace{\frac{c}{\omega_{pi}L}\overline{\nabla}\left(\frac{1}{\overline{n}}\right)\times\overline{\nabla}\beta_e}_{\text{hydrostatic}} \tag{1.16}$$

where $\omega_{pi} = \sqrt{\frac{n_0 e^2}{\epsilon_0 m_i}}$ is the ion plasma frequency, $\omega_{pe} = \sqrt{\frac{n_0 e^2}{\epsilon_0 m_e}}$ is the electron plasma frequency, $\beta_e = 2\mu_0 P_e/B_0^2$ is the electron plasma beta, and S is the Lundquist number. The latter is a dimensionless ratio of the Alfvén crossing timescale to the resistive diffusion, $S = \frac{v_A L \mu_0}{\eta}$. The first two terms of the MHD induction term in equation (1.16) are on the order of unity. The resistive term is on the order of S^{-1}, the electron inertia term is of order $c^2/(\omega_{pe}^2 L^2)$, the Hall term is of order $c/(\omega_{pi}L)$, and the hydrostatic term is of order $\beta_e c/(\omega_{pi}L)$. We can now estimate the magnitude of each term for an average solar prominence and the arched laboratory plasma in our experiments. This exercise will allow us to gauge the importance of each term in the dynamics of plasma under study. The estimates are listed in table 1.1. In both cases of the solar prominence and our laboratory arched plasma, the Hall term is the primary contributor to non-ideal MHD effects. The resistive term is much smaller than the Hall term in both cases. Thus, as long as the resistive term remains small, the Lundquist number's actual value is irrelevant. For both environments, the order of terms is the same when arranged from largest to smallest. Based on that, we conclude that our experiment will capture the essential physics of solar prominence with correct boundary conditions. This model, however, ignores the presence of neutrals and their collisional coupling with the plasma constituents. The section below addresses that issue with a more complex approach.

1.6.2 Three-fluid Description

In weakly ionized plasmas ($n_i/n_n << 1$), the significant presence of neutrals introduces non-ideal MHD effects such as the Hall effect and ambipolar diffusion (see section 1.5). These effects are particularly important in the lower solar atmosphere and solar prominences characteristic of

Name	Term	Solar Prominence	Laboratory Arched plasma
Plasma beta	β_e	3.4×10^{-2}	8.0×10^{-2}
Lundquist number	S	8.4×10^{9}	3.5×10^{3}
Electron inertia	$c^2/(\omega_{pe}^2 L)$	3.5×10^{-18}	1.0×10^{-4}
Hall term	$c/(\omega_{pi}L)$	8.3×10^{-8}	0.85
Hydrostatic term	$\beta_e c/(\omega_{pi}L)$	2.8×10^{-9}	7.6×10^{-2}
Resistive term	S^{-1}	2.4×10^{-10}	5.9×10^{-4}

Table 1.1: Comparison of the equation (1.16) terms magnitude estimates for a typical solar prominence [20, 11] and the arched plasma in our experiments. For solar prominence we used $n_e = 3 \times 10^{10}$ cm^{-3}, $n_e/n_n = 0.5$, $T = 8000$ K, $B = 5$ Gauss. The arched plasma parameters used for these estimates are listed in table 2.2

weakly ionized plasma. Our unique experimental setup allows for the study of arched, weakly ionized plasma. In chapter 4, we study jet-like structures erupted from the laboratory arched plasma that is relevant to weakly ionized solar structures such as anemone jets and spicules. In a three-fluid model, we introduce neutrals as a third fluid in plasma. We can ignore the inertia of ions and electrons for weakly ionized plasma. Furthermore, as demonstrated in section 1.6.1, the inertia term is significantly smaller than all other terms. We will assume singly ionized ions and quasineutrality ($n_e \approx n_i$). We start with an equation of motion for electrons [90]:

$$\underbrace{m_e n_e \left[\frac{\partial \mathbf{u}_e}{\partial t} + (\mathbf{u}_e \cdot \nabla)\mathbf{u}_e\right]}_{\text{electron inertia}} = -\underbrace{e n_e(\mathbf{E} + \mathbf{u}_e \times \mathbf{B})}_{\text{Lorentz}} - \underbrace{\nabla P_e}_{\text{hydrostatic}} - \underbrace{\nu_{ei}\rho_e(\mathbf{u}_e - \mathbf{u}_i) - \nu_{en}\rho_e(\mathbf{u}_e - \mathbf{u}_n)}_{\text{collisional}} \tag{1.17}$$

where $\mathbf{u}_e$, $\mathbf{u}_i$, and $\mathbf{u}_n$ are fluid velocities of electrons, ions and neutrals respectively; m_e is the mass of electron, n_e and $\rho_e = m_e n_e$ are number and mass density of electrons; ν_{ei} is electron-ion collision frequency, and ν_{en} is electron-neutral collision frequency. As it is usually done, we ignore

the electron inertial force to obtain Ohm's law:

$$\mathbf{E} = -\mathbf{u}_e \times \mathbf{B} - \frac{\nabla P_e}{en_e} - \frac{\nu_{ei}\rho_e(\mathbf{u}_e - \mathbf{u}_i)}{en_e} - \frac{\nu_{en}\rho_e(\mathbf{u}_e - \mathbf{u}_n)}{en_e} \tag{1.18}$$

For weakly ionized plasma, we can also ignore the ion inertia [90] to obtain the ion force balance as:

$$0 = -\nabla P_i + en_i\left[\mathbf{E} + \mathbf{u}_i \times \mathbf{B}\right] - \nu_{in}\rho_i(\mathbf{u}_i - \mathbf{u}_n) - \nu_{ie}\rho_i(\mathbf{u}_i - \mathbf{u}_e) \tag{1.19}$$

where ν_{ie}, ν_{in} are ion-electron and ion-neutral collision frequencies respectively. The current density can be written as $\mathbf{J} = -en_e(\mathbf{u}_e - \mathbf{u}_i)$. With the relation $\nu_{ie}\rho_i = \nu_{ei}\rho_e$, we substitute equation (1.18) into equation (1.19) to arrive at:

$$(\mathbf{u}_n - \mathbf{u}_i)\left(1 + \frac{\nu_{en}\rho_e}{\nu_{in}\rho_i}\right) = \frac{\nabla(P_e + P_i)}{\nu_{in}\rho_i} - \frac{\mathbf{J} \times \mathbf{B}}{\nu_{in}\rho_i} - \frac{\nu_{en}\rho_e\mathbf{J}}{en_e\nu_{in}\rho_i} \tag{1.20}$$

which gives us a relative velocity between ions and neutrals. The neutral fluid equation of motion can be written as:

$$\underbrace{m_n n_n\left[\frac{\partial \mathbf{u}_n}{\partial t} + (\mathbf{u}_n \cdot \nabla)\mathbf{u}_n\right]}_{\text{neutral inertia}} = -\underbrace{\nabla P_n}_{\text{hydrostatic}} - \underbrace{\nu_{ne}\rho_n(\mathbf{u}_n - \mathbf{u}_e) - \nu_{ni}\rho_n(\mathbf{u}_n - \mathbf{u}_i)}_{\text{collisional}} \tag{1.21}$$

We then use $(\mathbf{u}_n - \mathbf{u}_i)$ expression from equation (1.20) in equation (1.21), along with $\nu_{in}\rho_i = \nu_{ni}\rho_n$ and $\nu_{en}\rho_e = \nu_{ne}\rho_n$ to find the fluid equation of motion as:

$$\rho_n\left[\frac{\partial \mathbf{u}_n}{\partial t} + (\mathbf{u}_n \cdot \nabla)\mathbf{u}_n\right] = -\nabla P + \mathbf{J} \times \mathbf{B} \tag{1.22}$$

where $P = P_e + P_i + P_n$ is the total pressure, and terms proportional to m_e were neglected. It is worth noting that the neutrals are subjected to the Lorentz force due to the ion-neutral collision coupling. We use the expression for electric field from equation (1.18) and the expression for the relative velocity of the ion and the neutral fluid from equation (1.20) to write the Faraday law of induction as:

$$0 = \underbrace{\frac{\partial \mathbf{B}}{\partial t} - \nabla \times (\mathbf{u}_n \times \mathbf{B}) + \nabla \times \eta'\mathbf{J}}_{\text{MHD induction equation}} + \underbrace{\nabla \times \left(\frac{\mathbf{J} \times \mathbf{B}}{en_e}\right)}_{\text{Hall}} - \underbrace{\frac{\nabla \times ((\mathbf{J} \times \mathbf{B}) \times \mathbf{B})}{\nu_{in}\rho_i(1 + \nu_{ne}/\nu_{ni})}}_{\text{ambipolar}} \tag{1.23}$$

Name	Term	Solar Prominence	Laboratory Arched plasma
Hall term	$c/(\omega_{pi}L)$	8.3×10^{-8}	0.85
Ambipolar term	$(t_A\nu_{in}(1+\nu_{ne}/\nu_{ni}))^{-1}$	1.2×10^{-6}	0.20
Resistive term	S'^{-1}	2.4×10^{-10}	1.5×10^{-3}

Table 1.2: Comparison of the equation (1.24) terms magnitude estimates for a typical solar prominence [20, 11] and the arched laboratory plasma in our experiments. For solar prominence we used $n_e = 3 \times 10^{10}$ cm^{-3}, $n_e/n_n = 0.5$, $T = 8000$ K, $B = 5$ Gauss. The arched plasma parameters used for these estimates are listed in table 2.2

where the resistivity $\eta' = \frac{\nu m_e}{e^2 n_e}$, is now dependent on the electron-neutral collision frequency through $\nu = \nu_{en} + \nu_{ei}$. We follow the same method of section 1.6.1 and use equation (1.15) to estimate the magnitude of each term in equation (1.23).

$$0 = \underbrace{\frac{\partial \overline{\mathbf{B}}}{\partial \bar{t}} - \overline{\nabla} \times (\overline{\mathbf{u}_n} \times \overline{\mathbf{B}}) + \frac{1}{S'}\overline{\nabla} \times \overline{\nabla} \times \overline{\mathbf{B}}}_{\text{MHD induction}} + \underbrace{\frac{c}{\omega_{pi}L}\overline{\nabla} \times \left(\frac{(\overline{\nabla} \times \overline{\mathbf{B}}) \times \overline{\mathbf{B}}}{\overline{n}}\right)}_{\text{Hall term}} - \underbrace{\frac{1}{t_A\nu_{in}(1+\nu_{ne}/\nu_{ni})}\overline{\nabla} \times \left(\frac{((\overline{\nabla} \times \overline{\mathbf{B}}) \times \overline{\mathbf{B}}) \times \overline{\mathbf{B}}}{\overline{n}_i}\right)}_{\text{ambipolar}} \tag{1.24}$$

where the Lundquist number $S' = v_A L\mu_0/\eta'$ is now dependent on the electron-neutral collision frequency. The first two terms of the induction equation are again of the order of unity. The resistive term of the induction equation is proportional to $1/S'$. The Hall term has the same form as in the two-fluid model of equation (1.16) and is of the order of $c(\omega_{pi}L)^{-1}$. Lastly, the ambipolar term is on the order of $(t_A\nu_{in}(1+\nu_{ne}/\nu_{ni}))^{-1}$. With this in hand, we estimate the magnitude of each term for a sample solar prominence and our arched laboratory plasma. This will aid us in gauging how well our experiment captures the essential physics of the solar prominences and the arched plasma structures of the lower solar atmosphere. The estimates of each term are listed in table 1.2 for arched laboratory plasma and a typical solar prominence. The resistive term is the smallest one for both environments. In the case of a solar prominence, the ambipolar term is estimated to be

larger than the Hall term. The ambipolar and Hall terms are on the same order of magnitude in the laboratory. One term can dominate the other depending on the experimental parameters and the location along the arch. Based on this analysis, we conclude that ambipolar and Hall effects significantly impact both solar structures and our laboratory arched plasma. It is important to note that this work does not aim to simulate arched solar structures exactly. This would require plasma production with parameters outside of our experimental capabilities and generally would be extremely difficult, if not impossible. Instead, we focus on laboratory arched plasma that lies in regimes relevant to those found in solar counterparts. As shown in this and the previous sections, the arched plasma under study is affected by the same non-ideal effects as the solar structures. While it's not a perfect simulation, the essential physics we capture in our experiments is still relevant to what we observe on the Sun.

1.7 Outline of this dissertation

The primary goal of this dissertation is to unravel certain aspects of the dynamics of arched magnetized plasma structures akin to those found in the solar atmosphere. The experimental setup was carefully designed to capture the essential physics of similar structures on the Sun. The details of the experiment, methods, and diagnostics are described in chapter 2. We investigated the role of the strength and direction of the nearly horizontal strapping magnetic field on the evolution and morphology of the arched plasma. The process and results of these studies are presented in chapter 3. The presence of a strong strapping magnetic field in the system introduces a substantial shear to the guiding magnetic field. We observed and studied a jet-like structure erupting from the arched plasma in strong magnetic shear conditions. Chapter 4 offers details on that research. Finally, chapter 5 offers final conclusions, remarks, and suggestions on future work that could be conducted on this experiment.

CHAPTER 2

Experimental Methods

2.1 The Solar Plasma Device (SPD)

All experiments conducted for this dissertation were performed on the Solar Plasma Device (SPD), a linear plasma device located at the Basic Plasma Science Facility (BaPSF) at the University of California, Los Angeles. This device is built from a five-meter-long and one-meter diameter stainless-steel cylindrical vacuum chamber (see figures 2.1 and 2.2). Around 30 radial ports along the machine are built to facilitate the use of in-situ probes, diagnostics, antennas, and other devices. Ten of these ports are fitted with ball-valve vacuum feed-throughs that allow for a full range of motion of the probe mounted on them. Anytime a Cartesian coordinate system is mentioned in this work, it refers to the one indicated in figure 2.2. Here the origin is set in the middle of the device (on the cylindrical axis), on the plane cutting through the center of both arched plasma electrodes. The y-axis points vertically up, and the x-axis points away from the arched plasma source, towards the side with access ports, and along the horizontal direction. Finally, the z-direction is along the cylindrical axis of the device, towards the main (background) plasma source. The vacuum chamber is pumped down to a nominal 10^{-7} torr pressure using a turbomolecular pump in tandem with a standard roughing vacuum pump. During operation, the chamber is filled in a controlled manner with neutral ultra-high purity helium using a mass-flow-controller (to about 5-9 mtorr). Helium gas constantly flows into the chamber to keep the purity high as the pump gate valve is held open at around 30%.

The experimental conditions, namely the magnetic field strength and direction, gas pressure,

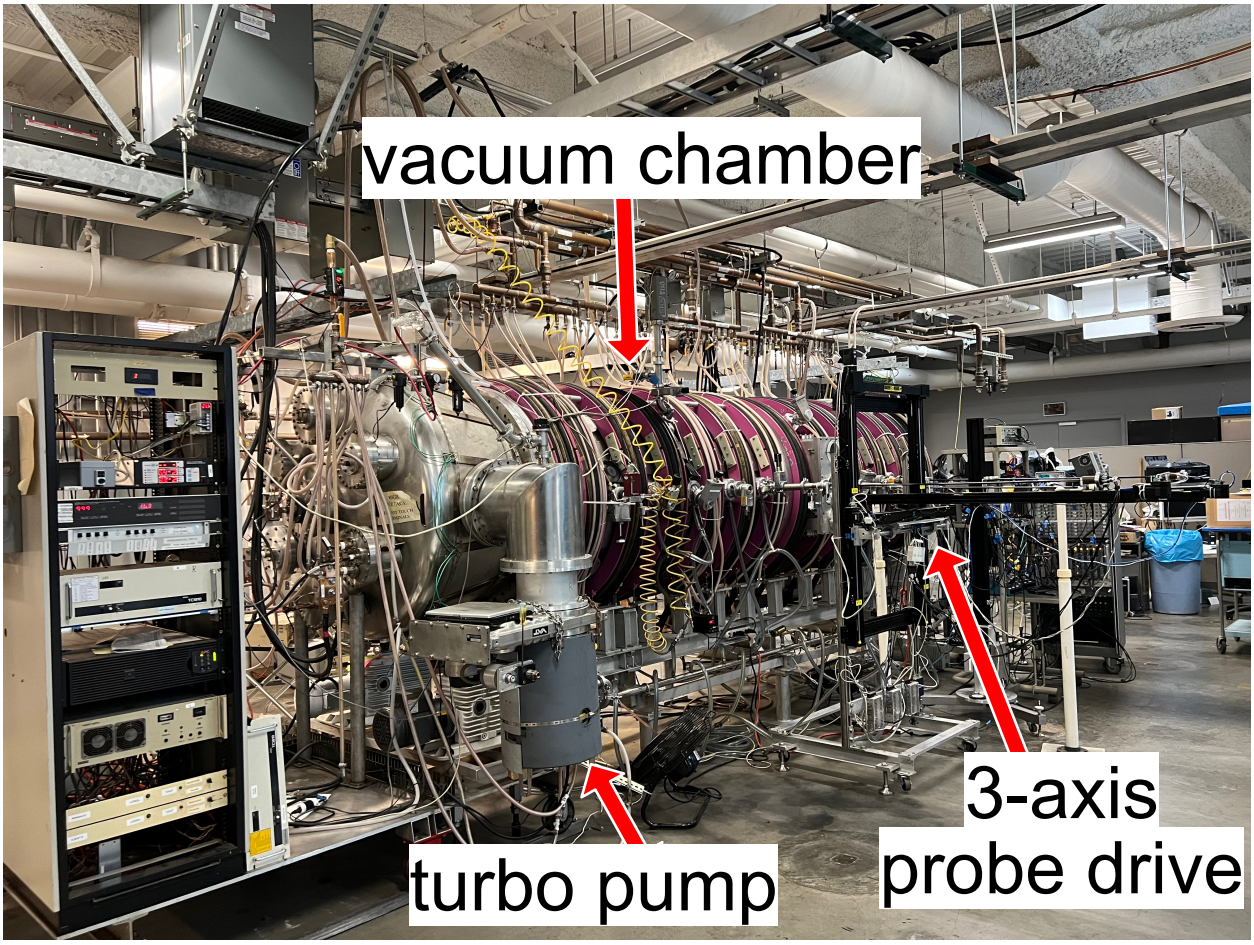

Figure 2.1: A photograph of the Solar Plasma Device (SPD)

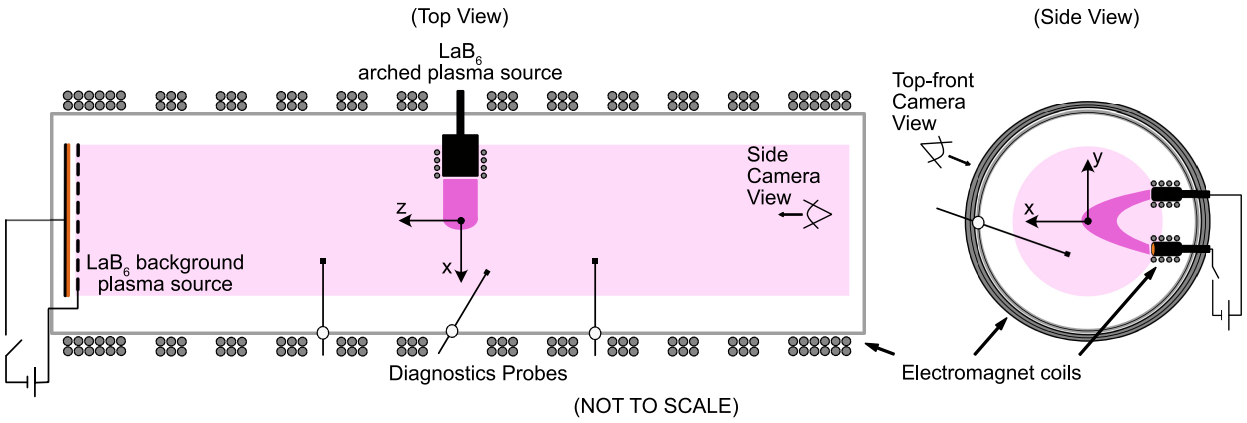

Figure 2.2: Schematic of the experimental setup depicting cross-sections of the vacuum chamber from the top (left panel) and side (right panel) views. The coordinate system used throughout this work and its origin are indicated on both panels. The origin is located on the axis of the vacuum chamber, in front of the arched plasma source, as indicated in both panels. The ambient (or background) plasma column is highlighted by a light pink. The arched plasma is shown in a dark-pink color in both views. The in-situ diagnostic probes enter the chamber through ball valves mounted on the chamber wall opposite the arched plasma source. Two camera locations mentioned later are noted on the diagram. The combination of the magnetic field generated by larger electromagnets outside the chamber and smaller electromagnets around footpoints of the arched plasma provides flexibility in simulating a variety of magnetic field configurations.

and various timing settings, are controlled manually. The rest, constituting quite a large portion of the experiment, is automated and computer-controlled. In the past, multi-function data acquisition and device control (DAQ) software was written in LabView for the LaPD machine (Large Plasma Device at the same facility). This software was then copied and adapted for use on the SPD machine. It is installed on a Windows 10 operating system data acquisition computer. This DAQ software allows for expansion with user-written modules to operate new devices (e.g., probe motion devices, digitizers, oscilloscopes).

2.1.1 Background Plasma Production

SPD has two plasma sources: the main (background) plasma source and the arched plasma source. The former produces a cylindrical plasma column along the axis of the device. It was found that the presence of the background plasma aids the formation of the arched plasma in experiments presented here. The arched plasma structures on the Sun usually evolve in the presence of background plasma (that may have different parameters), so we employed it in some of the experiments reported later on. We used a hot Lanthanum hexaboride (LaB_6) cathode and Molybdenum mesh anode discharge for ambient plasma production. The cathode (20 cm x 20 cm) comprises four equally sized LaB_6 crystal tiles mounted in front of a carbon heating element. The electrical current ($\approx$ 350 A, 70 V) passing through the resistive carbon indirectly heats the cathode to about 1700°C. At this temperature, the LaB_6 crystal becomes efficient at thermionic electron emission [91]. Right in front of the cathode, a carbon mask is installed to ensure a cylindrical shape of the plasma column ($\approx$ 20 cm diameter). A molybdenum wire-mesh square anode (40 cm x 40 cm) is mounted 30 cm away from the cathode. This electrode pair is connected to the discharge pulser, a large capacitor bank (V_{max} = 200 V, I_{max} = 2.5 kA, C = 2.34 F) charged with a DC power supply usually to around 100 Volts. An electronically controlled and timed switch closes the circuit with a user-defined repetition rate (typically 2 seconds). The voltage applied between the two electrodes accelerates the primary electrons emitted from the hot cathode toward the mesh anode. Only a small fraction of the electrons are collected on the mesh anode. Most electrons pass through and

travel along the length of the device, collisionally ionizing the neutral helium gas on their path. Some of the secondary electrons (ionized by primaries) are collected on the anode to close the current path with the floating discharge pulser. The ambient plasma is usually confined with an axial magnetic field in a magnetic mirror configuration (30 Gauss in mid-section and 80 Gauss on end magnets). Typical background plasma parameters are listed in table 2.1. Each discharge can be set to a custom duration, nominally, and for this work, that is 10 ms. This plasma production method is mirrored from a recently upgraded sibling device in the same facility - LaPD (Large Plasma Device) - which serves as a user facility for a broad range of research [92, 93].

2.1.2 Arched Plasma Production

The arched plasma source is installed in the middle of the vacuum chamber on the side wall (see figures 2.2 and 2.3). It is mounted on a large rectangular side port which allows for removing the source assembly for maintenance and repairs. The general principles behind the arched plasma production are the same as for the background plasma. Two electrodes are lined up vertically with adjustable separation (usually 20 cm center-to-center). The bottom electrode serves as a hot cathode, while the top is a 15 cm-diameter copper disk anode. The hot cathode in this assembly is a LaB_6 crystal disk of 7.6 cm diameter mounted within a custom-made carbon block. Immediately behind it, there is a carbon heater element that indirectly heats the cathode to around 1900°C. The heater element is electrically insulated from the carbon block and the cathode. In regular operation, a 340 A current is driven through the heating element at around 12 Volts using a DC power supply. The cathode is connected to its own discharge pulser, synced with the main trigger. The delay can be customized to produce the arched plasma either during or right after (afterglow) the ambient plasma. The capacitor bank used here (V_{max} = 450 V, C = 52.5 mF) is usually charged to around 350 Volts. When triggered, the pulser closes the circuit driving primary electrons from the cathode to the anode. These energetic electrons collisionally ionize the background helium gas, producing plasma, which carries electrical current between the electrodes. Most of the voltage applied between the electrodes drops in a thin sheath (thickness $<$ 0.1 mm $<<$ arched plasma

Parameter	Value	Unit
Discharge Time	10 – 15	ms
Axial plasma length	≈ 4	m
Azimuthal plasma diameter	≤ 0.6	m
Plasma density	1×10^{12}	cm^{-3}
Plasma beta	$\approx .2$	–
Electron temperature	≈ 5	eV
Ion temperature	≤ 0.1	eV
Magnetic Field	15 – 80	Gauss
Electron gyroradius	1.7×10^{-1}	cm
Ion gyroradius	2.2	cm
Debye length	1.6×10^{-3}	cm
Ion sound speed	1.4×10^{6}	cm/s
Alfvén velocity	3.3×10^{6}	cm/s
Ion cyclotron frequency	1.1×10^{4}	Hz
Electron cyclotron frequency	8.4×10^{7}	Hz
Ion plasma frequency	1.3×10^{8}	Hz
Ionization fraction	$\approx 1 \times 10^{-2}$	–
Ion-neutral collision frequency	5.4×10^{5}	Hz
Electron-neutral collision frequency	2.3×10^{7}	Hz
Electron-ion collision frequency	3.1×10^{6}	Hz
Ion-neutral mean free path	2.9×10^{-1}	cm
Ion-plasma mean free path	1.8×10^{-2}	cm

Table 2.1: Typical background plasma parameters. Some parameters are calculated assuming usual conditions: Helium gas and the magnetic field strength of 30 Gauss.

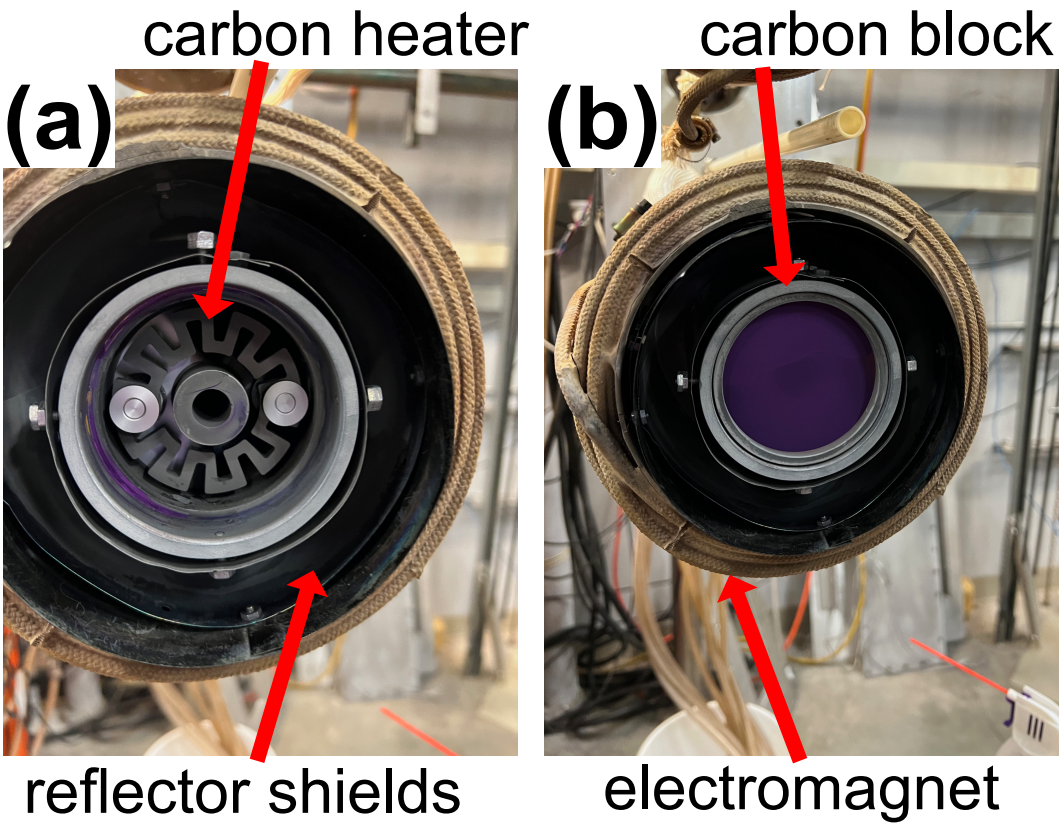

Figure 2.3: Photographs of the arched plasma source hot cathode assembly with lanthanum hexaboride (LaB_6) crystal **(a)** removed, and **(b)** installed. The electromagnet coil is wound on the outermost layer. Multiple thermal shields made of molybdenum and tantalum are installed. The carbon heating element visible in panel (a) is mounted on two tungsten rods and held in place by two tungsten nuts on each side. The LaB_6 crystal fits on the notch right above the heating element. It is then secured with a carbon ring, fixed by a set of four screws.

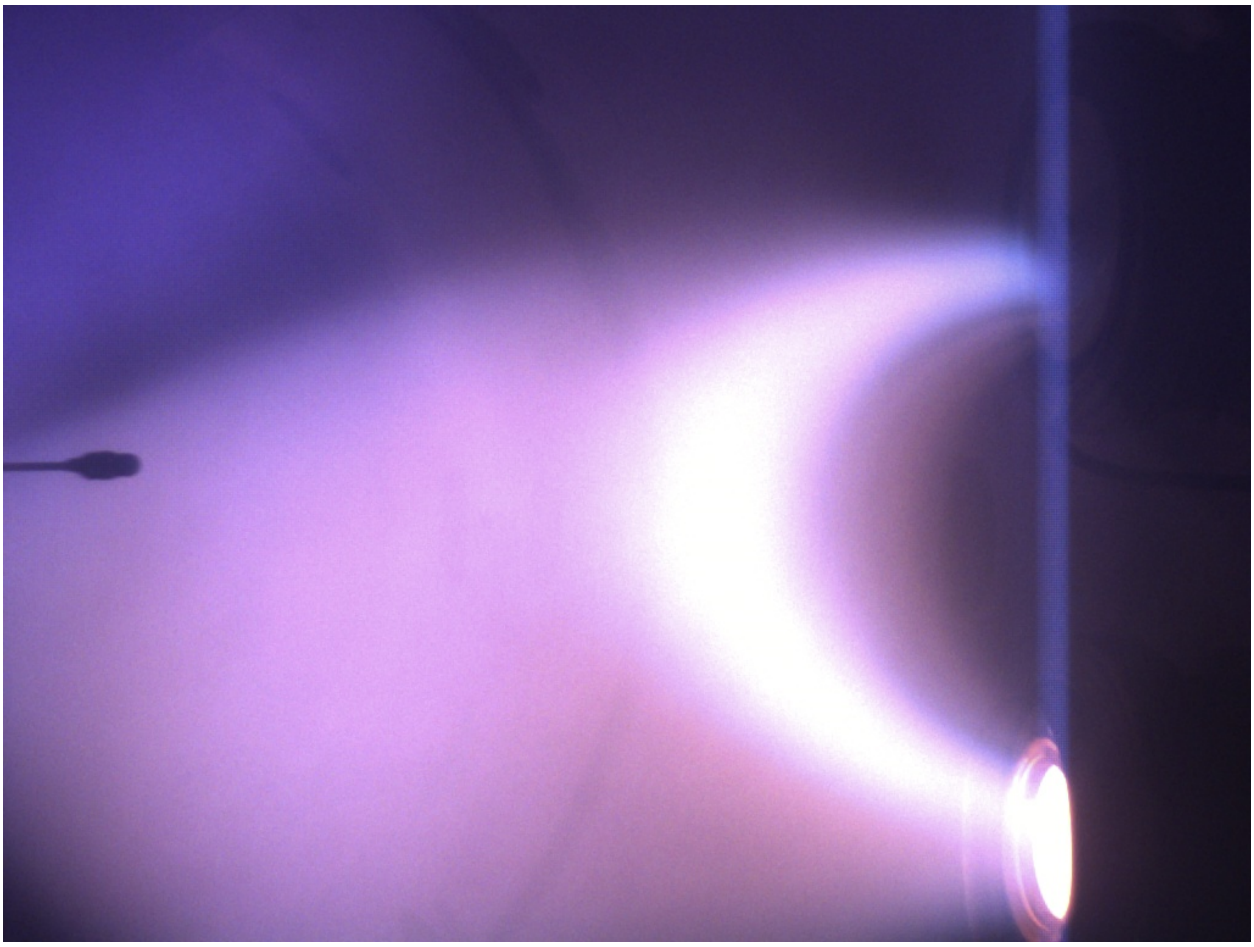

Figure 2.4: A fast camera picture of a typical arched plasma discharge captures the b-dot probe during data acquisition.

length), such that the dynamics of the plasma are not affected by the discharge voltage. The arched plasma follows the guiding magnetic field B_{guid} discussed in section 2.1.3. The electrodes in this setup are also footpoints to which the arched plasma is tied, imposing a line-tied boundary condition. The separation between the footpoints of the arched plasma can be varied in the range of 15 - 41 cm. Typically, the arched plasma has $n_e = 1 \times 10^{13}$ cm^{-3}, $T_e = 13$ eV, Alfvén transit time $\tau_A = 2$ μs, and resistive diffusion time $\tau_R = 500$ μs. Usually, the discharge duration for this plasma is set to 400-600 μs. A photograph showing a typical arched plasma discharge seen from the side is presented in figure 2.4. Typical arched plasma parameters are listed in table 2.2.

Parameter	Value	Unit
Discharge Time	400 – 600	μs
Toroidal plasma length	≈ 50	cm
Minor radius	≤ 15	cm
Plasma density	$\approx 1 \times 10^{13}$	cm^{-3}
Plasma beta	10^{-3} – 10^{-1}	–
Electron temperature	≈ 15	eV
Ion temperature	≈ 0.3	eV
Magnetic Field	10 – 900	Gauss
Electron gyroradius	8.6×10^{-2}	cm
Ion gyroradius	1.1	cm
Debye length	8.5×10^{-4}	cm
Ion sound speed	2.3×10^{6}	cm/s
Alfvén velocity	3.5×10^{6}	cm/s
Ion cyclotron frequency	3.8×10^{4}	Hz
Electron cyclotron frequency	2.8×10^{8}	Hz
Ion plasma frequency	3.3×10^{8}	Hz
Ionization fraction	10^{-1} – 10^{-2}	–
Ion-neutral collision frequency	8.6×10^{5}	Hz
Electron-neutral collision frequency	3.7×10^{7}	Hz
Electron-ion collision frequency	7.7×10^{6}	Hz
Ion-neutral mean free path	3.1×10^{-1}	cm
Ion-plasma mean free path	1.5×10^{-2}	cm

Table 2.2: Typical arched plasma parameters. Here for some quantities, we assume Helium gas and conditions approximately in the middle of the arch ($\approx$ 100 Gauss). Ranges given for magnetic field and plasma beta are due to variation along the arch.

The arched plasma source assembly had an average lifetime of a few months. The heater assembly was usually the first one to fail. The repair and maintenance usually took about two weeks, during which the exact cause of each failure was determined. The necessary upgrades and improvements were developed each time in an effort to mitigate issues and extend the lifetime. Some examples of improvements include replacing a tungsten thermal shield behind the heater with a carbon shield and introducing new support points for the tungsten rods that supply the current to the heater.

2.1.3 Magnetic Field

Around the mid-section of the machine, there are ten sets of electromagnetic coils (6-turns each) and two extra coils at each end of the device with 12-turns each (see figure 2.2). The mid-section and end-section coils are constructed from a water-cooled welding cable and powered by separate 70 V / 3 kA DC power supplies. This electromagnet configuration supplies a steady and highly uniform ($\delta B/B < .5\%$) magnetic field along the cylindrical axis of the machine. The strength of that field can be varied between 5 to 500 Gauss, with the usual operation magnitude below 50 Gauss for the mid-section magnets. The direction of the field can be reversed by swapping the connections at the terminals. This magnetic field is called an overlying, ambient or strapping magnetic field throughout this work. It serves the purpose of the strapping magnetic field that inhibits the expansion of arched plasma structures on the Sun. Since this field is uniform in our experiments, its decay index is zero (more discussion on that in section 1.4).

We introduce an additional magnetic field that guides the arched plasma, B_{guid}. Its presence is highly relevant to the arched plasma structures of the Sun. Electromagnetic coils (water-cooled) are wound around each arched plasma source electrode. The electric current in each coil is driven in the opposite direction as to produce an arched magnetic field between the hot cathode and the anode. The magnitude of this magnetic field varies with distance from the source, as presented in figure 2.5. It reaches up to 900 Gauss at footpoints and then decays to around 50 Gauss at the apex of the arched plasma. This magnetic field is operated in a pulsed mode. We use a dedicated

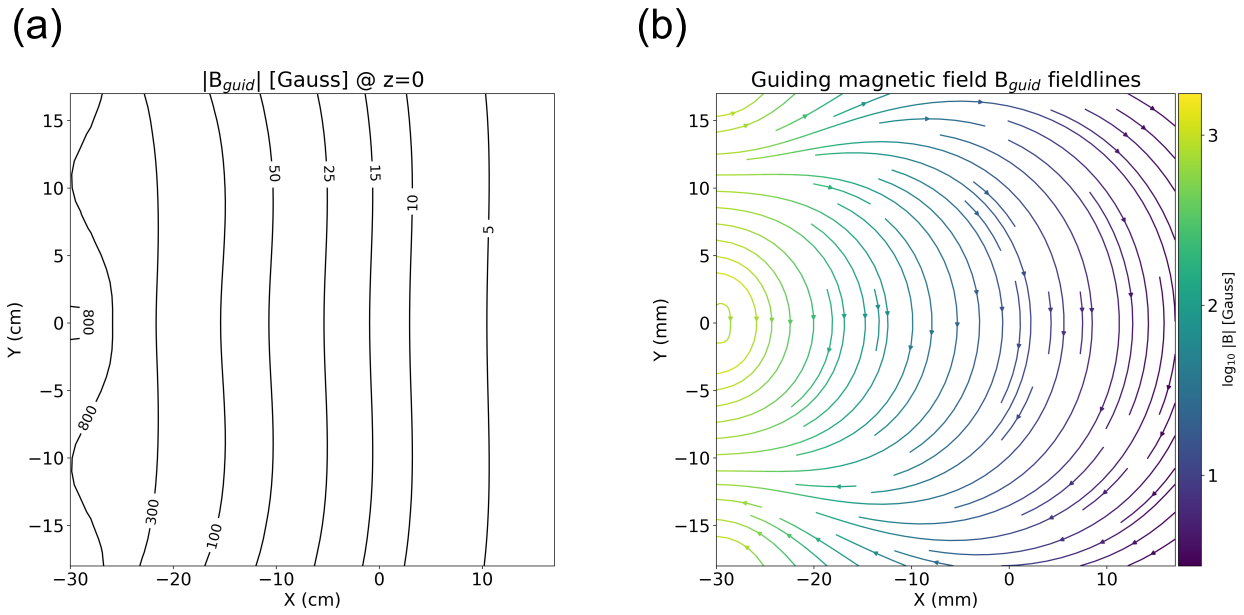

Figure 2.5: Typical magnitude and structure of the guiding magnetic field B_{guid} in the XY-plane cross-section at z = 0 cm. The data displayed here has been calculated with a Magpylib (Python package) model of the coils wound around arched plasma footpoints (located at x = -30 cm and y $\approx \pm$ 10 cm). In panel **(a)**, the absolute magnitude of the guiding magnetic field is plotted in the form of labeled contour lines. The apex of the arched plasma usually lies at around x = -10 cm, where the guiding magnetic field decays to around 50 Gauss. In panel **(b)**, a general structure of the guiding magnetic field is represented by streamlines of which color corresponds to a base-10 logarithm of the field's magnitude.

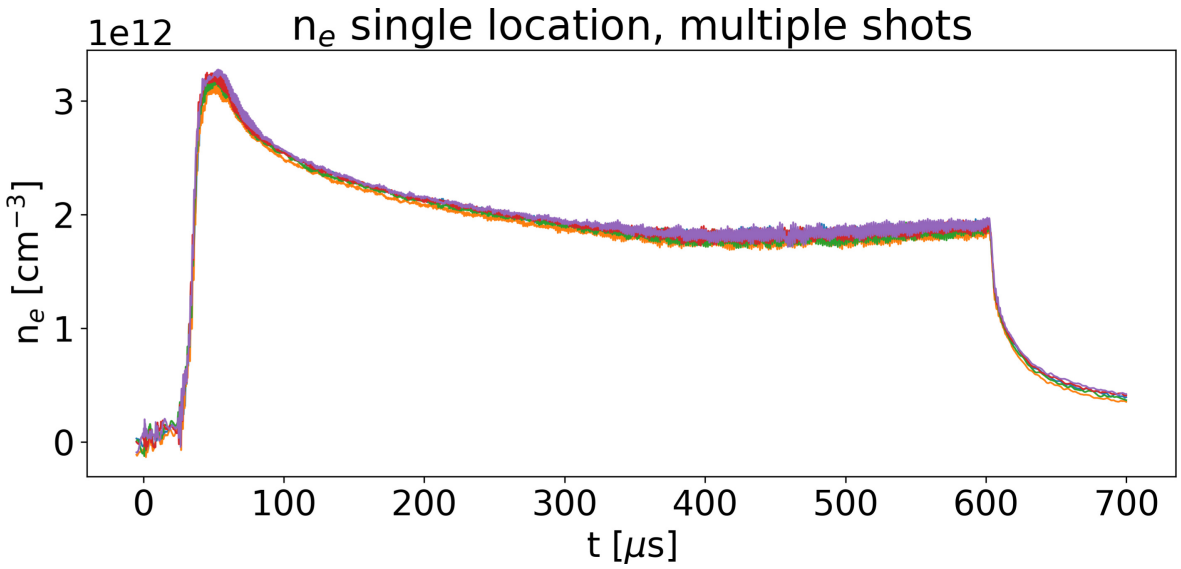

Figure 2.6: Electron density n_e in particles per cm^3 calculated from ion saturation current and temperature measured with a triple tip Langmuir probe. This plot has five traces, all corresponding to a single location in the middle of the arched plasma (x = -20 cm, y = z = 0 cm). The background field was set to 0 Gauss. Each trace corresponds to a single experimental shot. This figure illustrates the reproducibility of the experiments done at SPD.

pulser (V_{max} = 150 V, C = 0.45 F) device to power the magnets. The magnets were triggered well before the arched plasma discharge, ensuring enough time for the B_{guid} field to establish and to have a constant magnitude. The magnet pulse terminates a few milliseconds after the arched plasma discharge ends. We had the capability of reversing the direction of the guiding magnetic field by swapping the electrical connections to the magnet pulser. The magnitude of that field stayed constant throughout this work (see figure 2.5).

2.1.4 Data Acquisition

This experiment's ambient and arched plasmas are stable and reproducible, as confirmed by their persistent appearance and stationary density n and temperature T profiles (see figure 2.6). The low

variability in measured plasma parameters between experimental shots ($\delta n/n$, $\delta B/B < 0.01$) and the high repetition rate of the experiment (0.5 Hz) are crucial to the operation and data collection method used here. In-situ probes were introduced into the machine via ball valve feedthroughs (see figure 2.2), allowing their free movement inside. On the outside, each probe is mounted on a computer-controlled probe drive. We obtain a few experimental shots at each probe location to enhance the signal-to-noise ratio. The probe is then automatically moved to another pre-specified location. A few thousand shots a day are routinely recorded during normal operation. The analog signal from probes is converted to a digital form with a multichannel converter (SIS 3301). A typical sampling rate is set to 100 MHz (max allowed) with averaging set to 4 samples. The effective sampling frequency in such a case is at 25 MHz. The signal is then recorded by the DAQ software, as discussed below. A typical sequence of events of each experiment is visualized in figure 2.7.

While setting up a data run in the main DAQ software, the user can choose the number of shots per location and specify the parameters of the digitizer. These include sampling frequency, averaging window size, channels to be used, and the number of samples to collect. Once started, the software moves the probe to the first location on the user-specified grid, waits for the motion to be completed, then records a desired amount of experimental shots at that location. Each shot is saved separately as a binary file on the DAQ computer hard drive. Following that, a motion to the following location is executed, and the cycle continues until all grid points are completed. The data for each shot includes the probe's position (it is read from motor encoders and transformed to probe tip coordinates) and the signal from the digitizer. The binary data files are then compiled into one hdf5 file. This file is backed up on a remote workstation and additionally on an external hard drive. The hdf5 data file is then used to read the experimental data in the analysis work.

The data processing and analysis were conducted in Python in a Jupyter Notebook environment. Various functions and procedures were written to load, handle, format, and analyze different data collection types for the experiments discussed here. Usually, the experimental data was loaded and formatted into a multi-dimensional NumPy array formatted as [nt,ny,nx,nz,shot,chan]. The

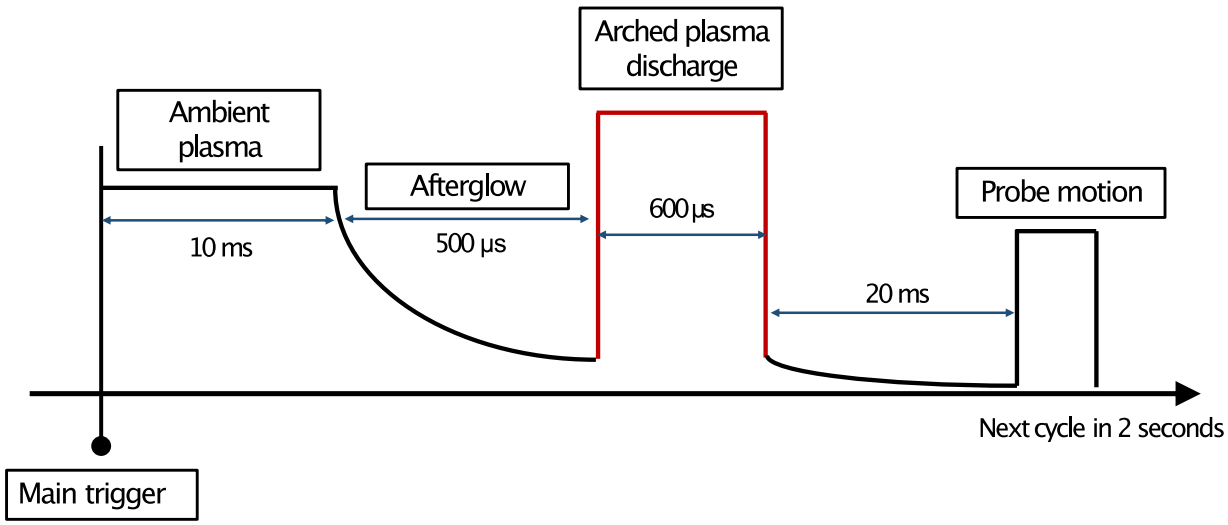

Figure 2.7: The typical timing sequence of each experimental shot at SPD. Following the main trigger, the main plasma discharge occurs during the first 10 ms. The arched plasma is usually triggered at 500 μs after the main discharge (in the afterglow) and is set to last 400-800 μs depending on the experiment. In some experiments, the arched plasma is triggered during the ambient plasma discharge, or the ambient plasma is not used at all. Once recorded, the collected shot data is saved into a binary file on the DAQ computer, and the probe is moved to a new location.

dimensions stand for the time, y-axis position, x-axis position, z-axis position, experimental shot, and the digitizer channel. From there, various techniques briefly described in the sections below were employed to extract desired plasma parameters.

2.2 Probes and Diagnostics

The diagnostic measurements were taken primarily using in-situ probes and imaging equipment. Four diagnostic probes were constructed for this project from a thin stainless steel tube (around 65" long, 0.375" diameter) coated with ceramic for thermal and electrical insulation. On one end, there is a cap with electrical feedthroughs to which appropriate electronics are connected. The other end is mounted with a specialized probe tip immersed in plasma during data collection. The probe tip is a thin alumina tube ($\approx$ 10" long, 3.5 mm diameter) terminating with a measurement assembly. A typical probe is depicted in figure 2.8.

Due to the radiative heating of the probe tip and the probe shaft from hot plasma sources, we employed appropriate materials and techniques in the probe construction. These include high temperature resistant ceramic coated wires, Kapton coaxial cables, ceramic epoxy, crimping over soldering, and avoiding unnecessary joints. The probes we built here have survived temperatures of up to 700°C. Four different probes were employed in work presented here: magnetic loop (bdot), double-tip Langmuir, triple-tip Langmuir, and Mach probe (see figure 2.9).

2.2.1 Magnetic Field (B-dot) Probe

The magnetic field probe (figure 2.9a) consists of 6 coils, two wound in opposite directions in each of the three axes. These three orthogonal coil pairs are wound on a custom-made Vespel cube (3 mm side) using a single piece of ceramic coated wire (38 AWG), ten loops for each coil. The cube is mounted on the tip of a ceramic tube and covered with an isolating ceramic cap to protect it from the harsh plasma environment. All joints are secured with a high-temperature-resistant ceramic epoxy, which also electrically insulates the coils from plasma. The wires from

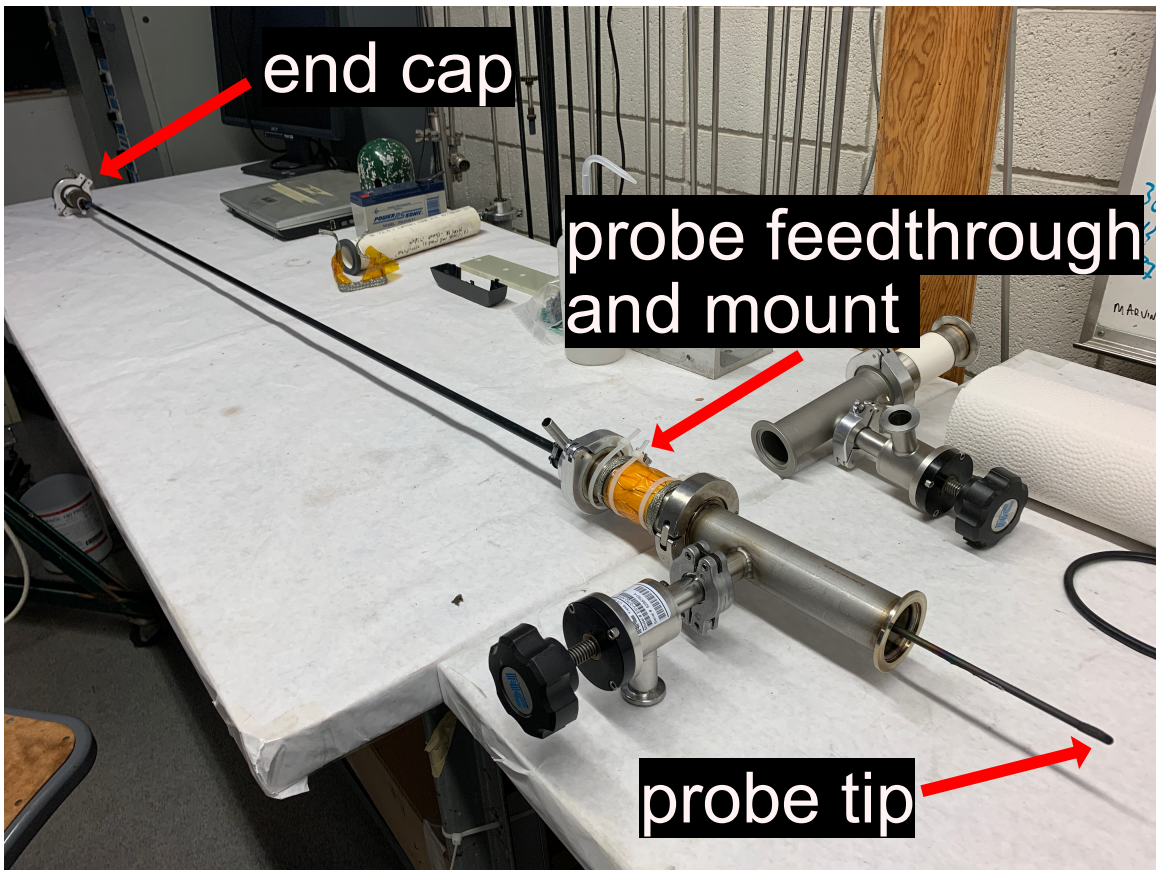

Figure 2.8: A photograph of a typical in-situ probe assembly. At the far end, there is an end cap with the electrical connections. The probe shaft goes through a probe feedthrough and mount assembly labeled in the figure. That assembly is mounted to a ball valve feedthrough of the machine allowing for a full range of motion. There is a differential pumping region that minimizes leaks through feedthrough.

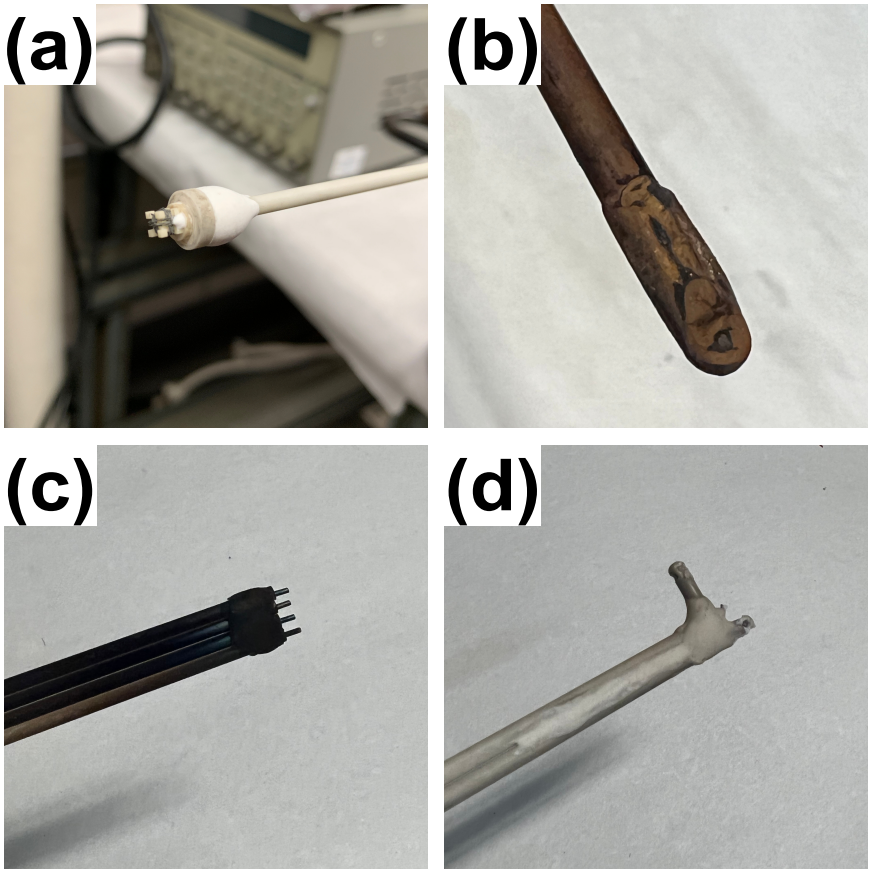

Figure 2.9: Probe tip photographs of four in-situ probes built for this project. **(a)** Magnetic loop (bdot) probe tip with a ceramic cap removed. Six thin ceramic-coated wires are looped around a custom-made cube (3 mm side) to form 6 coils used to measure the magnetic field and current density. **(b)** Double Langmuir probe consisting of two tantalum flat tips positioned on the opposite sides of the probe (only one is visible here) used to measure plasma density, temperature, and potential. **(c)** Triple Langmuir probe with four cylindrical tungsten tips used to measure time-resolved temperature, floating potential, and density. **(d)** Mach probe, which has three pairs of flat tantalum tips, each positioned along a Cartesian axis, and an extra tip for local referencing. It is used for ion flow velocity measurements. Each probe has been designed to withstand harsh plasma conditions and high temperatures resulting from close proximity to a hot-cathode arched plasma source.

each coil are fed to the other end of the probe and connected to six LEMO feedthroughs (one coil per connector). The changing magnetic field along each of the three axes induces a voltage in corresponding coils via Faraday's law:

$$V = -NAG\frac{\partial B}{\partial t}, \tag{2.1}$$

where N is number of loops, A is area of loops, B is magnetic field, G is the gain of the differential amplifier used, and t is time. Since this probe measures a fluctuating magnetic field component, it is also referred to as a b-dot probe. Each coil picks up an electrostatic signal. Therefore, each coil in an orthogonal pair is wound in the opposite direction. Then the signal from each coil in a pair is passed through an isolating differential amplifier. The electrostatic signal cancels out in such a setup while the magnetic field signal remains amplified.

The magnetic field probe data represents voltage induced in coils due to fluctuating magnetic fields. This signal is usually used to obtain the plasma's magnetic field and current density. The data collection for this probe begins before the plasma discharge occurs as to capture any changes from the baseline static fields. First, the signal from each coil pair is treated with a Savitzky-Golay filter of 1 μs window and is averaged over shots. To extract the magnetic field, we then employ the FFT integration method. The smoothed-out signal is transformed to the frequency domain via Fast Fourier Transform (FFT). We can then rewrite equation (2.1) as:

$$\tilde{B}(f) = -\frac{\tilde{V}(f)}{2\pi i f NAG} \tag{2.2}$$

where f is now frequency. The area of the probe A is affected by the internal probe circuitry effects, and in practice, this should be accounted for. We deal with this by representing the entire probe with a complex-valued impedance, which is then accounted for by replacing A in equation (2.1) with a complex-valued 'effective area' A_{eff}. Its value can be found empirically by conducting measurements with the probe in a known magnetic field configuration. We have done this using an in-house made Helmholtz coil which has a characteristically high uniformity of the field. The b-dot probe and the Helmholtz coil were then connected to the network analyzer, which records the magnitude M (in dB) and the phase θ of the probe signal relative to the input signal. The effective

area can be then obtained through:

$$A_{eff}(f) = \left(\frac{5}{4}\right)^{3/2} \frac{rR_H \times 10^{M/20}}{\mu_0 n N 2\pi f g_H} e^{i\theta} \tag{2.3}$$

where R_H, r, and n are the resistance, radius, and number of loops in the Helmholtz coil, N is the number of loops in the b-dot probe, and g_H is the gain of the differential amplifier used. With that in hand, the b-dot signal in the frequency domain is then divided by a complex-valued $(2\pi i f N A_{eff} G)$, which integrates it. We then transform the signal from each orthogonal pair to the stationary machine coordinate system as per equation (2.12) discussed in section 2.3. To eliminate any DC offset, a $f = 0$ frequency signal is removed. Finally, we transform the signal back to the time domain via inverse FFT. The result is a magnetic field in Teslas, resolved in time and space. Per Maxwell's equation, a curl of the magnetic field yields current density, which is used extensively in plasma diagnostics here.

2.2.2 Langmuir Probes

A Langmuir probe is commonly used in laboratory plasmas due to its simple construction and mode of work. The most basic version consists of a single metal tip exposed to the plasma and collecting some current based on the bias applied. Various plasma parameters can then be inferred from that signal.

2.2.2.1 Double Tip

The double Langmuir probe (figure 2.9b) consists of two tantalum flat tips (1 mm^2) mounted on the opposite sides of the probe tip and electrically insulated from one another. The metal tips are directly exposed to plasma. One tip is used for an ion saturation current measurement I_{sat}. When this tip is sufficiently negatively biased (several times greater than electron temperature), all electrons are repelled from it, and only ions are collected. This ion current saturates at a certain voltage. Usually, the I_{sat} tip is biased with respect to the chamber ground at about -70 V. The current drawn is then recorded as a voltage across a known resistor. From the Bohm sheath criterion, we know

that the formation of the sheath around the probe tip is possible only if the ions enter the sheath at a velocity approximately equal to or less than the ion sound speed $c_s = \sqrt{T_e/m_i}$ [94]. For a one ion species plasma, this gives a direct relationship between the ion density n_i and the I_{sat} as:

$$n_i = \frac{I_{sat}}{qA_s \exp(-1/2)} \sqrt{\frac{m_i}{k_b T_e}} \tag{2.4}$$

where q is a charge of the ion (usually just e for singly ionized helium), A_s is the probe sheath area, and m_i is the ion mass. The sheath around the probe tip expands with the magnitude of the negative bias, effectively increasing the collection area. However, as long as the Debye length of the plasma is much smaller than the tip's physical dimensions, it is fair to assume $A_s \approx A_t$, where A_t is the area of the probe tip. Because plasma is generally electrically neutral, the measured ion density n_i can be treated as the electron density n_e.

The voltage sweep method uses the second tip, which provides additional plasma parameters. For that, we use an in-house made floating voltage sweeper (adjustable amplitude and frequency). A typical setting would be 10 sweeps, -60 to 40 Volts over 200 μs each. The tip's current drawn in or out is measured as a voltage across a known resistor. The bias voltage is also recorded. The resulting I-V curves can then be used to obtain electron density n_e, electron temperature T_e, the plasma potential V_{pl} and the floating potential V_f [95]. The latter is the potential of the probe tip at which no net current is collected. Since ions and electrons are at different temperatures, their thermal velocities are unequal. Hence each species is collected at a probe tip at different rates. The voltage sweeps are adjusted for each experimental condition accordingly (sweep length, period, voltage range). All signals are passed through isolators before reaching a digitizer. The primary drawback of the swept method is a limited temporal resolution.

2.2.2.2 Triple Probe

A triple probe offers an instantaneous electron temperature and floating potential measurement. Moreover, the extraction of plasma parameters is more straightforward and less prone to errors when compared to the swept probe method. A triple Langmuir probe constructed here has, in fact,

four cylindrical tungsten tips (figure 2.9c). Each tip (2 mm long, 0.76 mm diameter) is mounted on a custom-made boron nitride (BN) piece to ensure electrical insulation from the probe shaft and each other. About 10" from the probe tip, each tungsten wire is crimped to a Kapton-insulated coaxial cable (26 gauge) central conductor. Each central conductor is connected to a separate LEMO feedthrough at the end cap. The shields of all cables are connected to each other and the additional feedthrough. Usually, the shields are connected to a chamber ground to reduce the noise picked up on a central conductor. Each of the four tips has its specific function. Two tips act as a double probe where one tip is biased (about 60 V) with respect to the other tip. The positive tip collects electrons, while the negative one collects ions. The current flowing between them, I_{sat}, is measured across a known resistor, recorded as voltage V_r, and later used to calculate plasma density through equation (2.4). The third tip is floating, and its potential V_t is measured with respect to the electron collecting tip across a 1 MΩ resistor. It is then used to obtain an electron temperature, as described below. The fourth tip, also floating, has potential V_{fl} measured with respect to the ground and representing the plasma floating potential. A simplified circuit diagram for this probe is presented in figure 2.10. All signals are passed through individual isolating amplifiers before being connected to a digitizer. The electron temperature is directly extracted from V_t through [96]:

$$\frac{1}{2} = \frac{1 - \exp\left(-\phi V_t\right)}{1 - \exp\left(-\phi V_{bias}\right)} \approx 1 - \exp\left(-\phi V_t\right), \tag{2.5}$$

where V_{bias} is applied between electron collecting and ion collecting tips, $\phi = e/k_B T$, and k_B is the Boltzmann constant. The factor ϕV_{bias} is usually around 7 for this experiment which permits the approximation in equation (2.5). The floating potential measured with the fourth tip, along with the electron temperature measurement, can be used to obtain the plasma space potential V_{pl} through [97]:

$$V_{pl} = V_f + \mu T_e/e \tag{2.6}$$

where the coefficient μ is determined experimentally for different gases from the swept probe I-V curve analysis. For helium in experiments conducted here, $\mu \approx 3$.

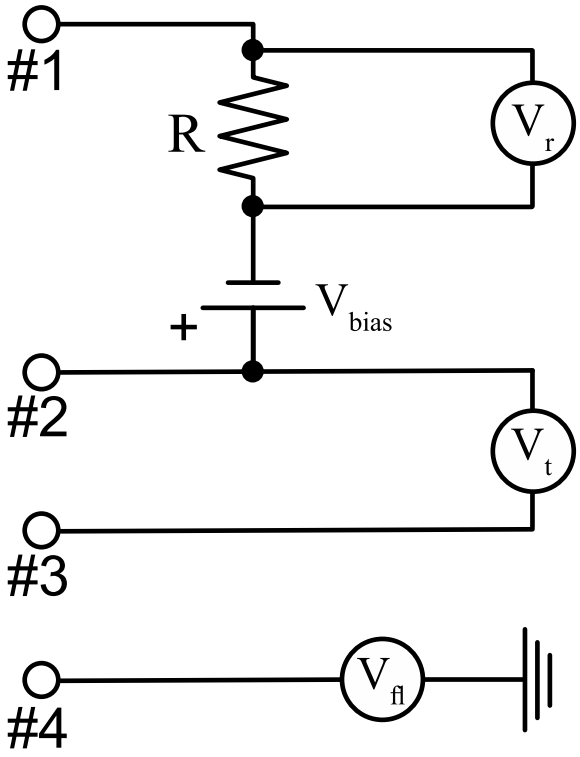

Figure 2.10: A circuit diagram for a triple probe setup showing how the probe tips were used to measure the floating potential V_{fl}, and V_t, V_r used to calculate T_e, and I_{sat} respectively.

2.2.2.3 Mach Probe

The last probe constructed for this dissertation is a three-axis Mach probe (figure 2.9d). It has a total of six tantalum flat tips ($\approx$1 mm^2 area). Three pairs are aligned along each of the three Cartesian axes, where two tips in each pair face opposite directions. In this configuration, each pair has an upstream and a downstream tip. An extra seventh tantalum cylindrical tip (2 mm long, 0.38 mm diameter) is mounted for a local potential reference. All six tips are separately biased with respect to the reference tip at about -65 Volts. The current drawn by each tip (ion saturation current) is measured as a voltage across a known resistor, passed through an isolator. The measured currents from each pair are then used to obtain the ion flow velocity with respect to the ion sound speed or the Mach number. Generally, only a tip pair that is parallel to the total magnetic field yields a reliable measurement. The ion gyration affects the current collected on tip pairs perpendicular to the magnetic field. As it turns out, however, the velocity component aligned with the field was the one of interest to us.

The ion saturation current measured on each tip is recorded and then used to obtain the flow along each axis through [95]:

$$\frac{j_{up}}{j_{down}} = \exp\left(KM\right), \tag{2.7}$$

where j_{up}, j_{down} are upstream and downstream ion saturation current densities measured, M is the mach number, and K is the calibration constant. For all plasmas studied here, the ion gyroradius is much larger than the size of the probe tip (over a factor of 10). This justifies the use of the calibration constant from [98] $K = 4\sqrt{T_i T_e}/(T_i + T_e)$, which is approximately 1.73 for experiments presented here. An extra calibration coefficient C must be experimentally determined and used to avoid systematic errors. This is due to the variance of probe tip areas, cable length between each probe tip and the digitizer, resistors used for current measurements, etc. The coefficient C is determined by comparing data from the Mach probe oriented normally, and rotated by 180°, in a weakly magnetized plasma with no flows existing. Any difference between upstream and downstream tips readings yields $C = V_{up,normal}/V_{down,inverted}$. With that obtained for each pair, the ratio of current

densities becomes:

$$\frac{j_{up}}{j_{down}} = \frac{V_{up}}{V_{down}} \cdot \frac{1}{C} \tag{2.8}$$

The Mach number extracted from each pair represents the ion flow velocity v_i in terms of the ion sound speed c_s as:

$$M = \frac{v_i}{c_s} = \frac{v_i}{(\gamma Z k_b T_e / m_i)^{1/2}} \tag{2.9}$$

where γ is an adiabatic index (usually 5/3), Z is the ion charge state, and m_i is the mass of the ion. As mentioned before, this probe is most reliable for flows parallel to the magnetic field. It is therefore used primarily for the diagnostic of parallel flows. Nonetheless, the regions of plasma where this probe is used are weakly magnetized and highly collisional with background neutrals. For that reason, perpendicular flow measurements are not without merit (as discussed later in chapter 4). All signals from Langmuir probes were usually treated with a Savitzky-Golay filter of around a 1 μs window (less than Alfvén crossing time).

2.2.3 Imaging

Two cameras were used in this project, primarily for quick diagnostics and ensuring the performance as well as reproducibility of the plasma. Each camera was positioned at one of the two mounting points (interchangeable). One was at the end of the device on the side opposite the main plasma source. The other was in the upper front of the arched plasma source. Both are indicated in figure 2.2. For ultra-fast fps videos, we used a Phantom V7.6 camera that was usually set to 100k fps and fitted with a wide-angle lens. This provided us with plasma recordings resolved to 10 μs. The only drawback of this camera was its relatively small resolution (about 50x100 pixels at high fps) and grayscale recording mode. For still, full-color pictures with higher resolution (1024x768), we used a Cooke DiCam-Pro intensified CCD camera, synced to the main trigger. The variable delay allowed us to take pictures at different stages of the plasma evolution. Usually, the exposure time was set to 10 μs.

2.3 Three-axes Probe Drive

2.3.1 Hardware

During a typical data run, we mount a selected probe on an automated three-axis probe drive (see figure 2.11) constructed directly for this project. The probe drive has been built with four Velmex BiSlide® motorized positioning stages. While the y-axis motion is handled by two stages (coupled with a belt), the other two axes use one stage each. The motors used in this assembly (Applied Motion STM 23S-3EE) were controlled by the custom-written extension module to the data acquisition software through an Ethernet protocol. Each motor takes a command on how many steps it must rotate and in which direction. It takes 25 thousand steps for a full rotation and ten rotations for a linear motion of 1 inch. This translates to roughly 1.016×10^{-5} cm/step. This novel probe drive enables data collection in a pre-specified three-dimensional grid. Measured plasma parameters (i.e., magnetic field, density) can be visualized in a three-dimensional space allowing for more in-depth analysis and understanding of the physical phenomena.

2.3.2 Control Software

In order to implement the newly built probe drive into experimental runs, a new control module had to be developed. This module served as an extension to the DAQ software responsible for experimental control and data acquisition. The front end of the probe drive module was written in LabView, while the back end that communicates with and controls the motors was written in Python. The two communicate through TCP tunnels, which proved to be the most stable and reliable. A configuration panel for the probe drive software is depicted in figure 2.12. It lets the user specify the three-dimensional grid parameters (dimensions, resolution) and the software limits for the probe motion to avoid a collision with the chamber wall. A transformation between probe tip coordinates and the stepper motor encoder position also had to be developed. The user or the main DAQ software requests a desired probe location which is then translated to the motors' position. Drawings representing a simplified geometry of the 3D probe drive with relevant dimensions are

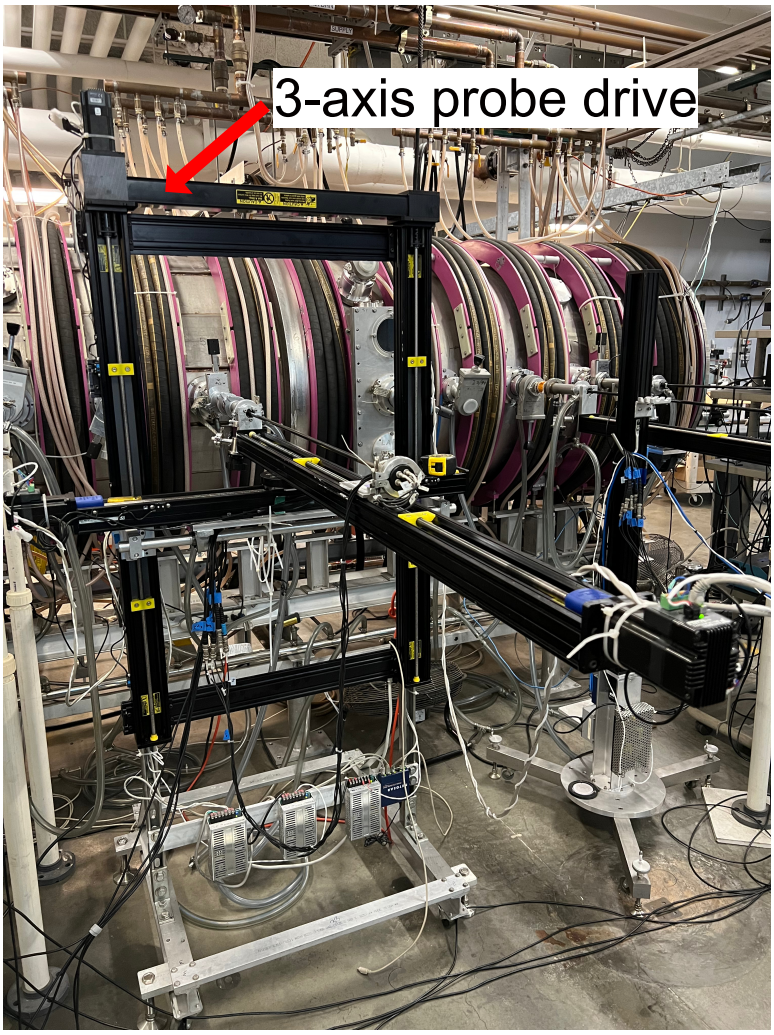

Figure 2.11: A photograph of a three-axis probe drive constructed for this project, along with a probe mounted on it. The motorized positioning stages (black) allow for an automatic probe motion across a specified 3D grid. This allows for faster data collection and the study of the measured plasma parameters in three dimensions.

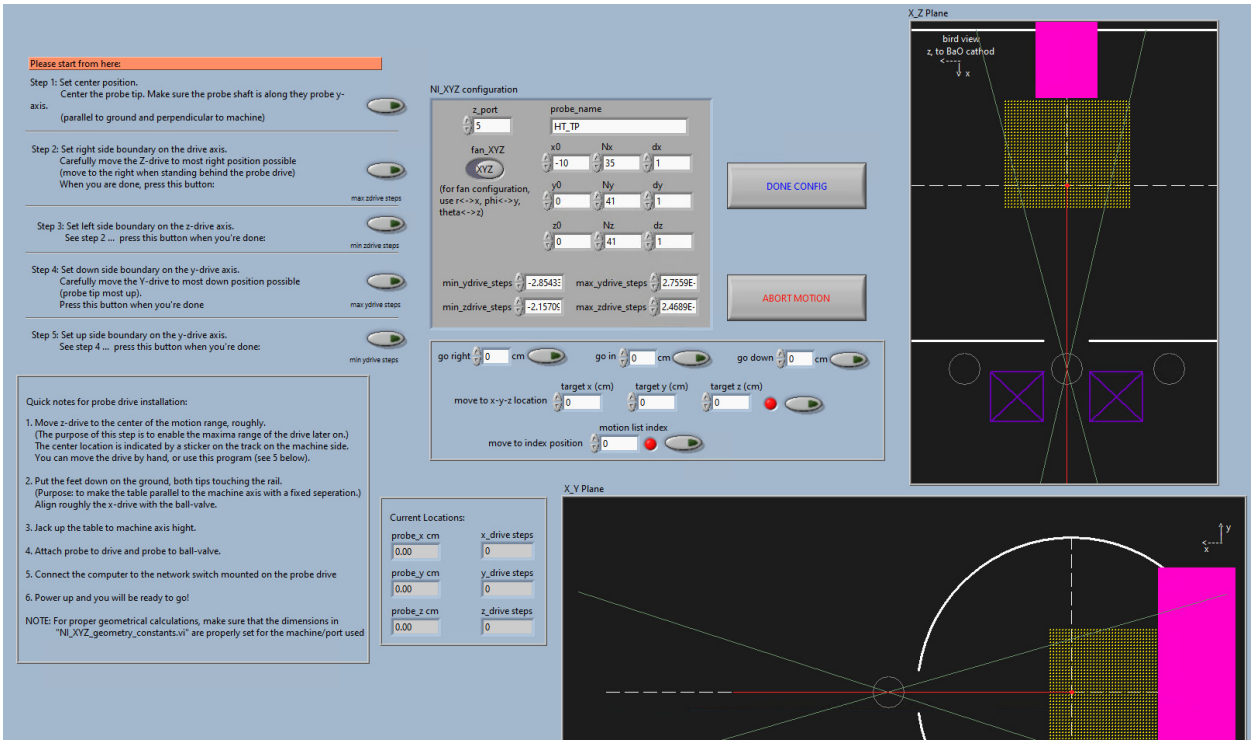

Figure 2.12: A snapshot of the configuration panel from the three-axis probe drive software was written for this project. The user can define software motion limits and define the origin of the probe coordinate system. It allows configuring a 3D grid through which the probe moves during a data run. The projections in XY and XZ displaying the grid and the current probe position are also included.

presented in figure 2.13. The transformations from probe tip coordinates to stepper motor positions in steps were determined to be:

$$
\begin{aligned}
x_D &= \rho - L_B \\
y_D &= L_T \tan\phi + L_D(\sec\phi - 1) \\
z_D &= (L_T + L_D \sin\phi)\tan\theta \\
&\text{where} \\
\theta &= \tan^{-1}\left(\frac{z_p}{L_B - x_p}\right) \\
\phi_S &= \tan^{-1}\left(\frac{y_p}{\sqrt{(L_B - x_p)^2 + z_p^2}}\right) \\
\phi &= \tan^{-1}\left(\frac{yp}{L_B - x_p}\right) = \tan^{-1}\left(\frac{\tan\phi_S}{\cos\theta}\right) \\
\rho &= \sqrt{(L_B - x_p)^2 + y_p^2 + z_p^2}.
\end{aligned}
\tag{2.10}
$$

Here, the x_D, y_D, and z_D are the displacement of carriages mounted on respective positioning stages. At the same time, x_p, y_p, and z_p are coordinates of the probe tip with respect to the machine coordinate system labeled in figure 2.2. The length of the probe shaft section from the middle of the ball valve to the probe tip is ρ, the angle θ is measured between a projection of the probe shaft to the horizontal (XZ) plane and the x-axis, while angle ϕ is measured between the projection of the probe shaft onto XY plane and the x-axis. To simplify some expressions below, an additional angle ϕ_S is introduced; it is measured between the probe shaft past the ball valve and the horizontal XZ plane. The angles and physical length constants L_D, L_T, and L_B are all indicated in figure 2.13. When requesting the position from stepper motors, it is transformed back to probe coordinates to

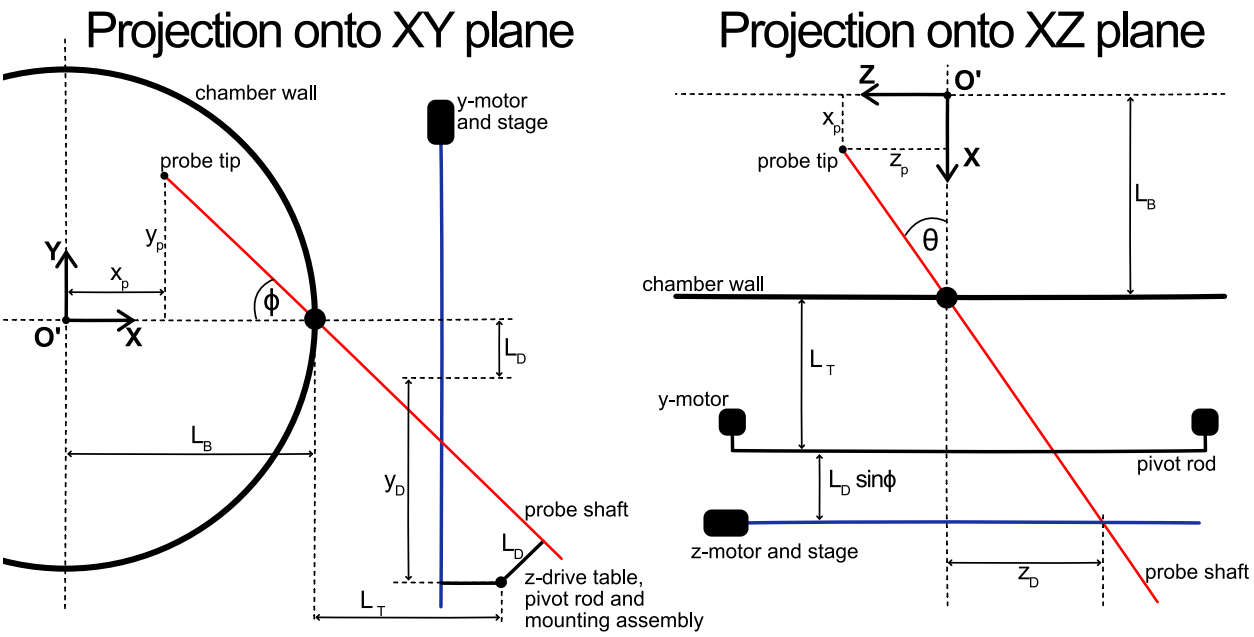

Figure 2.13: A simplified diagram of the novel three-axis probe drive built for this experiment is projected onto the XY plane (left) and the XZ plane (right). The relevant angles ϕ and θ discussed later are marked. The physical constants noted are L_D, L_T, and L_B are the length between the pivot rod and the center of the probe shaft, the distance between the center of the ball valve and the pivot rod along the horizontal, length between the center of the machine and the center of the ball valve. The probe shaft is drawn in red, while motorized positioning stages are drawn in blue. The relevant coordinate for the probe and drive are noted with appropriate subscripts. This diagram is meant to serve as a visual aid for the transformations in equations (2.10) and (2.11). It is not to scale.

be interpreted by the user and software. It is accomplished with the following inverse transforms:

$$\begin{aligned}
\rho &= x_D + L_B \\
\phi &= 2\tan^{-1}\left[\frac{\sqrt{2L_D y_D + L_T^2 + y_D^2} - L_T}{2L_D y_D}\right] \\
\theta &= \tan^{-1}\left[\frac{z_D}{L_T + L_D \sin\phi}\right] \\
\phi_S &= \tan^{-1}\left[\tan\phi \cdot \cos\theta\right]
\end{aligned} \tag{2.11}$$

then,

$$\begin{aligned}
x_p &= L_B - \rho\cos\phi_S\cos\theta \\
y_p &= \rho\sin\phi_S \\
z_p &= \rho\cos\phi_S\sin\theta
\end{aligned}$$

Finally, a transformation was required for the collected data when we utilized a probe measuring three Cartesian components of a given parameter (e.g., b-dot or Mach probe). This was to convert from moving probe tip coordinates to stationary machine coordinates. The particular construction of this probe drive introduces two rotations to the coordinate system of the probe tip. The first is a rotation by angle ϕ (described above) about the z-axis as the y-drives move up or down. Then, the motion along the z-drive introduces a rotation by angle $\beta = \arctan[\tan\theta \cdot \cos\phi]$ about the new y-axis. The transformation from probe tip coordinates (primed) to the machine coordinates (unprimed) was determined to be:

$$\begin{bmatrix} V_x \\ V_y \\ V_z \end{bmatrix} = \begin{bmatrix} \cos(\phi)\cos(\beta) & \sin(\phi) & \cos(\phi)\sin(\beta) \\ -\sin(\phi)\cos(\beta) & \cos(\phi) & -\sin(\phi)\sin(\beta) \\ -\sin(\beta) & 0 & \cos(\beta) \end{bmatrix} \cdot \begin{bmatrix} V_x' \\ V_y' \\ V_z' \end{bmatrix} \tag{2.12}$$

where $\vec{V}$ is a sample vector quantity measured.

2.4 Heater Control Software

The heating elements in both plasma sources were brought to high temperatures slowly and gradually. In efforts to extend their lifetime, the current was reduced at the end of each day and then brought back to a nominal level in the morning. A LabView software has been written to facilitate this process in an automatic and remote fashion. The power supplies delivering current to the heating elements were connected to a computer through an analog galvanic isolator and a multifunction I/O device (National Instruments USB-6001). The heater control software allows for each power supply's gradual or instantaneous current setting. With this tool in hand, the daily heater routine was dramatically sped up, allowing for more time spent on other experimental aspects.

CHAPTER 3

Evolution and Morphology of an Arched Magnetized Laboratory Plasma in a Sheared Magnetic Field

This chapter presents the results from laboratory experiments on the spatiotemporal evolution of an arched magnetized plasma in a sheared magnetic field configuration. The experiment was designed to model conditions relevant to the formation and destabilization of similar structures in the solar atmosphere. The magnitude of a nearly horizontal overlying magnetic field was varied to study its effects on the writhe and twist of the arched plasma. In addition, the direction of the guiding magnetic field along the arch was varied to investigate its role in forming either forward-S or reverse-S-shaped plasma structures. The electrical current in the arched plasma was well below the current required to make it kink unstable. A significant increase in the writhe of the arched plasma was observed with larger magnitudes of the overlying magnetic field. Forward-S-shaped arched plasma was observed for a guiding magnetic field oriented nearly antiparallel to the initial arched plasma current, while the parallel orientation yielded the reverse-S-shaped arched plasma.

3.1 Introduction

3.1.1 Background and Motivation

Arched magnetized plasma structures are ubiquitous in the solar atmosphere. Solar prominences and coronal loops are notable examples of such structures that confine a current-carrying plasma by closed magnetic fields. Magnetic loops in the solar corona have characteristically low plasma

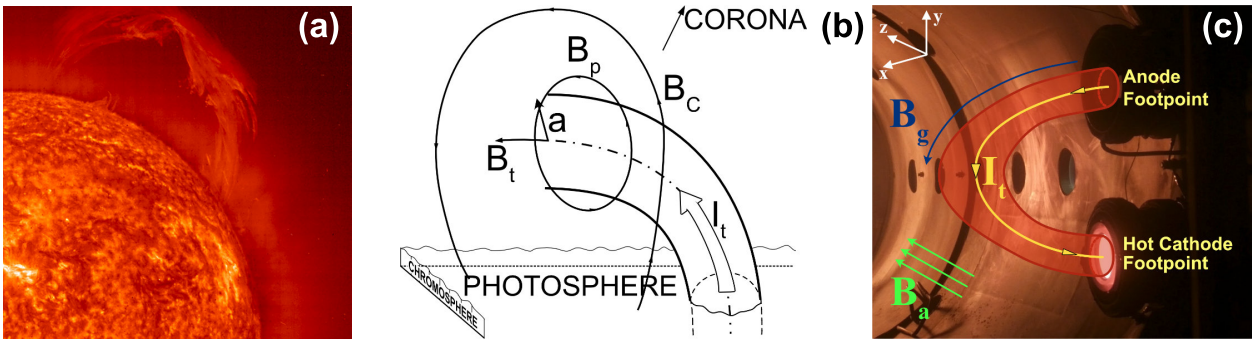

Figure 3.1: (a) A solar prominence observed in the extreme ultraviolet (EUV) wavelength of 304 Å by SOHO spacecraft on 28 March 2000 (Credit: NASA). (b) Schematic of a model flux rope in solar corona with overlying strapping field B_c. Minor radius a and flux rope current I_t are indicated. Toroidal and poloidal components of the magnetic field are B_t and B_p, respectively [adapted from [20]]. (c) Photograph of the experimental setup depicting a current filament I_t, guiding magnetic field B_g, and ambient (or overlying) magnetic field B_a. The experiment simulates the background conditions of a solar prominence shown in (b).

beta ($\beta \approx 10^{-3} - 10^{-2}$) suggesting a nearly force-free state of these structures [19, 99, 18]. A photograph of a solar prominence, a model of its structure, and the laboratory arrangement to model the prominence eruption have been depicted in figure 3.1. Solar prominences can remain stable for days to a few months [23, 24, 25, 26]. Some of these structures lose confinement sporadically and erupt due to loss of equilibrium [27, 28, 29, 30]. The relatively stable pre-eruption phase for these structures lasts for several thousands of Alfvén transit times (time taken by the Alfvén wave to travel from one footpoint of the arched plasma to another). Solar eruptive events (e.g., coronal mass ejections, solar flares, and jets) are among the most energetic events associated with plasma eruption in the solar system. It is estimated that CME eruptions and flares can release $10^{30} - 10^{33}$ ergs of energy in the form of the kinetic energy of the bulk plasma motion and/or electromagnetic radiation [20]. Such eruptive events carry adverse effects on us on Earth. A general understanding of the dynamics and the mechanism behind eruptive solar events remains limited. We hope that our work contributes to this understanding and forecasting abilities.

3.1.2 The Twist and Writhe

Modeling solar prominences in a laboratory or computer simulation often involves the creation of flux ropes - twisted magnetic structures due to significant poloidal magnetic field generated by the toroidal electrical current (see figure 3.1b) [44, 45, 46, 47]. The kink instability is a prominent candidate for triggering eruptions on the Sun. Observational signatures of this instability are usually associated with helical deformations (i.e. writhe and twist) of filaments and prominences [45, 67, 68, 69]. A kink-unstable magnetic flux rope with the electrical current along an externally imposed toroidal magnetic field, B_t, is expected to develop writhe due to the dominance of a self-generated magnetic field, B_p. Quantitatively, writhe is a measure of net self-coiling of magnetic field lines and is related to its total torsion (how sharply it is twisting out of the plane of curvature) [71]. The twist, on the other hand, measures the turning angle of a bundle of magnetic field lines around its central axis. Both writhe and twist are closely related through magnetic helicity, which quantifies the twist, writhe, and the linkage of the magnetic field [100]. Under ideal MHD assumptions (justified for solar prominences), the magnetic helicity is nearly conserved. Therefore, the twist and writhe are closely coupled with each other. The total twist, Φ, can be expressed as [72],

$$\Phi = \frac{lB_\phi(r)}{rB_z(r)}, \tag{3.1}$$

where l is the length of the flux rope, r is the minor radius, B_z is the axial magnetic field, and B_ϕ is the azimuthal magnetic field. When the twist exceeds a critical value Φ_c, the system becomes kink unstable and evolves to reduce the curvature of magnetic field lines. This process lowers the net magnetic energy of the system and effectively converts the twist into writhe [73, 74, 75, 76]. For line-tied magnetic arches (aspect ratio = major radius/minor radius $\approx$ 5), the critical value of the twist parameter, Φ_c, was estimated to be $\approx 3.5\pi$ [19].

An association between the sign of magnetic helicity and the shape of filaments was suggested by several authors [17]. It has been observed that reverse-S-shaped structures dominate the Northern Hemisphere of the Sun, while forward-S-shaped structures are more abundant in the Southern Hemisphere [101]. The writhe and twist naturally develop in a sheared magnetic configuration,

which produces sigmoidal-shaped (forward-S or reverse-S) solar filaments [71]. We note that the total twist in a sheared magnetic configuration may not be accurately estimated using equation 3.1 due to underlying assumptions of azimuthal symmetry.

3.1.3 In This Chapter

Our experiment facilitates in-situ measurements on varieties of arched current-carrying magnetized plasma (see figure 3.1c). Plasma parameters in the experiment are appropriately scaled to capture the essential physics of arched plasma on the Sun. Due to a relatively low electrical current ($<$200 A) and a poloidal twist of the magnetic field, our setup captures essential features of solar arched plasmas during the pre-eruption phase. The experiments conducted here introduce two independent plasma sources, producing the arched magnetized plasma and the background plasma. The relative magnitude of parameters in the arched and background plasma can be varied, and the magnetic field direction can be reversed. Most importantly, the electrical current in the arched plasma can be kept below the kink-instability threshold long enough ($> 50t_A$) to study the behavior and evolution of an arched plasma during the pre-eruption phase. The high reproducibility of this experiment and the ability to take measurements in three spatial dimensions allows for reconstruction and visualization of the magnetic field, current density, and other plasma parameters in three dimensions and in time.

The development of writhe in a kink-stable arched plasma in a sheared magnetic configuration was studied in this experiment. It is demonstrated that the occurrence of the kink-instability is not a necessary requirement for the formation of writhe and twist. The dependence of the writhe of the arched plasma on the magnitude of the overlying magnetic field has been examined. In addition, the parallel and antiparallel orientations of the guiding magnetic field have been correlated with the occurrence of forward-S and reverse-S-shaped arched plasmas. Contrary to our intuition, the low-β and kink-stable arched plasma in this experiment displays a non-force-free behavior, which will be shown in 3D measurements of electrical current density and magnetic field.

3.2 Experimental Setup

3.2.1 General Overview

We designed the experimental setup with the primary goal of studying the arched magnetized and current-carrying plasmas relevant to similar structures on the Sun. This is accomplished by driving an electrical current between two electrodes along an arched vacuum magnetic field (see figures 3.1c and 3.2). Foot-points of the arched plasma are anchored on electrodes imposing a line-tied boundary condition.

The experiments are performed using the Solar Plasma Device at UCLA. A cylindrical vacuum chamber (5.0 m long, 1.0 m diameter) is filled with helium, a background neutral gas (pressure: 5 - 9 mtorr). As shown in figure 3.2, multiple electromagnets are placed around the vacuum chamber to produce a near uniform and up to 300 Gauss axial magnetic field inside the chamber. The axial magnetic field confines the ambient cylindrical plasma. It also provides an overlying (ambient) magnetic field for the arched plasma, which impacts the eruption dynamics. The guiding magnetic field (900 G at foot-points) is produced using two smaller electromagnets that surround the cathode and anode (the foot-points of the arched plasma, see the side-view in figure 3.2). The ambient plasma is produced by a lanthanum hexaboride (LaB_6) hot-cathode source (≈20 cm diameter). A discharge is created between this emissive cathode and a molybdenum wire-mesh anode that is located 30 cm away. This plasma source is placed at one end of the vacuum chamber and connected to a discharge pulser (V_{max}: 200 V, I_{max}: 2.5 kA, Repetition rate: 0.5 Hz, pulse-width: 15 ms). The cathode is indirectly heated up to 1700°C. At this temperature, it becomes efficient in the thermionic emission of electrons [91]. The ambient plasma (0.6 m diameter, 4 m long, plasma density $n_e = 10^{12}$ cm^{-3}, electron temperature $T_e = 4$ eV, pulse-width = 10-15 ms) is produced by the acceleration of primary electrons from the cathode during the discharge pulse. The arched plasma (pulse-width = 0.2-0.8 ms) is created using another cathode/anode pair. The anode is a 15 cm diameter copper disk and the cathode is a 7.6 cm diameter indirectly heated LaB_6 disk (temperature ≈ 1800°C). This anode/cathode pair is mounted on two side ports on the

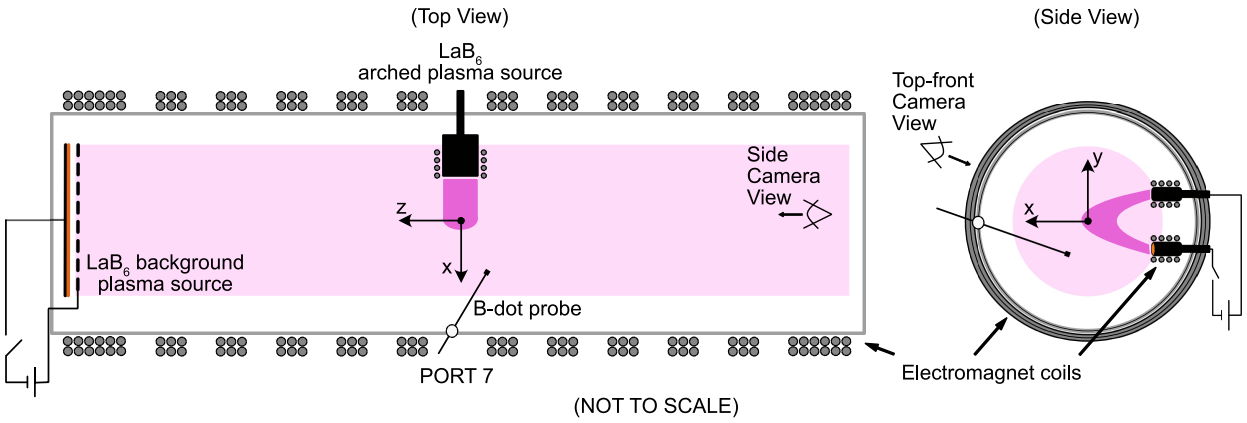

Figure 3.2: Schematic of the experimental setup for studies of this chapter, depicting cross-sections of the vacuum chamber from the top (left panel) and side (right panel) views. The coordinate system used throughout this work and its origin is indicated on both panels. The origin is located on the axis of the vacuum chamber, in front of the arched plasma source, as indicated in both panels. The ambient (or background) plasma column is highlighted by a light pink color. The arched plasma is shown in a dark-pink color in both views. The combination of the magnetic field generated by larger electromagnets outside the chamber and smaller electromagnets around footpoints of the arched plasma produces a sheared magnetic configuration and provides flexibility in simulating varieties of force-balance scenarios for the arched plasma evolution. For experiments in this chapter, we used the b-dot probe at port 7 of the SPD machine.

	Solar Prominence	Laboratory Arched plasma
Plasma β	10^{-1} - 10^{-3}	10^{-1} - 10^{-3}
r/r$_i$	10^{9} - 10^{10}	10^{2}
Lundquist number	10^{10}	10^{3} - 10^{4}
Experiment timescale / τ_A	150	200
Resistive diffusive time / τ_A	10^{10}	$>$500
Aspect ratio	5	3

Table 3.1: Comparison of the relative plasma parameters of a typical solar prominence [20, 11] and the laboratory arched plasma.

chamber. Typically, the arched plasma has $n_e = 5 \times 10^{13}$ cm^{-3}, $T_e = 13$ eV, Alfvén transit time $\tau_A = 2$ μs, and resistive diffusion time $\tau_R = 500$ μs. The arched plasma source uses a floating power supply, and it operates in sync with the ambient plasma source. A detailed discussion on plasma production and the experimental system can be found in chapter 2. Both electrodes reside in the $z = 0$ symmetry plane, at $x = -28$ cm and $y = \pm$ 13.5 cm (coordinate system depicted in figure 3.2). Typical relative parameters of the arched plasma and a quiescent solar prominence are presented in table 3.1.

3.2.2 Diagnostics

This experiment uses a computer-controlled 3D probe drive system and a multichannel digitizer to acquire high-resolution 3D data. A three-axis magnetic probe is the main diagnostic tool. A dual-tip Langmuir probe was also used for general plasma diagnostics (temperature and density). These probes are built using high-temperature ceramic coated wires and other components that can withstand up to 750°C temperature near the cathode foot-point of the arched plasma. This setup allows for a reliable and efficient measurement of plasma parameters (n, T_e, B) with a good spatiotemporal resolution (spatial resolution $\Delta x = 1.5$ cm, temporal resolution $\Delta t = 4 \times 10^{-8}$

s for the results reported here). The experiment is highly reproducible, and it operates with a 0.5 Hz repetition rate. This facilitates the measurement of the key plasma parameters in 3D. A fast intensified CCD camera (5 ns minimum exposure time, 1280 x 1024 resolution, and 12-bit digital converter) is used to record the images of the plasma from two different perspectives (side and top-front views as marked in figure 3.2). All the diagnostics are described in detail in chapter 2.

3.3 Results and Discussion

We conducted a series of experiments under different magnetic field configurations to examine the effects of the overlying magnetic field magnitude and the guiding magnetic field direction on the evolution of an arched magnetized plasma. The arched plasma current was varied in the range of 50-150 A. Typical time traces of the arched plasma current and voltage are presented in figure 3.3. It is evident that the arched plasma current evolves on time scales much faster than the resistive diffusion time ($\tau_R \approx 500$ μs). During earlier stages of evolution ($t < 100$ μs), the poloidal magnetic flux in the arched plasma gradually builds up, which leads to dynamic and eruptive behavior. A quasi-steady state of the arched plasma (nearly persistent appearance with low-frequency global oscillations) is identified at later stages ($t > 100$ μs).

3.3.1 Imaging of the Arched Plasma Profile

Unfiltered images of the arched plasma are presented in figure 3.4. These images were recorded along the z-axis using the fast camera (located at $z = -3$ m, see figure 3.2). Three panels in this figure were captured at three different overlying magnetic fields (0, 30, and 60 Gauss) at 300 μs after the arched plasma discharge initiation, corresponding to the final stage of the arched plasma evolution. Figure 3.4a corresponds to a case with no overlying magnetic field, where the plasma evolves to a uniform arch. Significant changes in the morphology of the arched plasma are evident at higher overlying magnetic fields, most notably the appearance of a bright S-shaped region (see figure 3.4c). The main role of the overlying magnetic field in affecting the dynamics of the arched

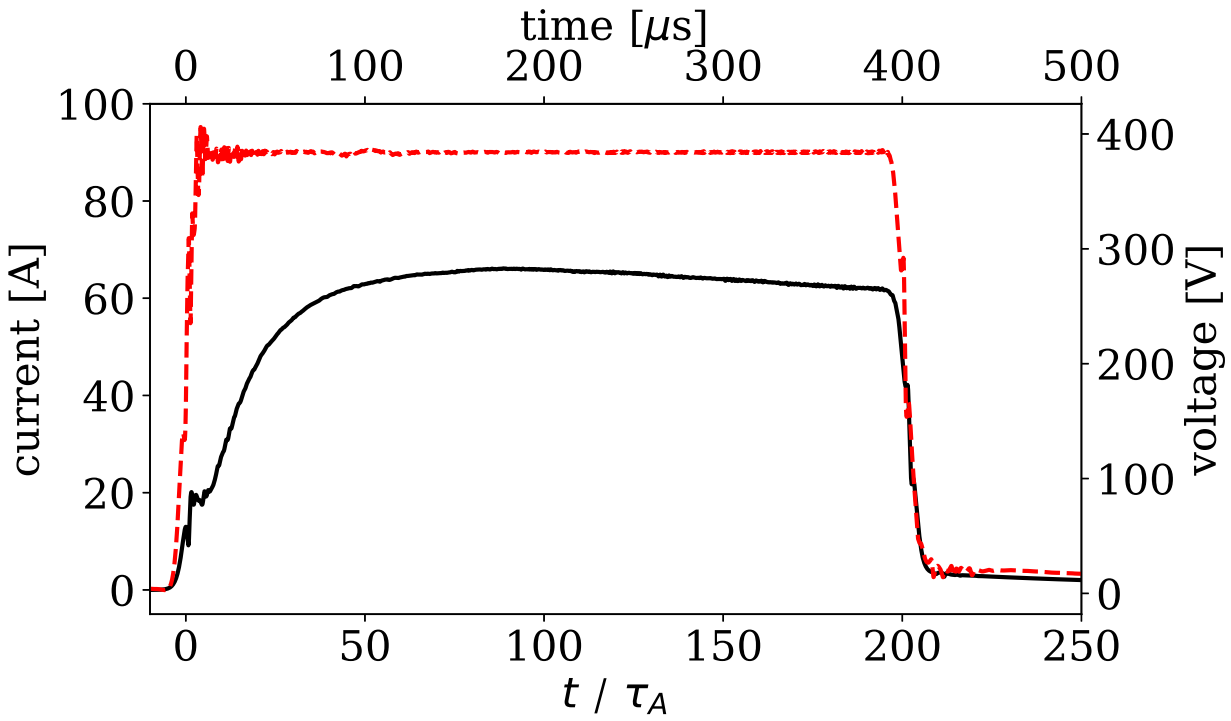

Figure 3.3: The discharge current (solid black line) and the discharge voltage (dashed red line) time traces of the arched plasma source in the presence of a 15 Gauss ambient magnetic field. Each trace is an average of 16 shots. The guiding magnetic field was oriented parallel to the arched plasma current. Similar trends in the discharge current evolution are observed in other magnetic configurations. During the first 100 μs of the discharge, the current gradually builds up, and the arched plasma evolves. A relatively stable phase with a persistent appearance of the plasma is observed after 100 μs.

plasma can be explained by highlighting the importance of Lorentz force associated with the arched plasma current (I_t) and the ambient (overlying) magnetic field (B_a). In the solar atmosphere, this force appears due to the interaction of a large-scale strapping field with the electrical current of prominence or filament [102, 103, 104] (see figure 3.1b). Relative directions of the overlying (or strapping) magnetic field and the arched plasma (or prominence) current dictate the direction of this Lorentz force. On the Sun, in most cases, this force is in the inward direction, and it assists in inhibiting the prominence eruption. Therefore, the Lorentz force due to the overlying magnetic is arranged to be in the inward direction in these experiments. In addition to altering the balance of magnetic forces, an overlying magnetic field introduces magnetic shear at the arched plasma's leading edge, significantly affecting its evolution and morphology. Formation of the S-shaped structure in figure 3.4c is a direct result of the development of strong magnetic shear in the arched plasma.

3.3.2 Detailed Study with a Magnetic Field Probe

Images of the arched plasma are useful in identifying global structures and key stages of plasma dynamics. However, fine-scale internal structures can be better captured in high-resolution three-dimensional (3D) magnetic field measurements. Therefore, the analysis of images is complemented by tracking 3D magnetic field and current-density structures of the arched plasma for six different magnetic-field configurations. The results for overlying magnetic-field B_a = 0, 7.5, 15, 30 Gauss with guiding magnetic-field nearly parallel to the initial arched plasma current are presented in figures 3.5 and 3.6. Following that, figure 3.7 presents measurements for overlying magnetic field B_a = 15, 30 Gauss with a guiding magnetic field nearly antiparallel to the initial arched plasma current. The case of $B_a = 0$ Gauss is reported to serve as a baseline. The streamlines of plasma current density and total magnetic field, in figures 3.5-3.7, are computed by processing volumetric data ($\Delta x = 50$ cm, $\Delta y = 40$ cm, $\Delta z = 40$ cm) from a three-axis magnetic-loop probe. The temporal evolution was recorded with respect to the time when the arched plasma source was turned on at $t = 0$ μs. Typical Alfvén transit and resistive diffusion times are 2 μs and 500 μs,

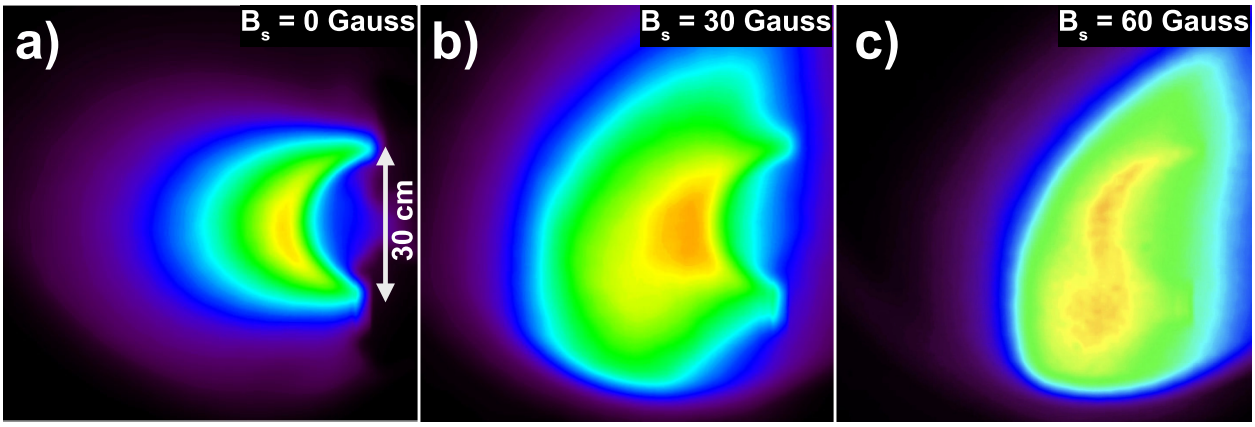

Figure 3.4: Unfiltered camera images of the arched plasma taken along the z-axis present the side-view perspective in figure 3.2. The red and yellow colors signify a higher plasma density, whereas blue and purple represent the arched plasma's lower-density edge region. Panels (a), (b), and (c) correspond to overlying background magnetic fields of 0, 30, and 60 Gauss, respectively, along the positive z-axis (into the page). Each frame was taken at 300 μs after discharge. These panels represent the final stages of the arched plasma evolution. The earlier stages of the evolution are better captured in 3D magnetic-field data (presented in figure 3.6). Deformation of the arched structure and formation of a sigmoid shape is observed at higher ambient magnetic fields in panels (b) and (c).

respectively. Therefore, changes in the morphology of the arched plasma were minimal after the time indicated in the right-most panels for all magnetic configurations in figures 3.6 and 3.7.

Relative magnitudes of three major forces govern the dynamics of an arched magnetized plasma in the laboratory and on the Sun. We reasonably assume a half-torus shape of the arched plasma, which is subjected to the guiding and ambient magnetic fields (see figure 3.1b). With that, the major forces are the tension force F_t, the hoop force F_h, and the strapping force F_s [24]. A detailed discussion on these forces can be found in section 1.3 of this dissertation. For a typical solar prominence, relative magnitudes of hoop, tension, and strapping forces are 1.0, 0.3, and 0.7, respectively [24]. The magnetic field configurations were chosen strategically for this experiment to keep it relevant to the solar case. Therefore, it was important to keep the arched plasma current well below the current threshold for kink instability.

In the case of B_a = 0 Gauss, an outward expansion of the arch was dominated by the hoop force in the absence of an overlying magnetic field and associated Lorentz force (results presented in figure 3.5). The twist of the arched plasma for this configuration was observed to be minimal, as expected ($\Phi_{max} \approx 0.05\pi$). The arched plasma was, therefore, kink-stable ($\Phi < \Phi_c$). Interestingly, the arched plasma current does not closely follow the magnetic field. In the absence of an overlying magnetic field, this magnetic configuration serves as a baseline to which we compare all other magnetic field configurations.

In the following three magnetic configurations, the inward Lorentz force (strapping force) was applied using an overlying magnetic field (B_a = 7.5, 15, 30 Gauss, results presented in figure 3.6), while the guiding magnetic field was oriented nearly parallel to the arched plasma current. The overlying magnetic field naturally introduces magnetic shear in the arched plasma. The initial magnitude of the magnetic shear can be enhanced by the application of a stronger ambient magnetic field, and its sign can be reversed by reversing the direction of the guiding magnetic field. The magnitude of magnetic shear has a direct impact on the arched plasma evolution. Notably, the sigmoid shape (reverse-S) is prominent at stronger overlying magnetic fields. An increase in the magnitude of B_a enhances the strapping force and reduces the major radius of the arched

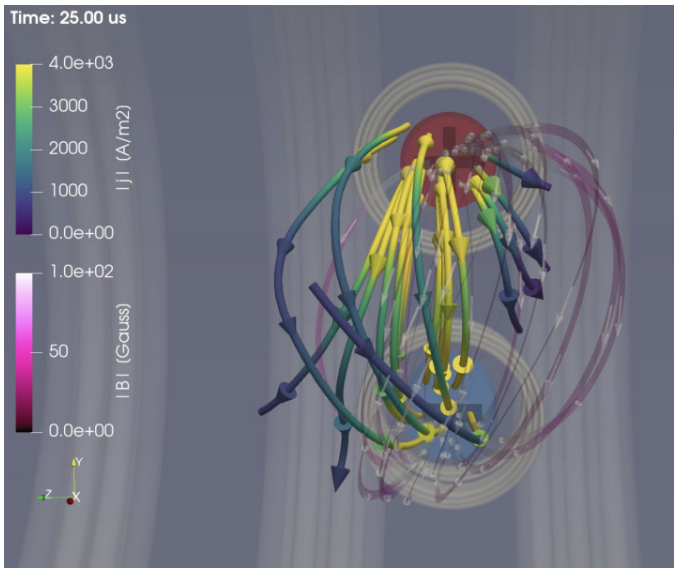

Figure 3.5: Streamlines of the electrical current density of an arched plasma measured at 25 μs (12.5 τ_A since the birth of the arched plasma). The overlying magnetic field was turned off in this case. Therefore, Lorentz force associated with the overlying magnetic field is absent. The solid streamlines (with arrowheads outside the tubes) represent plasma current density, whereas transparent ribbons (with internal arrowheads) represent the total magnetic field (including the vacuum magnetic field). Cathode and anode foot-points are marked by "-" and "+" signs, respectively. Electromagnetic coils are rendered in a transparent light-gray color. The color scales associated with the streamlines of the magnetic field and current density are indicated on the left. It is evident that the arched plasma current does not closely follow the vacuum magnetic field lines, even in the absence of the overlying magnetic field.

plasma. For three different overlying magnetic fields, B_a = 7.5, 15, and 30 Gauss, we estimated the magnetic field twist $\Phi_{max} \approx 0.22\pi, 0.35\pi,$ and 0.73π, respectively. This confirms that the arched plasma is not kink-unstable. Results in figure 3.6 suggest that even a kink-stable arched plasma produces a complex magnetic topology in the presence of a strong overlying magnetic field.

Finally, two magnetic configurations associated with antiparallel arched plasma current and guiding magnetic field were explored at B_a = 15, 30 Gauss. Streamlines of magnetic field and electrical current density for both cases are depicted in figure 3.7. As expected, the sign of the magnetic shear is reversed in these cases when compared to the parallel guiding magnetic field cases presented in figure 3.6. The evolution of the magnetic topology of the arched plasma also differs. The sigmoid shape is again more prominent at stronger magnitudes of the overlying magnetic field. However, the arched plasma takes a forward-S shape in this case (as opposed to the reverse-S shape in figure 3.6). For both cases, the arched plasma current is well below the current threshold for kink instability. The magnetic field twist is estimated using 3D magnetic field data. The maximum twist of the arched plasma is 0.22π and 0.54π for B_a = 15 and 30 Gauss, respectively. The trend of increase in Φ at stronger ambient magnetic fields is also observed in imaging data (see section 3.3.3). As we discussed earlier in section 3.1, the forward-S and reverse-S plasma structures are usually observed in the different hemispheres of the Sun. A close association between sigmoid formation and solar eruption has been established in remote observations [105]. The underlying cause for the formation of forward- and reverse-S-shaped sigmoids on the Sun is still unresolved [106]. Our experiments cannot rule out the correlation between kink instability and the shape of the sigmoid. However, our results confirm that kink instability is not a necessary requirement for the formation of sigmoids on the Sun. In addition, the relative directions of the overlying and guiding magnetic fields play essential roles in controlling the sign of sigmoid.

3.3.3 Quantifying Shear Angle with Filtered Imaging Data

To complement the magnetic field measurements, we recorded filtered images of the arched plasma to capture the dynamics of singly ionized helium (468 nm narrow band-pass filter). These images

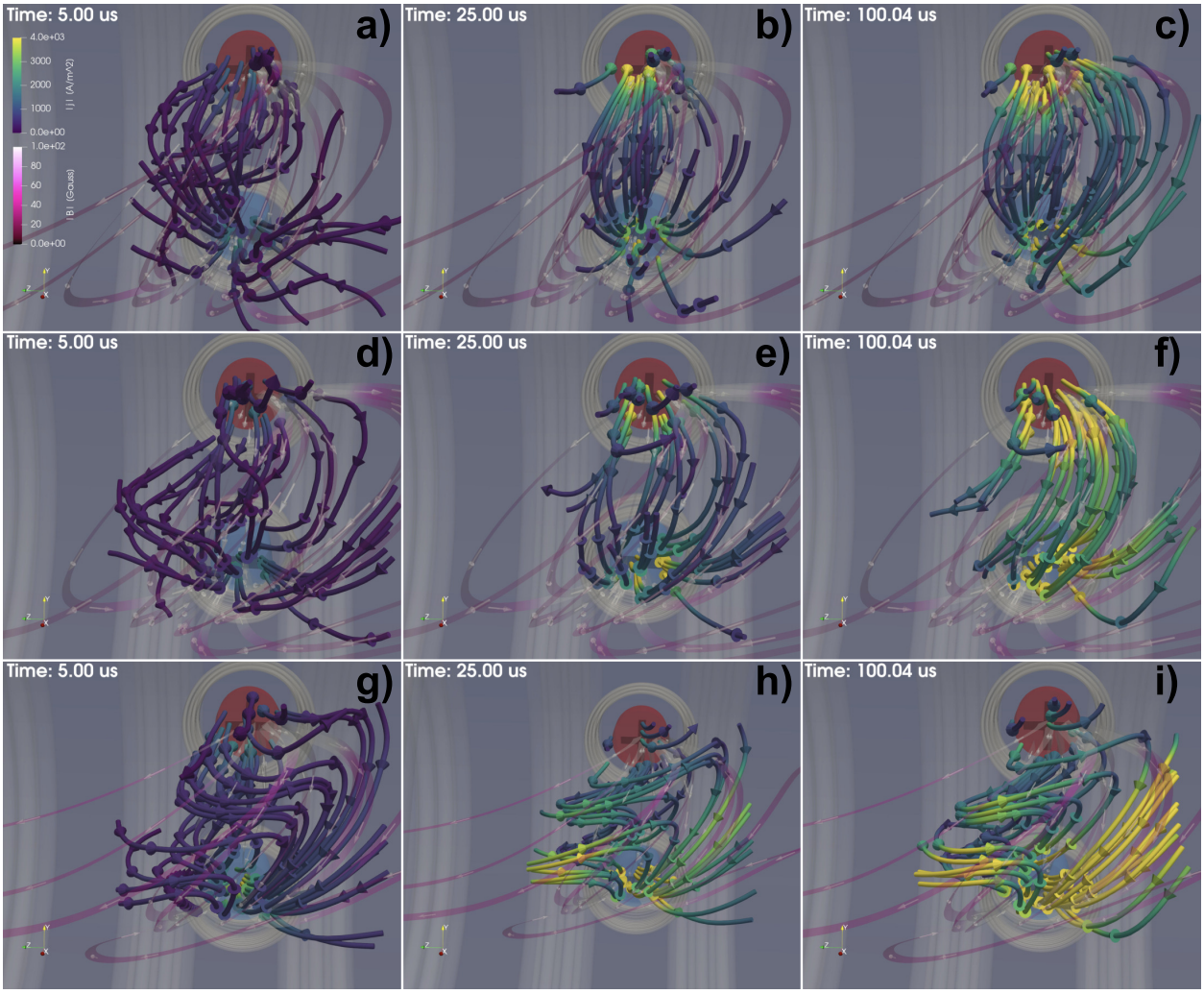

Figure 3.6: The temporal evolution of the arched plasma is captured by displaying the streamlines of current density and magnetic field at 5 μs, 25 μs, and 100 μs (τ_A = 2 μs) for three different ambient magnetic fields: 7.5 G [panels a-c], 15 G [panels d-f], and 30 G [panels g-i]. The guiding magnetic field was set parallel to the electric current of the arched plasma. The solid streamlines (with arrowheads outside tubes) represent plasma current density, whereas transparent ribbons (with internal arrowheads) represent the total magnetic field. Cathode and anode foot-points are marked by "-" and "+" signs, respectively. Electromagnetic coils are rendered in a transparent light-gray color. All panels share the same color scale, displayed on the left of the panel (a).

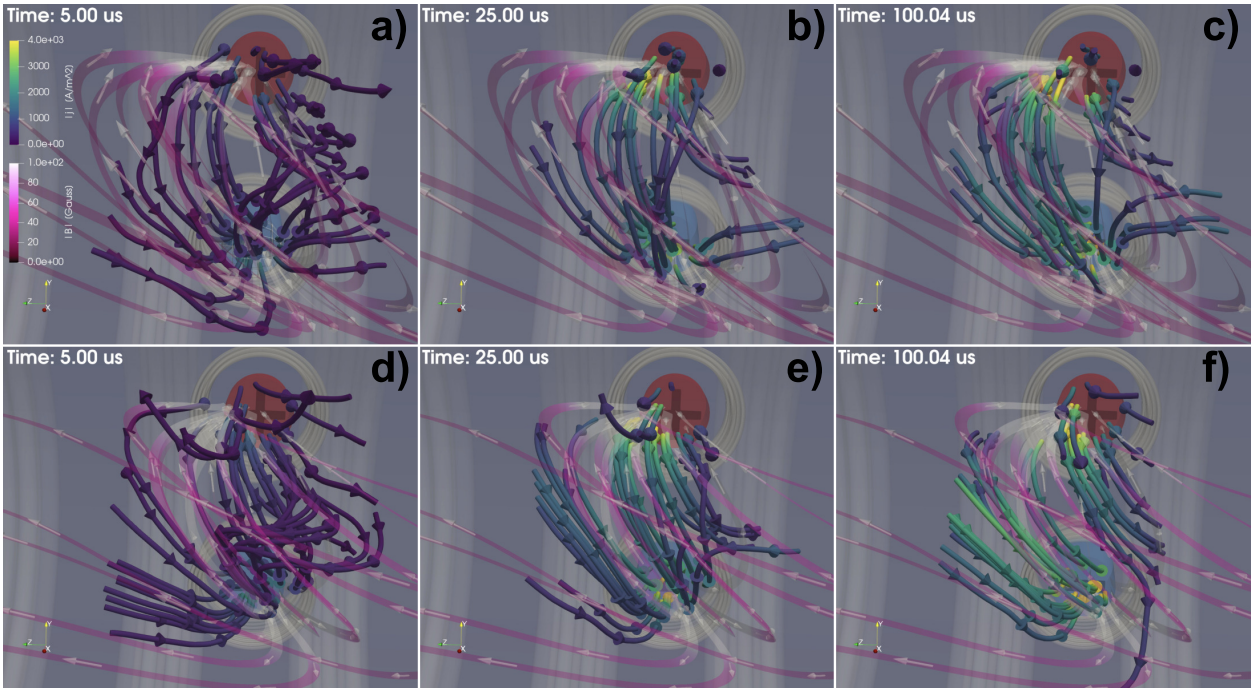

Figure 3.7: The temporal evolution of the arched plasma is captured by displaying the streamlines of current density and magnetic field at 5 μs, 25 μs, and 100 μs (τ_A = 2 μs) for two different ambient magnetic fields: 15 G [panels a-c], and 30 G [panels d-f]. The guiding magnetic field and the electric current of the arched plasma are nearly antiparallel to each other in the beginning. The solid streamlines (with arrowheads outside tubes) represent plasma current density, whereas transparent ribbons (with internal arrowheads) represent the total magnetic field (including the vacuum magnetic field). Cathode and anode foot-points are marked by "-" and "+" signs, respectively. Electromagnetic coils are rendered in a transparent light-gray color. All panels share the same color scale, displayed on the left of the panel (a).

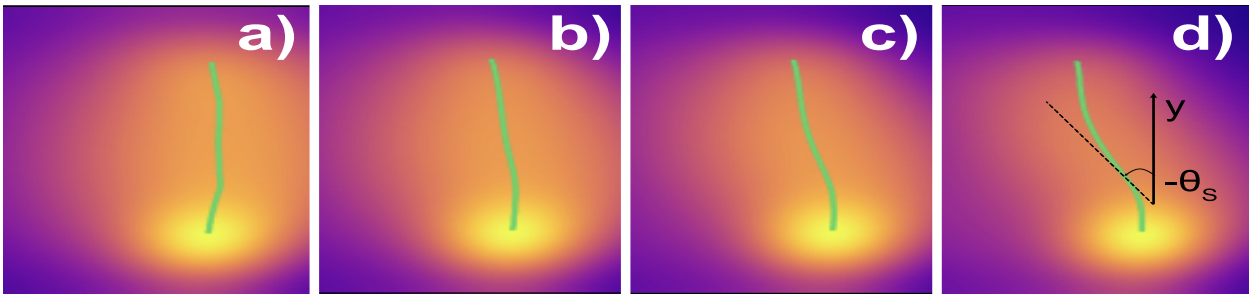

Figure 3.8: Fast camera images of singly ionized helium in the arched plasma (top-front view as indicated in figure 3.2, 468 nm narrow pass band filtered) recorded at 125 μs after the discharge ($\approx$62.5 τ_A) for (a) 0 G, (b) 7.5 G, (c) 15 G, and (d) 30 G overlying magnetic field configurations. The guiding magnetic field and the electrical current of the arched plasma are nearly antiparallel to each other in the beginning. The symmetry axis of the arched plasma in each frame is highlighted by the solid green line, representing the peak intensity of He^+ emission. The magnetic shear of the arched plasma at the apex increases with the strength of the overlying magnetic field. The sheared configuration produces an arched plasma with a sigmoid (forward-S) shape that becomes more pronounced at higher magnitudes of the overlying magnetic field (see panels c and d). This trend is also observed when the guiding magnetic field and the arched plasma current are nearly parallel to each other in the beginning, except for the reverse-S shape of the arched plasma. The angle θ_S defined in the text is indicated in panel (d).

were collected from the top-front view (the camera positioned at x = 65 cm, y = 20 cm, z = 0 cm as indicated in figure 3.2) for B_a = 0, 7.5, 15, and 30 Gauss. Each case was investigated with the guiding field oriented nearly parallel and then nearly antiparallel to the initial arched plasma current. These images were processed to identify the symmetry axis of the arched plasma. The maximum He-I emission intensity along the horizontal direction was assumed to occur on the symmetry axis. The identification of the symmetry axis is helpful in tracking the morphological evolution of the arched plasma. A selection of processed images is presented in figure 3.8 for the antiparallel orientation of the guiding magnetic field with respect to the arched plasma current.

Our analysis of the imaging data agrees well with estimates of twist from 3D magnetic-field

data (depicted in figures 3.5-3.7). The sigmoid shape is observed to be more pronounced at larger magnitudes of the overlying magnetic field, and its sign changes with the reversal of the guiding magnetic field. For guiding magnetic field oriented nearly parallel to the initial arched plasma current, a reverse-S-shaped arched plasma is produced. Reversal of the guiding magnetic field (antiparallel to the arched plasma current) forms a forward-S-shaped arched plasma. Selected images for all four cases of the ambient magnetic field with guiding magnetic field in the antiparallel orientation are presented in figure 3.8. These panels represent the final stages of the arched plasma evolution ($\tau_A << t$ = 125 μs $< \tau_R$). The solid-green line in these panels highlights the symmetry axis of the arched plasma, where peak emission of He^+ occurs in the horizontal direction. The overlying magnetic field significantly impacts the morphology of the arched plasma. The sigmoid shape of the arched plasma is visible at a stronger overlying magnetic field, as evident in figure 3.8d.

The temporal evolution of the sigmoid and associated twist are analyzed by acquiring multiple frames of He^+ plasma during 40–200 μs. The temporal resolution of these frames was 5 μs. At each time step, the symmetry axis was computed and marked (as in panels of figure 3.8). The angle θ_S quantifies the angle between the vertical axis (connects both foot points) and the symmetry axis at the leading edge of the arched plasma (marked in figure 3.8d). The forward-S shape of the arched plasma is characterized by a negative θ_S, while the reverse-S shape has a positive θ_S. The time evolution of θ_S for parallel and antiparallel guiding magnetic field (with respect to the arched plasma current) is presented in figure 3.9. The early stages of the arched plasma evolution (0-40 μs) are excluded from this analysis due to difficulty in accurately identifying the symmetry axis. This was mainly due to the lower intensity of He^+ emission in the beginning. These results are consistent with 3D magnetic-field measurements on the observation of strong magnetic shear and sigmoid formation at stronger overlying magnetic fields. Moreover, the reversal of the sign of sigmoid with a guiding magnetic field is also confirmed.

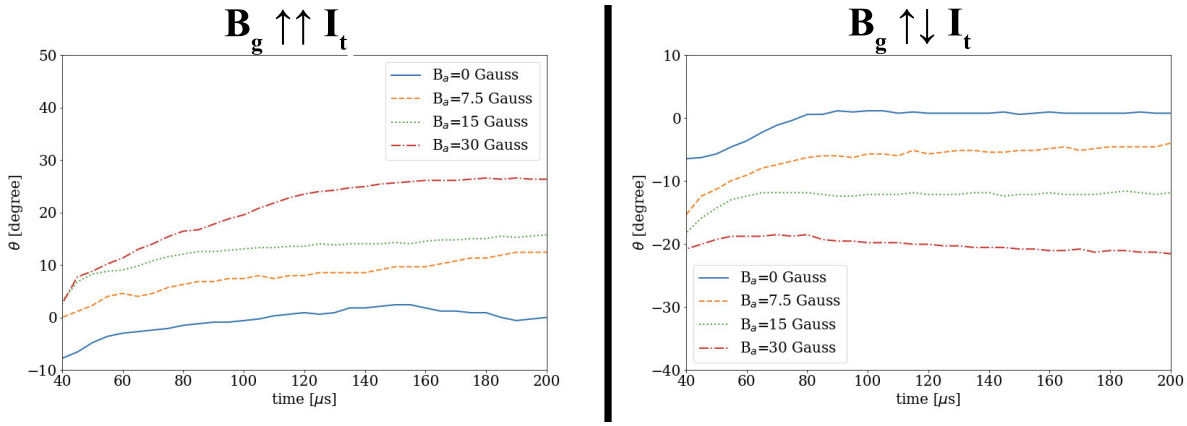

Figure 3.9: Temporal evolution of the shear angle θ_S (as indicated in figure 3.8d) at four different overlying magnetic fields (0, 7.5, 15, and 30 Gauss) are displayed in these panels. On the left panel (a), the guiding magnetic field is oriented nearly parallel to the initial arched plasma current. The right panel (b) corresponds to the guiding magnetic field, nearly antiparallel to the initial arched plasma current. These panels display results during the later stages of the temporal evolution, mainly because the angle θ_S could not be measured reliably in the beginning due to the extremely dynamic nature of the arched plasma. There is a noticeable trend of increase in $|\theta_S|$ with an overlying magnetic field for both guiding field configurations. The negative angle θ_S in the antiparallel guiding magnetic field configuration is associated with a forward-S shape, while the positive angle θ_S (parallel case) corresponds to the reverse-S shape of the arched plasma.

3.3.4 Final Comment on a Force-free State

Our results indicate that the arched plasma is not in a force-free state (characterized by the parallel magnetic field and electrical current). There are numerous examples of the force-free state of a low β plasma - especially in the solar corona. The concept of force-free magnetic fields has been widely used to model the coronal magnetic field structures [18]. Although this simplified description is often useful in explaining the large-scale topological evolution of the magnetic fields, it is not always supported by observations - especially during eruptions and in the active region on the Sun [20, 107]. The observation of a non-force-free state in this laboratory experiment and active region on the Sun should not be unexpected since the basic assumptions for the existence of a force-free state (ignorable pressure gradients, plasma flows, and Hall-term) are not supported by observations. Another example of non-parallel current and magnetic fields are pressure-gradient driven diamagnetic currents in a low-β magnetized plasma. In our future research, we will attempt to identify the exact cause of the existence of a non-force-free state in our experiment. This chapter's main focus is highlighting the development of sigmoid shapes in a kink-stable arched plasma. Our initial analysis suggests eruptive behavior of the arched plasma and formation of large-scale flux-rope structures when sufficiently large magnetic shear is developed in the arched plasma ($t = 75 - 200$ μs). These large-scale flux-ropes are not captured in figures 3.6 - 3.8 and will be discussed in chapter 4.

3.4 Summary

The effect of a nearly horizontal overlying magnetic field on the evolution of an arched magnetized plasma has been studied in this laboratory plasma experiment. The experiment was designed to capture the dynamics of arched plasma eruptions on the Sun. The electrical current in the arched magnetized plasma was kept below 200 A to ensure that relative magnitudes of the hoop, tension, and strapping forces for solar filaments and prominences are comparable with the experiment. The lower magnitude of electrical current ensures that the arched plasma does not form multiple

poloidal magnetic-field twists from one foot-point to the other during the pre-eruption phase (as observed on the Sun). Experimental results confirm that sigmoid plasma structures are naturally produced in a sheared magnetic configuration – even in the absence of kink instability. The shear angle critically depends on the magnitude of the overlying magnetic field and the direction of the guiding magnetic field. This suggests that the apparent writhe of a current-carrying arched plasma has a strong dependence on the structure of the overlying magnetic field, not just on the magnitude of the electrical current.

CHAPTER 4

Dynamic Formation of a Transient Jet from Arched Magnetized Laboratory Plasma

This chapter explores the eruptive behavior of arched magnetized plasmas with dimensionless parameters relevant to the Sun's photosphere ($\beta \approx 10^{-3}$, Lundquist number $\approx 10^4$, plasma radius/ion gyroradius ≈ 20, ion-neutral collision frequency $\gg$ ion cyclotron frequency). Dynamic formation of a transient plasma jet was observed in the presence of the strapping magnetic field. The eruption leading to the jet is nonintuitive since the arched plasma is both kink- and torus-stable. The jet structure erupts within a few Alfvén transit-times from the formation of the arched plasma. Extensive measurements of plasma temperature, density, magnetic field, and flows are presented. In its early stages, the jet plasma flows away from the arch at supersonic speeds (Mach 1.5). This high-speed flow persists up to the resistive diffusion time in the arched plasma and is driven by large gradients in the magnetic and thermal pressures near the birthplace of jets. There are two distinct electric current channels within the jet, one consisting of outgoing electrons and another composed of electrons returning to the anode footpoint. Significant current density around the jet results from the diamagnetic current produced by a large thermal pressure gradient in the jet. Ion-neutral charge-exchange collisions provide an efficient mechanism to produce the cross-field current and control the dynamics of the complex current channels of the jet.

4.1 Introduction

4.1.1 Background and Motivation

The solar atmosphere is an incredibly dynamic environment, filled with a myriad of diverse structures. Solar prominences, jets, and spicules are just some examples. Arched plasma structures on the Sun (coronal loops, prominences) are abundant in both upper and lower solar atmospheres. They sporadically erupt, forming jet-like structures (coronal jets, chromospheric anemone jets) or eject massive amounts of particles and energy (e.g., coronal mass ejections, flares) [46, 1, 108, 2]. Such eruptive events are thought to be triggered by the loss of stability in the arch (kink and/or torus instability) or reconnection between the emerging flux and the pre-existing magnetic field [32, 33, 34, 35].

Compared to the solar corona (upper solar atmosphere), the lower solar atmosphere (photosphere and lower chromosphere) has a lower temperature, and lower ionization level [4, 3]. The relatively high neutral density ($n_n/n_i \approx 10^3$) and, thus, high ion-neutral collision rates play an important role in the dynamics of photospheric and chromospheric structures. Phenomena like the non-ideal Hall effect and ambipolar diffusion must be considered (more discussion in section 1.5). The latter, in the astronomical definition, is a decoupling between neutral and charged components, leading to diffusion of magnetic field via ion-neutral collisions [3]. The abundance of neutrals in the lower solar atmosphere has been shown to impact the propagation of MHD waves [81], excitation of Alfvén waves, and rate of magnetic reconnection [4], as well as dissipation of electric currents [82]. In solar prominences, ion-neutral collisions generate a frictional force in the direction opposite to gravity, which helps support their structure [83].

4.1.2 In This Chapter

We present the results from laboratory studies of arched magnetized current-carrying plasmas in the presence of a nearly uniform strapping field [48]. The plasma parameters and experimental

conditions were tuned so that the plasma under study remains relevant to similar structures in the lower solar atmosphere. The strapping magnetic field is oriented perpendicular to the plane of the arched plasma and along the axis of the machine, as described in the section below. This field corresponds to the large-scale external magnetic field that straps and inhibits the eruption of solar prominences [24, 109]. The dimensionless plasma parameters in the experiment are arranged to be as close to the solar parameters as possible (see tables 3.1 and 4.1). Relatively low discharge current ($I < 150$ Amperes) in the experiment ensures that the arch remains kink-stable [76, 19, 72]. The strapping-magnetic field is nearly uniform. Therefore the decay index is nearly zero, and the torus instability is absent in this experiment. The decay index measures how fast the strapping magnetic field decays in magnitude along the major radius of the arched plasma (usually modeled as a half-torus). In mathematical form, the decay index is expressed as $n = -d\ln(B_S)/d\ln(R)$, where B_S is the strapping magnetic field, and R is the major radius [78]. The torus instability occurs when the strapping magnetic field (and thus inward $J \times B$ force) decays faster than the hoop force pushing the arched plasma outwards. The critical value for a line-tied arched plasma has been determined to be $n_{crit} = 1.5$ [77]. A relatively high neutral pressure in the experiment ($n_n/n_i \approx 10^2$) makes it relevant to the conditions found in the solar photosphere and lower chromosphere, as discussed above. This experiment allows for *in situ* measurements of plasma parameters (i.e., density, temperature, plasma flows, magnetic field) resolved in time and space.

The formation of a transient jet-like structure perpendicular to the plane of the arched plasma was observed and is reported here. The jet forms in the presence of a strong strapping magnetic field. The early eruption leading to the jet is triggered by the build-up of magnetic shear in the arch, as well as the interaction between emerging flux and the pre-existing strapping field (arched plasma is kink- and torus-stable). The ion flow in the jet was measured to be supersonic and on the order of the Alfvén speed in early stages (Mach 1.5), which is relevant to solar structures like anemone-jets [2] and spicules [41]. The laboratory jet also carries an electrical current with a complex 3D magnetic structure, as discussed in the following sections. Extensive measurements of electron temperature and plasma density were used to produce thermal-pressure profiles of the

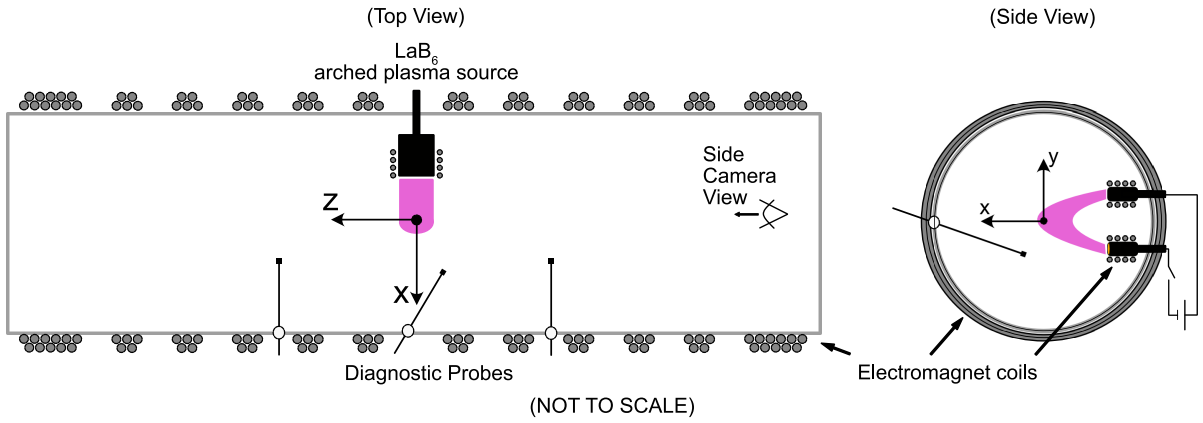

Figure 4.1: Schematic of the experimental setup, depicting cross-sections of the vacuum chamber from the top (left panel) and side (right panel) views. The coordinate system used throughout this work and its origin is indicated on both panels. The origin is located on the axis of the chamber, in front of the arched plasma source, as indicated in both panels. The arched plasma is shown in a dark-pink color in both views. The combination of magnetic fields, generated by larger electromagnets outside the chamber and smaller electromagnets around footpoints of the arched plasma, provides flexibility in simulating a variety of magnetic configurations.

plasma in the arch and the jet (presented below). This research is relevant to the jets, and spicules found in the lower solar atmosphere [41, 2], as well as solar eruptions resulting from emerging flux interacting with pre-existing magnetic field [33, 35].

4.2 Experimental Setup

4.2.1 Overview

This experiment was built to facilitate laboratory studies of current-carrying arched magnetized plasmas relevant to those on the Sun. The electrical current is driven between two electrodes along an arched vacuum magnetic field (see figure 4.1). The arched plasma foot-points are anchored at electrodes, imposing a line-tied boundary condition. The experiment is performed in a cylindri-

cal vacuum chamber (5.0 m long, 1.0 m diameter) filled with neutral helium gas (pressure: 5 – 9 mtorr). The electromagnets placed around the vacuum chamber produce a nearly uniform axial magnetic field (typically set to 30 Gauss, but can be as high as 300 Gauss). This magnetic field serves as a strapping field for the arched plasma, introduces shear to the vacuum field, and impacts the eruption dynamics. The guiding magnetic field (900 G at foot-points) is produced using two smaller electromagnets encompassing the electrodes (see the side-view in figure 4.1). The magnitude of the overlying magnetic is intentionally kept below 60 Gauss. Stronger field results in the open guiding magnetic field-line geometry, which impedes the arched plasma formation. Moreover, an excessively strong strapping magnetic field would result in a strapping force that overwhelms all other forces acting on the arch [110], i.e., not a solar-relevant scenario. The arched plasma (pulse-width = 0.2-0.8 ms) is produced using a lanthanum hexaboride (LaB_6) hot-cathode source. The anode is a 15 cm diameter copper disk while the cathode is a 7.6 cm diameter indirectly heated LaB_6 disk (temperature $\approx$ 1900°C). At this temperature, the cathode becomes efficient in the thermionic emission of electrons [91]. An electric discharge is created between this emissive cathode and the anode above it with a repetition of 0.5 Hz (see figure 4.1). The arched plasma is produced through the ionization of neutral helium gas by primary electrons accelerated from the cathode during the discharge pulse (≈400 V). Typically, this arched helium plasma carries about 120 A of current and has $n_e = 5 \times 10^{13}$ cm^{-3}, $T_e = 13$ eV, $T_i = 0.1$ eV, Alfvén transit time $\tau_A = 2\ \mu$s, and resistive diffusion time $\tau_R = 500\ \mu$s. The capacitor bank used to supply the current is charged by a floating power supply. The electrode pair is mounted on a large side port in the middle of the chamber. The separation between the foot points of the arched plasma can be varied in the range of 10 - 41 cm. Both electrodes reside in the $z = 0$ symmetry plane, at $x = -28$ cm and $y = \pm$ 10 cm (coordinate system depicted in figure 4.1). Typical dimensionless parameters of the arched plasma and a quiescent solar prominence are presented in table 3.1 of chapter 3. The relevant plasma parameters of jet-like structures found in the lower solar atmosphere and the laboratory jet erupted from arched plasma are compared in table 4.1.

	Lower solar atmosphere	Laboratory jet
Plasma β	≈ 1 *	0.8
v_{ion}/v_A	≈ 1 †*	≈ 1
n_i/n_n	10^{-3} – 10^{-4} *	2×10^{-2}
ν_{in}	10^{5} – 10^{8} *	5.4×10^{5}
ν_{ei}	10^{7} – 10^{8} *	1.4×10^{6}
Ω_i/ν_i	10^{-1} – 10^{-4}*,**	2.1×10^{-2}
D_{jet}/r_i	10^{7} – 10^{8} *	≈ 10
length/width (jets)	≈ 10 *	≈ 10

Table 4.1: Comparison of the relevant plasma parameters of typical solar structures (anemone jets, spicules) found in the lower solar atmosphere (photosphere and lower chromosphere) and the jet-like structure erupted from laboratory arched plasma. Here v_{ion}, v_A are ion flow velocity and Alfvén velocity, ν_{in}, ν_{ei}, ν_i are ion-neutral, electron-ion and overall-ion collision frequencies, while Ω_{ci} is the ion cyclotron frequency. The n_i and n_n are ion and neutrals number densities, respectively. The diameter of the jet and the ion gyroradius are D_{jet} and r_i, respectively. *[2] †[41] **[86]

4.2.2 Diagnostics

Diagnostic *in-situ* probes (three-axis magnetic, dual and triple tip langmuir, Mach) are mounted on a computer-controlled 3D probe drive system. A more comprehensive discussion on probes and the probe drive can be found in sections 2.2 and 2.3, respectively. The data is collected at a given location multiple times (for signal-to-noise considerations) before the system moves the probe to the next location. The high reproducibility of this experiment allows for the reconstruction of measured parameters in 3D space. A multichannel 100 MHz digitizer is used to record the data in high temporal resolution. The diagnostic probes are built using high-temperature ceramic coated wires and other components that can withstand up to 750°C temperature near the cathode footpoint of the arched plasma. This setup allows for a reliable and efficient measurement of plasma parameters (n, T_e, B) with a good spatiotemporal resolution (spatial resolution $\Delta x = 1.5$ cm, temporal resolution $\Delta t = 4 \times 10^{-8}$ s for the results reported here). A fast intensified CCD camera (5 ns minimum exposure time, 1280 x 1024 resolution, and 12-bit digital converter) is used to record the plasma images for quick on-the-go diagnostics.

4.3 Results and Discussion

The experiments conducted in this work are focused on the diagnostics of the transient jet ejected from the arched plasma. In all experiments, the guiding magnetic field follows the same direction as the electric current in the arched plasma (anode to cathode). Two strapping field cases are investigated, $B_S = 0$ and 30 Gauss in the positive z-direction (resulting in an inward $j \times B$ force on the arch). In the magnetic field configuration of this experiment, ions remain magnetized in the arched plasma and are weakly magnetized away from it. The strapping field introduces a shear to the magnetic field that triggers a dynamic formation of the jet structure towards the negative z-direction along the axis of the machine. This phenomenon takes place during the early stages of the arched plasma evolution ($t < 100$ μs), when the poloidal magnetic flux in the arched plasma gradually builds up, leading to dynamic and eruptive behavior. The side-by-side comparison be-

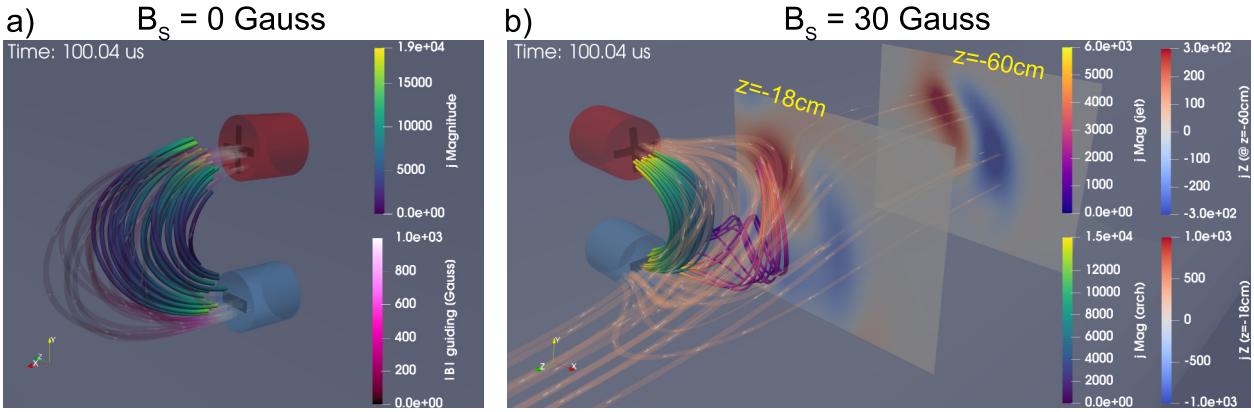

Figure 4.2: Three-dimensional rendering of the current density structure calculated using data from a three-axis b-dot probe (t=100 μs after the discharge onset). On both panels, the tubular streamlines represent current density, with color scale corresponding to its magnitude. Translucent ribbons represent the total magnetic field. Blue and red cylinders represent the cathode and anode footpoints with (-) and (+) marks, respectively. The background magnetic field has been set to 0 and 30 Gauss for panel **(a)** and panel **(b)**, respectively. The two planes in panel (b) display the magnitude of the z-component of current density ($j_{\|}$) at z = -18 cm and z = -60 cm. The presence of a strapping field introduces magnetic shear in the arched plasma, which leads to the ejection of a jet towards the negative z-direction (magenta-orange current density streamlines).

tween two strapping magnetic field configurations is presented in figure 4.2, which renders the magnetic probe data in the form of current density lines. With a strapping field present, a jet-like structure of considerable twist is observed to leave the arch towards the negative z-direction. The z-component current density planes in figure 4.2(b) display an outgoing channel (red, electrons away from the arch) and the return current channel (blue, electrons towards arch). Discussion on the twist and the closure between the two channels follows later in this chapter.

4.3.1 Thermal Pressure Measurements

The jet signatures are also apparent in the Langmuir probe data. A triple tip configuration allows for a temporally resolved measurement of plasma density, $n_e = n_i$ (through quasineutrality),

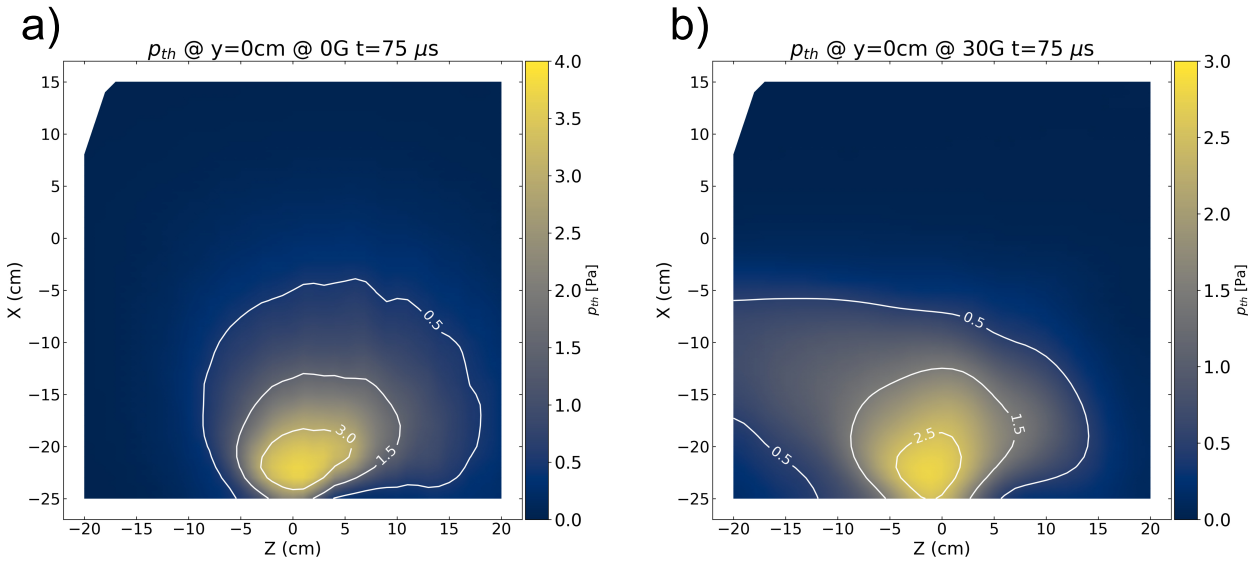

Figure 4.3: Thermal pressure at t = 75 μs after the discharge onset in the XZ plane at y=0 cm (cross-section in the middle of the arched plasma) for **(a)** B_S = 0 Gauss and **(b)** 30 Gauss. The plasma density in the arch was on the order of 2×10^{18} m^{-3}, and the electron temperature was on the order of 10 eV. The white isobars were added to guide the eye. There are clear signatures of thermal pressure associated with the jet towards the negative z-axis in the presence of a strong strapping magnetic field (panel b), indicating an ongoing eruption.

and electron temperature, T_e [96] (see section 2.2). These data were used to calculate the plasma thermal pressure through $p_{th} = n_e k_B T_e$, where k_B is the Boltzmann constant. The ion contribution to the thermal pressure is negligible since the ion temperature $T_i << T_e$. The cross-section planes (middle of the arch) containing plasma thermal pressure are presented in figure 4.3 for both cases of strapping field. There are clear signatures of plasma pressure towards the negative z-direction with a strapping field present. Using plasma density and electron temperature measurements, a transverse profile (XY plane at z = -18 cm) of the jet thermal pressure is presented in figure 4.4(a). A similar structure is also observed in transverse profiles of plasma density and temperature. The comparison of the thermal pressure and total current density profiles [using data presented in figure 4.2(b)] suggests that the high thermal pressure region contains both (forward and return) current channels of the jet. As expected, these characteristic features of the jet are ab-

sent in the case of a zero overlying magnetic field. This confirms that a strong strapping magnetic field is a potential source of driving transient jets due to the development of strong magnetic shear. The magnetic shear is likely to drive magnetic reconnection near the birthplace of jets. However, direct measurements of reconnection were not performed in this experiment.

4.3.2 Plasma Flow in the Jet

A three-axis Mach probe was employed to measure transverse profiles of plasma flow in the jet. The results for an XY plane at z = -18 cm are displayed in figure 4.4(b). In its early stages, the jet reaches supersonic speeds (Mach 1.5 $\pm$ 0.1) towards the negative z-axis. This velocity is also on the order of the Alfvén speed in that region ($v_A \approx 3.3 \times 10^4$ m/s) which resembles jet structures found in the Sun's lower atmosphere [41, 2]. The driving mechanism for this supersonic flow and its time evolution will be discussed later in this section.

4.3.3 Diamagnetic Current as a Result of High Thermal Pressure Gradient

The high thermal pressure gradient between the structure seen in Figure 4.4(a) and the space around it in the transverse plane gives rise to the diamagnetic current [111, 112]. In figure 4.5(a), the thermal pressure in the cross-section of the jet at z = -60 cm is over-plotted with the perpendicular component of current density ($j_\perp$) measured with a bdot probe. Additionally, the thermal pressure gradient and the magnitude of $j_\perp$ along the x-line at y = 3 cm and z = -60 cm are plotted in figure 4.5(b). The structure of thermal pressure correlates very well with the measured $j_\perp$. Moreover, the peaks in the thermal pressure gradient align with the peaks of $|j_\perp|$. This indicates that the diamagnetic current is a significant contributor to the large $j_\perp$ measured around the jet due to the large thermal pressure gradient. The presence of the substantial diamagnetic current explains the high twist in the jet current density streamlines of figure 4.2(b). In collisional plasma, such as in this experiment or the solar photosphere and chromosphere, diamagnetic currents and associated drift modes grow due to electron collisions, especially when transverse thermal pressure gradi-

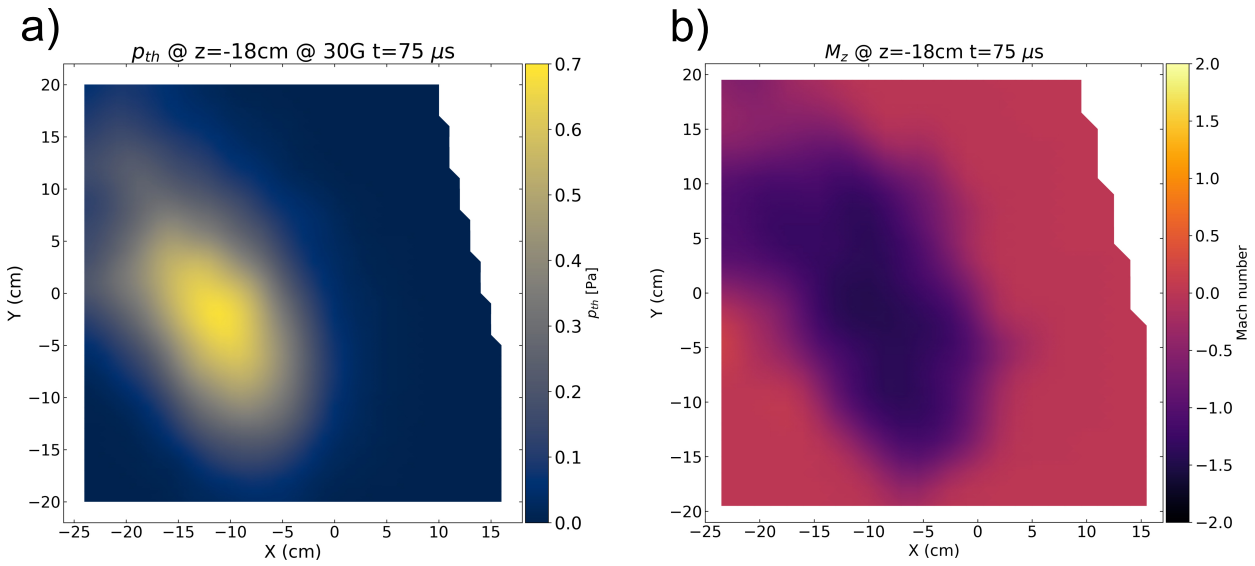

Figure 4.4: The thermal pressure **(a)** and the z-component of ion velocity **(b)** measured at t = 75 μs after the discharge onset in the XY plane at z = -18 cm (cross-section of the erupted flux rope). The magnitude of each corresponds to the respective color bar scale. These results confirm that the higher-thermal-pressure region of the jet propagates with supersonic speeds (Mach $\approx$ 1.5) during the eruption.

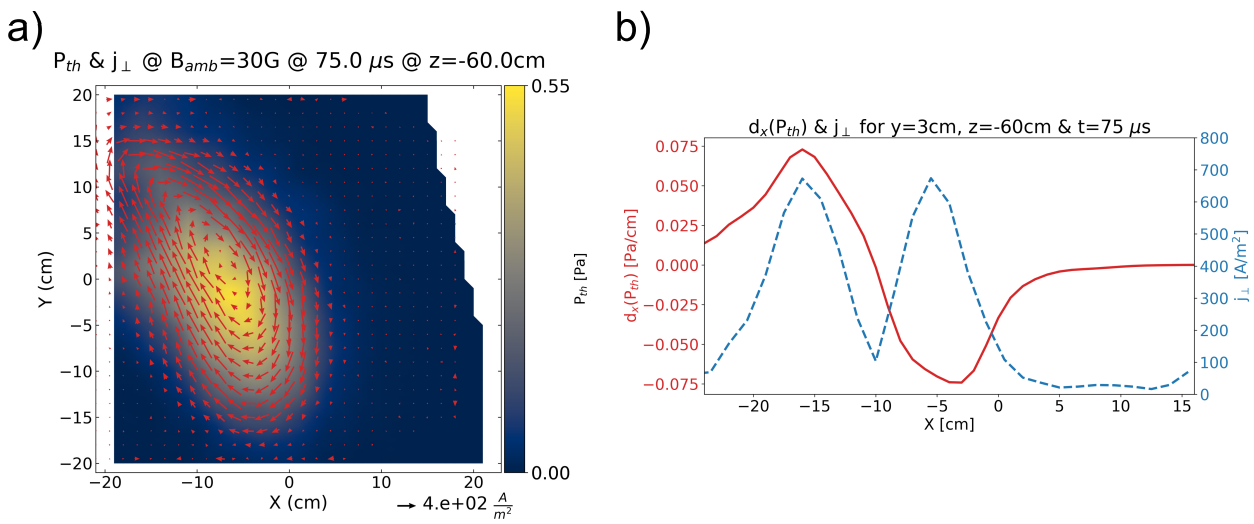

Figure 4.5: **(a)** Thermal pressure over-plotted with current-density vectors (red colored) of the jet at t = 75 μs; **(b)** gradient of the thermal pressure along the x-axis (solid red line) and the magnitude of $j_\perp$ (blue dashed line) at t = 75 μs, y = 3 cm and z = -18 cm. The strong twist in the current density lines of the ejected flux rope seen in Figure 4.2 results from the strong diamagnetic current present due to the large gradient in the thermal pressure.

ents are associated with plasma flows and electrical current directed along the magnetic field lines ([112, 113]).

4.3.4 Temporal Analysis

In order to investigate the temporal evolution of plasma density and electron temperature, the appropriate data were averaged over the center of the structure seen in figure 4.3 (i.e., the center of the arched plasma at its apex) and displayed in figure 4.6 for both cases of strapping magnetic field. The temperature traces evolve similarly in either case of the magnetic field setting. Only in later stages (around resistive diffusive timescales) is there a small dip in temperature trace for $B_S = 30$ Gauss. When it comes to density, there is an enhanced spike in the early stages of arch evolution with a strapping magnetic field present. It is then followed by a significant dip in density compared to the $B_S = 0$ Gauss case. The presence of a strapping magnetic field aids the initial formation of the arch (due to inwards $J \times B$ force). The jet is formed in an eruptive event that expels the high-density plasma confined in the arch and guides it along the elongated structure of the jet. The initial formation spike in plasma density traces is recorded in the center of arched plasma as well as in the center of the jet at z = -18 cm. The spike in the jet is delayed by 5 μs with respect to the arched plasma, as seen in figure 4.7. Factoring in the distance plasma had to travel from the apex of the arch to the center of the jet at that z-location, and the ion sound speed for plasma under study ($2.3 \pm 0.1 \times 10^4$ m/s), this delay corresponds to a Mach 1.5 speed. This is in agreement with the Mach probe measurements presented in figures 4.4(b) and 4.8.

The total outgoing current in the jet, I_{jet}, was obtained by integrating the measured z-current density j_z at z = -18 cm over the area of interest (see figure 4.4a). Similarly, integrating the x-current density j_x over an area parallel to the cathode yields a total current leaving the cathode, I_{cat}, into the arched plasma. The normalized time traces for both total currents, along with the Mach probe measurement of z-velocity in the jet, are presented in figure 4.8. The ratio of $I_{jet}/I_{cat} \approx 0.1$ in this experiment. The evolution of the total current in the jet differs in character when compared to the current injected into the arched plasma. The jet current is developing slower and with the

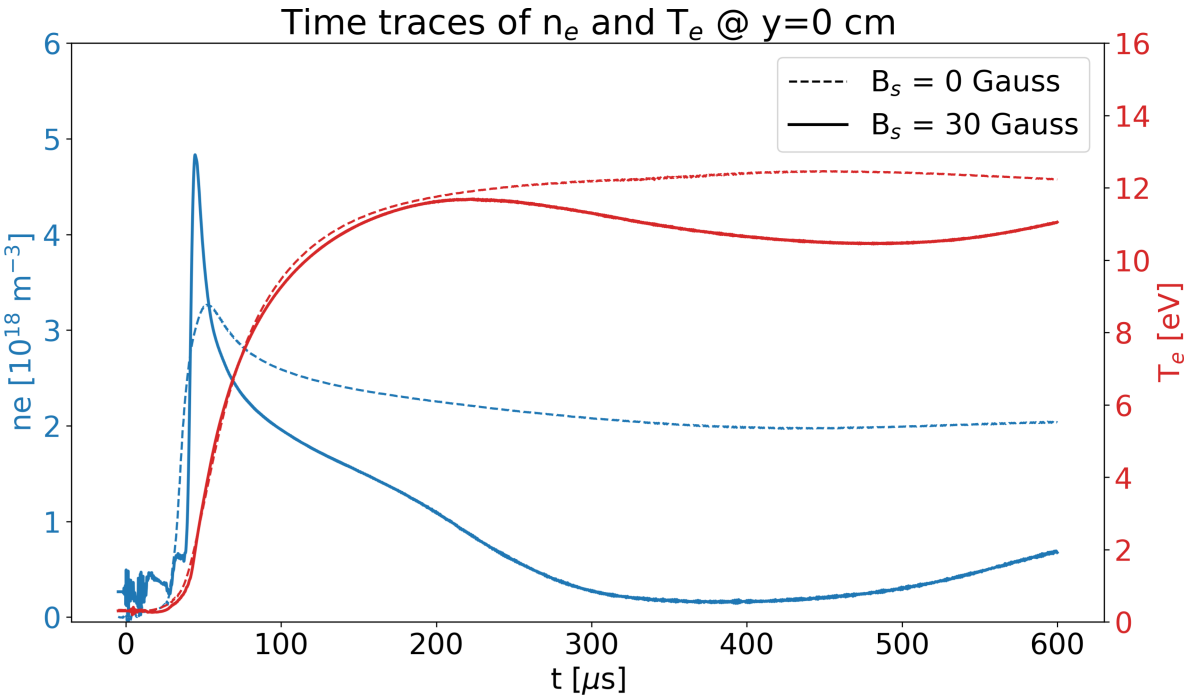

Figure 4.6: Electron density (blue) and temperature (red) at the center area of the arched plasma with strapping magnetic field B_S set to 0 Gauss (dashed) and 30 Gauss (solid). With the magnetic shear present, there is a significant enhancement in the initial density spike followed by depletion in the density and considerate dip in the temperature when compared to B_S = 0 Gauss case. This suggests the early onset of an eruptive event, which diverts the plasma from the main arch to the elongated structure (along the axis of the device shown in figure 4.1) of the jet.

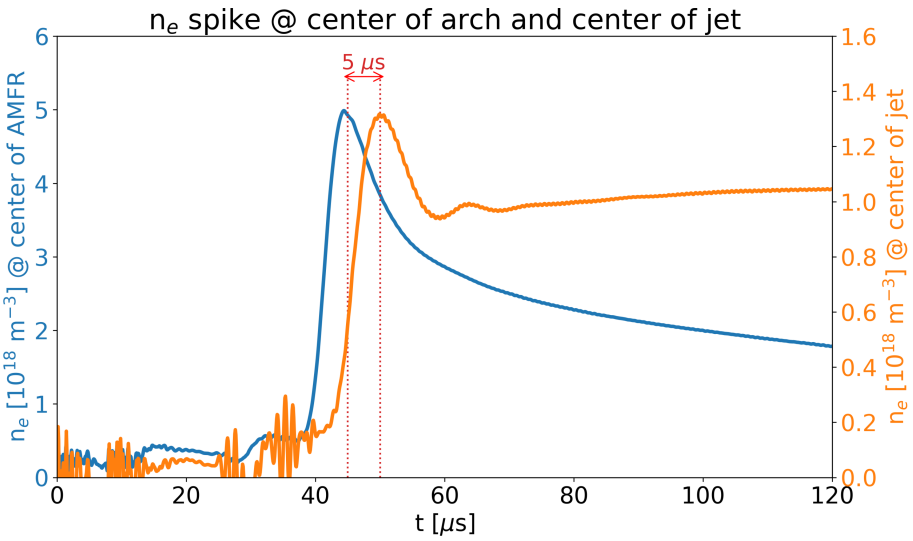

Figure 4.7: Electron density during early stages of arched plasma evolution in the center of arched plasma (blue) and the center of the jet at z = -18 cm (orange). The delay between the onset peaks of those signals is 5 μs. Considering the distance plasma traveled, this delay translates to a speed of $\approx 4 \times 10^4$ m/s. The ion sound speed for the plasma is 2.3×10^4 m/s. This corresponds to a Mach number ≈ 1.5, which agrees with Mach probe results depicted in figure 4.4b.

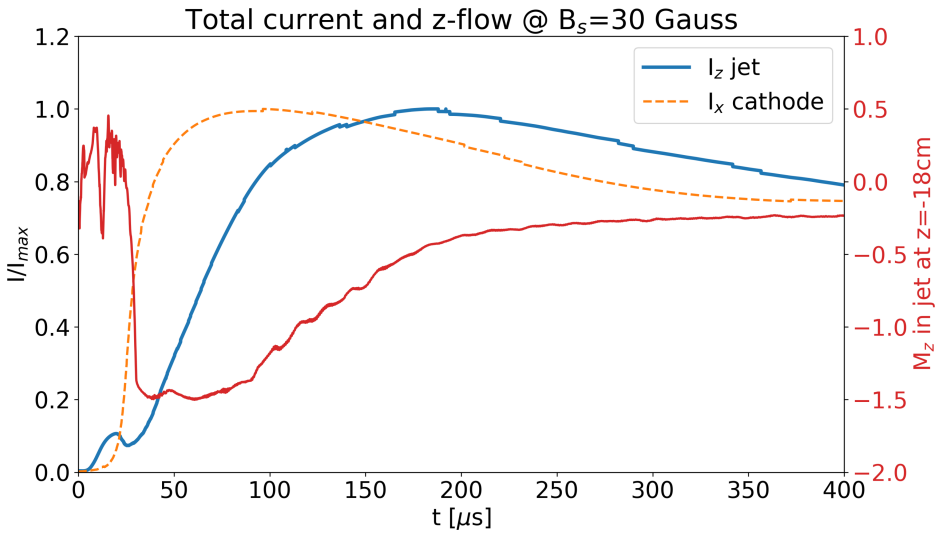

Figure 4.8: Temporal evolution of the total current leaving the cathode (dashed orange), the total jet current in the +z-direction at z = -18 cm (blue solid). Both current traces are normalized to their respective maxima. The jet z-flow velocity at z=-18 cm is expressed in terms of Mach number (solid red). The total current was obtained by integration of the measured current density in the area of interest. The flow velocity trace was obtained by averaging Mach probe data over the center of the structure in figure 4.4(b). Evidently, the electric current in the jet develops on a slower time scale than the current leaving the cathode, and its formation is concurrent with the appearance of supersonic flows. This implies that the jet is formed due to dynamic processes in the arched plasma and not due to plasma leakage from the arch along static magnetic field lines. The sharp, transient flow and the distinct electric current evolution indicate the formation of a dynamic plasma jet during an eruptive event in the arch plasma.

delay with respect to that in the arch. The distinct electric current evolution of the jet marks its own dynamics, which cannot be described as a leakage from the arched plasma.

4.3.5 Supersonic Flow Driving Force

The supersonic flow in the jet develops along with the eruptive event during the initial formation spike in the density trace. Since its onset, the jet supersonic flow persists for around 100 μs until it starts to decay, approaching zero around the resistive diffusion timescale. This flow decay implies a transient nature of the jet. The free energy driving the supersonic flow comes from the large magnetic pressure gradient between the arched plasma and the jet. In addition, there is a thermal pressure gradient between these locations fueling the flow. Both pressure differences, along with the kinetic energy in the jet, are plotted in Figure 4.9. The magnetic pressure trace reacts first to the formation of the arched plasma. The kinetic energy in the jet builds up shortly after, along with the thermal pressure difference, when the jet structure forms. In later stages, the gradient in thermal pressure reverses direction as the pressure in the jet exceeds that in the middle of the arched plasma.

4.3.6 Current Channels and the Return Path

There are two distinct current channels along the axis of the machine visible in XY planes of figure 4.2(b). The channel closer to the arched plasma (red) consists of outgoing electrons, while the (blue) corresponds to returning electrons. These two channels remain separate for a relatively large distance ($\approx$ 1.5 m) along the z-axis. The current density data from z = -60 cm plane is shown in figure 4.10(a), in which color fill corresponds to $j_z = j_{\|}$ and the vectors correspond to $j_{\perp}$ (diamagnetic current as per earlier discussion). All of the jet electron current returns to the anode footpoint via the return channel (a dark-blue patch in Figure 4.10) since the $j_{\|}$ integrates to zero over any transversal plane of collected data. The total current in each channel can be traced in time for various z-locations simply by integrating the current density over the area of that

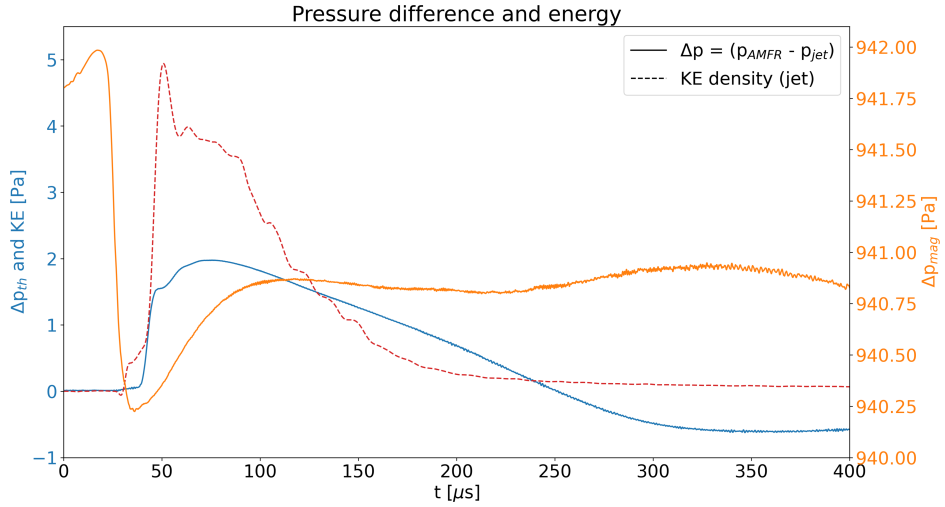

Figure 4.9: Temporal evolution of pressure difference between the center of arched plasma and the center of the jet at z = -18 cm. A thermal pressure difference is plotted in solid blue, with the scale on the left-hand side. The magnetic pressure difference is plotted in solid orange with the scale on the right-hand side. The red dashed line corresponds to the kinetic energy density in the jet, measured at z = -18 cm, with the corresponding scale on the left-hand side. A large gradient in the magnetic pressure between the arch and the jet's location is the primary driving force for the supersonic flow during the early stages of the jet eruption. The gradient in thermal pressure develops along the jet and provides a further driving force to the flow.

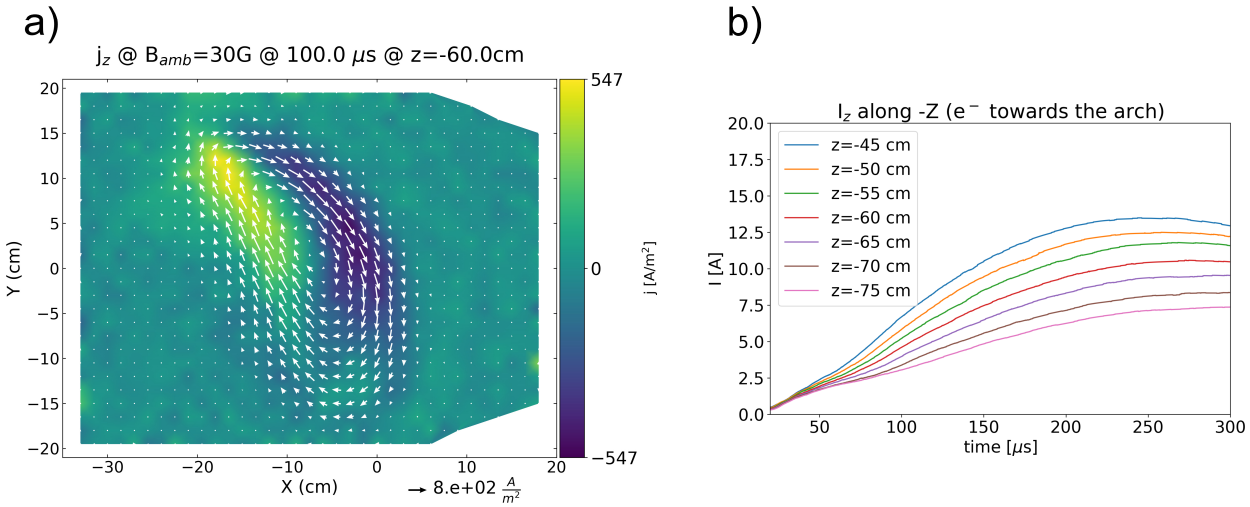

Figure 4.10: **(a)** The current density in the XY plane at z = -60 cm and t = 100 μs. The fill corresponds to the z-component ($j_{\parallel}$) with color scale on the right side, while the white vectors represent $j_{\perp}$ with the legend on the bottom. **(b)** Temporal evolution of total return current to the arch plasma [enclosed in the dark-blue colored region in panel (a)] at multiple axial locations on the device. In panel (a), electrons moving away from the arch constitute the positive (outgoing) channel, while the returning electrons comprise the negative channel. The total current in each of the two channels steadily decreases with axial distance from the arched plasma source. The cross-field current closure between these current channels is facilitated by ion-neutral collisions. This cross-field current density was $\approx$ 100 A/m^2.

channel. The time traces for total current in the electron return channel are presented in figure 4.10(b). The total current in these channels gradually decreases with distance (along the axis of the machine) from the arched plasma. This implies a gradual cross-field current along the length of the jet. The magnitude of this cross-field current density between channels was estimated to be around 100 A/m^2. A relatively high density of background neutral helium in these experiments (3×10^{14} cm^{-3}) allows for an ion-neutral collision rate high enough to facilitate the cross-field current in the jet. The elastic and charge transfer ion-neutral collision frequency in the jet were calculated [85, 84] to be 5.4×10^5 Hz and 1.6×10^5 Hz, respectively. Since the ion cyclotron frequency in the middle of the jet is $\approx 10^4$ Hz, the ions there fall into the collisional regime ($\Omega_i \tau_{in} << 1$), similar to the plasma in the solar photosphere and chromosphere [86]. The jet electron current return path is visualized in a 3D rendering of the measured current density in Figure 4.11. The return and the outgoing jet current channels turn sharply around the magnetic null. In that area, the magnetic field is low enough, allowing for the cross-field electron current. Figures 4.10 and 4.11 show that the two channels are not concentric. Instead, they are positioned side by side, with the return electron current channel farther along the x-axis (away from the arch). The electrons returning in this channel are forced to that particular path because it crosses the weakest magnetic field lines. A similar path shifted toward the negative x-axis would involve crossing a magnetic field up to 800 Gauss in magnitude (the arched magnetic field is very strong near the footpoints). Two oppositely directed, side-by-side current channels are also observed on the Sun (e.g., coronal cavities) [114, 115], and in other laboratory experiments [116]. Even though our experiment is not exactly in the same parameter regime, the physics leading to this channel arrangement might still be relevant.

4.4 Summary

The formation of a jet structure from an eruptive laboratory arched magnetized plasma has been observed, and in-depth studies focused on the characteristics of the jet were performed. This exper-

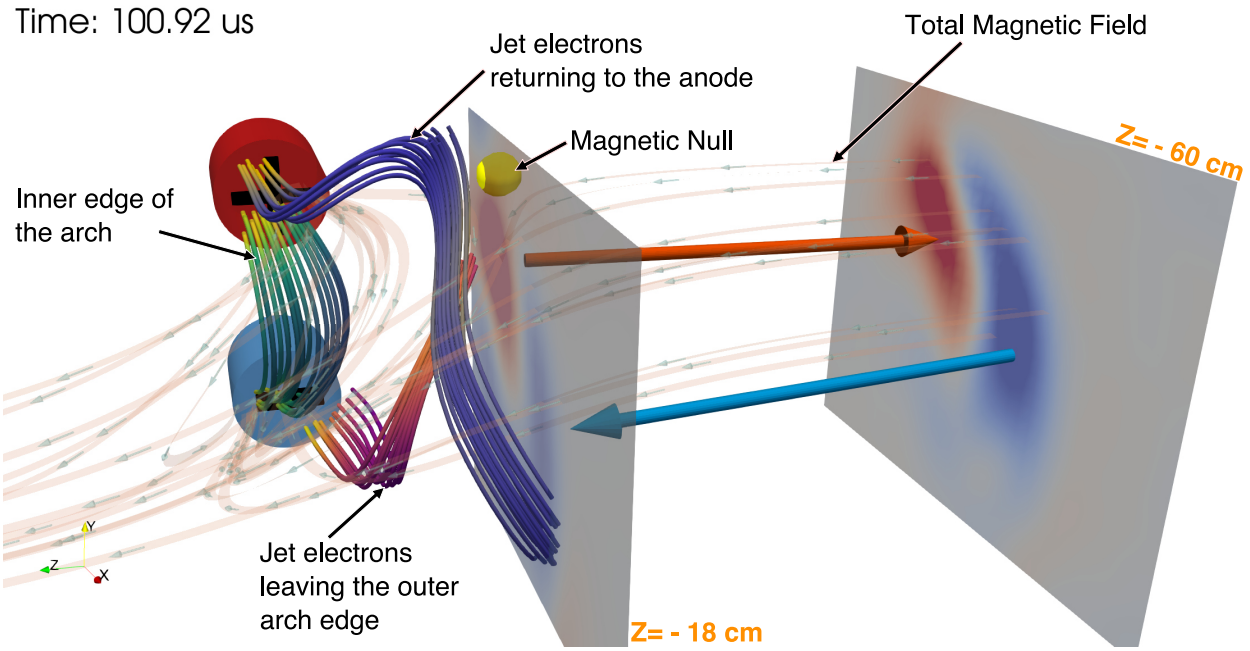

Figure 4.11: A 3D rendering of the current density measured 100.92 μs after the discharge trigger, visualizing a jet electron current return path to the anode. All current density channels are represented by tubes and labeled in the figure. The total magnetic field is rendered as translucent ribbons with arrows. The cathode and anode footpoints are rendered as blue and red cylinders with '-' and '+' marks, respectively. Two planes represent the magnitude of $j_z = j_{\|}$ current density, where blue corresponds to the positive electron current, and red corresponds to the negative electron current along the z-axis. Two large arrows (blue and red) are added as a visual aid for the direction of electron current. Both the outgoing and the returning electron current channels sharply turn near the magnetic null, represented as a yellow sphere. The return channel is forced towards the path crossing the weakest magnetic field lines.

iment was designed to capture the dynamics of arched plasma structures on the Sun, with relative parameters relevant to those found in the lower solar atmosphere (photosphere and chromosphere). The transient jet structure forms in the presence of a strapping magnetic field, which introduces a shear to the guiding magnetic field. The total electrical current in the arched plasma is kept below 150 Amps, preventing kink instability growth. The strapping field has no decay index, which rules out the torus instability. The interaction between the developing flux of the arched plasma and the pre-existing strapping magnetic field triggers an eruption (within the first few Alfvén times of arched plasma formation), forming a jet. A possible role of magnetic reconnection in driving the eruption will be explored in future work. This could be relevant to the flux rope formation on the Sun as a result of the interaction between flux emerging from the photosphere and the pre-existing coronal magnetic field [33]. Experimental data show signs of eruption both in temporal and spatial domains. The jet is characterized by a supersonic ion flow (Mach 1.5 ± 0.1) fueled by a large gradient in magnetic pressure. The thermal pressure gradient is also present (on a much smaller scale), further contributing to the flow. The jet consists of two electric current channels, one towards and another away from the arch. The high twist in the measured current density is a result of the diamagnetic current caused by a high thermal pressure gradient at the boundary of the jet. The current path closure between the channels is facilitated by ion-neutral charge-transfer collisions along the length of the jet. The high collisionality of ions in this experiment is relevant to the conditions of the Sun's photosphere. The total current in the arched plasma and the jet evolve at different rates and on different timescales. This implies that the jet is a dynamic structure.

CHAPTER 5

Summary and Future Work

In this work, we have studied laboratory arched magnetized plasma structures that are relevant to similar phenomena found on the Sun (e.g., solar prominences, microfilaments). These structures are found throughout the Sun's atmosphere and can significantly impact Earth through eruptive events, e.g., solar flares or coronal mass ejections. The arched plasma structures found in the lower solar atmosphere (photosphere and lower chromosphere) often give rise to phenomena like anemone jets or solar spicules. The goal of this research was to gain a deeper understanding of the dynamics of these phenomena, such that we might be able to predict them in the future.

This experiment was designed to capture the dynamics of arched plasma structures, with relative parameters kept relevant to those found in the lower solar atmosphere. There, a relatively low ionization level leads to significant ion-neutral collisionality. The relatively high neutral Helium density presence is unique to this experiment and allows for a more accurate representation of lower solar atmosphere conditions. Moreover, by keeping the arched plasma electrical current low, we preserve the relative magnitudes of major forces relevant to those found on the Sun. The low current also prevents kink instability in the plasma. The lack of a decay index in the overlying magnetic field also eliminates torus instability from this system. In light of that, our unique experimental setup allows us to study the eruptive behavior without these instabilities, which are often attributed to eruption drivers.

In chapter 3, we conducted a detailed study on the effects of a nearly horizontal overlying magnetic field on the evolution and morphology of an arched magnetized plasma. Our results show that the characteristic sigmoid shape of arched plasma structures is naturally produced in a

sheared magnetic configuration, even in the absence of kink instability. The shear angle critically depends on the magnitude of the overlying magnetic field and the direction of the guiding magnetic field. Forward-S-shaped arched plasma was observed for a guiding magnetic field oriented nearly antiparallel to the initial arched plasma current. The parallel orientation yielded the reverse-S-shaped arched plasma. This suggests that the apparent writhe of a current-carrying arched plasma strongly depends on the structure of the guiding magnetic field, not just on the magnitude of the electrical current. On the Sun, the reverse-S-shaped structures dominate the Northern Hemisphere, while forward-S-shaped structures are more abundant in the Southern Hemisphere. Our results might shed some light on this correlation.

Chapter 4 was focused on the study of the formation of a jet structure out of the laboratory arched magnetized plasma. The transient jet structure forms in the presence of a strong strapping magnetic field, which introduces a shear to the guiding magnetic field. The interaction between the developing flux of the arched plasma and the pre-existing strapping magnetic field triggers an eruption, forming a jet-like structure. For the experiments in this chapter, the background plasma was not employed in order to eliminate it as an eruption contributor. Our data show signs of eruption both in temporal and spatial domains. The jet is characterized by a supersonic ion flow (Mach 1.5) fueled by a large gradient in magnetic pressure. The jet consists of two electric current channels, one towards and one away from the arch. The high twist in the measured current density results from the diamagnetic current caused by a high thermal pressure gradient at the boundary of the jet. The investigated jet could be relevant to the flux rope formation on the Sun due to the interaction between flux emerging from the photosphere and the pre-existing coronal magnetic field.

There are several directions for future work on this topic. One possible avenue for research is the investigation of the magnetic shear's role in the properties and behavior of the ejected flux rope. Additionally, the study of the evolution of the arched plasma in the non-zero decay index overlying magnetic field (strapping field) could also provide valuable insights. In this scenario, it would be possible to introduce a torus instability to this system [77, 78]. The capabilities of this experiment

would allow for a detailed study of torus-unstable arched plasma eruptions. The investigation of the role of magnetic reconnection, Alfvén waves, and global oscillations during and after eruptions is another area that could be explored in future studies. Furthermore, the causes and implications of non-force-free configurations in energy storage and triggering the eruption should be further investigated.

In conclusion, this dissertation has contributed to our understanding of arched plasma structures on the Sun, with a particular focus on the lower solar atmosphere. Our laboratory experiments have provided new insights into these phenomena' dynamics and highlighted several areas for future research. We hope that this work will aid the future development of predictive models for similar solar structures and eruptive events.

REFERENCES

[1] K. R. Lang, *The Cambridge encyclopedia of the sun*. Cambridge: Cambridge University Press, 2001.

[2] K. A. P. Singh, K. Shibata, N. Nishizuka, and H. Isobe, "Chromospheric anemone jets and magnetic reconnection in partially ionized solar atmosphere," *Physics of Plasmas*, vol. 18, p. 111210, Nov. 2011.

[3] E. Khomenko and M. Collados, "HEATING OF THE MAGNETIZED SOLAR CHROMOSPHERE BY PARTIAL IONIZATION EFFECTS," *ApJ*, vol. 747, p. 87, Mar. 2012.

[4] J. I. Sakai and P. D. Smith, "TWO-FLUID SIMULATIONS OF COALESCING PENUMBRA FILAMENTS DRIVEN BY NEUTRAL-HYDROGEN FLOWS," *ApJ*, vol. 691, pp. L45–L48, Jan. 2009.

[5] P. Mein, P. Demoulin, N. Mein, O. Engvold, R. Molowny-Horas, P. Heinzel, and C. Gontikakis, "Dynamics of solar magnetic arches in the photosphere and the chromosphere.," *Astronomy and Astrophysics*, vol. 305, p. 343, Jan. 1996.

[6] Y. C. A, *The Sun*. New York: D. Appleton and Co., 1900.

[7] R. Casini, A. L. Ariste, S. Tomczyk, and B. W. Lites, "Magnetic maps of prominences from full stokes analysis of the he i d3 line," *The Astrophysical Journal*, vol. 598, pp. L67–L70, nov 2003.

[8] H. Lin, M. J. Penn, and S. Tomczyk, "A new precise measurement of the coronal magnetic field strength," *The Astrophysical Journal*, vol. 541, p. L83, sep 2000.

[9] E. Landi and F. Reale, "Prominence plasma diagnostics through extreme-ultraviolet absorption," *The Astrophysical Journal*, vol. 772, p. 71, jul 2013.

[10] M. J. Aschwanden, *Physics of the Solar Corona: An Introduction With Problems and Solutions (Springer-Praxis Books in Geophysical Sciences)*. Springer Verlag, 2005.

[11] S. Parenti, "Solar prominences: observations," *Living Reviews in Solar Physics*, vol. 11, pp. 1–88, 2014.

[12] S. Liu, H. Zhang, and J. Su, "Comparison of nonlinear force-free field and potential field in the quiet sun," *Solar Physics*, vol. 270, pp. 89–107, 2011.

[13] Y. Liu and H. Lin, "Observational test of coronal magnetic field models. i. comparison with potential field model," *The Astrophysical Journal*, vol. 680, no. 2, p. 1496, 2008.

[14] R. Esser and R. J. Edgar, "Reconciling spectroscopic electron temperature measurements in the solar corona with in situ charge state observations," *The Astrophysical Journal*, vol. 532, no. 1, p. L71, 2000.

[15] E. Tandberg-Hanssen, *Solar prominences*, vol. 12. Springer Science & Business Media, 2012.

[16] E. R. Priest, A. A. van Ballegooijen, and D. H. Mackay, "A Model for Dextral and Sinistral Prominences," *The Astrophysical Journal*, vol. 460, p. 530, Mar. 1996.

[17] Y. Nakagawa, M. Raadu, D. Billings, and D. McNamara, "On the topology of filaments and chromospheric fibrils near sunspots," *Solar Physics*, vol. 19, no. 1, pp. 72–85, 1971.

[18] Y. Nakagawa, "A Practical Representation of the Solar Magnetic Field," *Astronomy and Astrophysics*, vol. 27, p. 95, Aug. 1973.

[19] T. Török, B. Kliem, and V. Titov, "Ideal kink instability of a magnetic loop equilibrium," *Astronomy & Astrophysics*, vol. 413, no. 3, pp. L27–L30, 2004.

[20] J. Chen, "Physics of erupting solar flux ropes: Coronal mass ejections (cmes)-recent advances in theory and observation," *Physics of Plasmas*, vol. 24, p. 090501, 2017.

[21] E. Pettit, "Characteristic Features of Solar Prominences," *The Astrophysical Journal*, vol. 76, p. 9, July 1932.

[22] J. F. Hansen, *Laboratory simulations of solar prominences*. PhD thesis, California Institute of Technology, Aug. 2001. Medium: PDF Version Number: Final.

[23] K. R. Lang, *The Cambridge Encyclopedia of the Sun*, pp. 106–143. Cambridge, England: Cambridge University Press, 1 ed., 2001.

[24] J. Chen, "Theory of prominence eruption and propagation: Interplanetary consequences," *Journal of Geophysical Research: Space Physics*, vol. 101, pp. 27499–27519, 1996.

[25] E. Hildner, J. T. Gosling, R. M. MacQueen, R. H. Munro, A. I. Poland, and C. L. Ross, "The large coronal transient of 10 june 1973: I : Observational description," *Solar Physics*, vol. 42, no. 1, pp. 163–177, 1975.

[26] H. Cremades and V. Bothmer, "On the three-dimensional configuration of coronal mass ejections," *Astronomy & Astrophysics*, vol. 422, no. 1, pp. 307–322, 2004.

[27] C. Abbot, *The Sun*, p. 128. New York: D. Appleton and Company, 1911.

[28] R. Rosner, W. H. Tucker, and G. S. Vaiana, "Dynamics of the quiescent solar corona," *The Astrophysical Journal*, vol. 220, p. 643, 1978.

[29] L. Burlaga, "Magnetic clouds and force-free fields with constant alpha," *Journal of Geophysical Research: Space Physics*, vol. 93, no. A7, pp. 7217–7224, 1988.

[30] D. Rust, "Spawning and shedding helical magnetic fields in the solar atmosphere," *Geophysical Research Letters*, vol. 21, no. 4, pp. 241–244, 1994.

[31] A. Thomson, C. Gaunt, P. Cilliers, J. Wild, B. Opperman, L.-A. McKinnell, P. Kotze, C. Ngwira, and S. Lotz, "Present day challenges in understanding the geomagnetic hazard to national power grids," *Advances in Space Research*, vol. 45, no. 9, pp. 1182 – 1190, 2010.

[32] C. E. Myers, M. Yamada, H. Ji, J. Yoo, W. Fox, J. Jara-Almonte, A. Savcheva, and E. E. DeLuca, "A dynamic magnetic tension force as the cause of failed solar eruptions," *Nature*, vol. 528, pp. 526–529, Dec. 2015.

[33] V. Archontis and T. Török, "Eruption of magnetic flux ropes during flux emergence," *A&A*, vol. 492, pp. L35–L38, Dec. 2008.

[34] P. F. Wyper, S. K. Antiochos, and C. R. DeVore, "A universal model for solar eruptions," *Nature*, vol. 544, pp. 452–455, Apr. 2017.

[35] K. Muglach, "The Photospheric Footpoints of Solar Coronal Hole Jets," *ApJ*, vol. 909, p. 133, Mar. 2021.

[36] J. Cirtain, L. Golub, L. Lundquist, A. Van Ballegooijen, A. Savcheva, M. Shimojo, E. DeLuca, S. Tsuneta, T. Sakao, K. Reeves, *et al.*, "Evidence for alfvén waves in solar x-ray jets," *Science*, vol. 318, no. 5856, pp. 1580–1582, 2007.

[37] A. C. Sterling, R. L. Moore, D. A. Falconer, and M. Adams, "Small-scale filament eruptions as the driver of x-ray jets in solar coronal holes," *Nature*, vol. 523, no. 7561, pp. 437–440, 2015.

[38] A. C. Sterling, R. L. Moore, D. A. Falconer, N. K. Panesar, S. Akiyama, S. Yashiro, and N. Gopalswamy, "Minifilament eruptions that drive coronal jets in a solar active region," *The Astrophysical Journal*, vol. 821, no. 2, p. 100, 2016.

[39] T. Yokoyama and K. Shibata, "Magnetic reconnection as the origin of x-ray jets and hα surges on the sun," *Nature*, vol. 375, no. 6526, pp. 42–44, 1995.

[40] K. Shibata, Y. Ishido, L. W. Acton, K. T. Strong, T. Hirayama, Y. Uchida, A. H. McAllister, R. Matsumoto, S. Tsuneta, T. Shimizu, *et al.*, "Observations of x-ray jets with the yohkoh soft x-ray telescope," *Publications of the Astronomical Society of Japan*, vol. 44, pp. L173–L179, 1992.

[41] A. C. Sterling, "SOLAR SPICULES: A REVIEW OF RECENT MODELS AND TARGETS FOR FUTURE OBSERVATIONS," *Solar Physics*, vol. 196, no. 1, pp. 79–111, 2000.

[42] A. C. Sterling and R. L. Moore, "A microfilament-eruption mechanism for solar spicules," *The Astrophysical Journal Letters*, vol. 828, no. 1, p. L9, 2016.

[43] James, S. P., Erdélyi, R., and De Pontieu, B., "Can ion-neutral damping help to form spicules?," *A&A*, vol. 406, no. 2, pp. 715–724, 2003.

[44] T. Török, O. Panasenco, V. Titov, Z. Mikić, K. Reeves, M. Velli, J. Linker, and G. De Toma, "A model for magnetically coupled sympathetic eruptions," *The Astrophysical Journal Letters*, vol. 739, no. 2, p. L63, 2011.

[45] Y. Fan, "Coronal mass ejections as loss of confinement of kinked magnetic flux ropes," *The Astrophysical Journal*, vol. 630, no. 1, p. 543, 2005.

[46] B. Low, "Coronal mass ejections, magnetic flux ropes, and solar magnetism," *Journal of Geophysical Research: Space Physics*, vol. 106, no. A11, pp. 25141–25163, 2001.

[47] P. Chen, "Coronal mass ejections: models and their observational basis," *Living Reviews in Solar Physics*, vol. 8, no. 1, p. 1, 2011.

[48] S. K. P. Tripathi and W. Gekelman, "Laboratory Simulation of Arched Magnetic Flux Rope Eruptions in the Solar Atmosphere," *Physical Review Letters*, vol. 105, p. 075005, Aug. 2010.

[49] S. K. P. Tripathi, P. M. Bellan, and G. S. Yun, "Observation of Kinetic Plasma Jets in a Coronal-Loop Simulation Experiment," *Physical Review Letters*, vol. 98, p. 135002, Mar. 2007.

[50] W. H. Bostick, "Simulation of Solar Prominence in the Laboratory," *Physical Review*, vol. 104, pp. 1191–1193, Nov. 1956.

[51] P. M. Bellan and J. F. Hansen, "Laboratory simulations of solar prominence eruptions," *Physics of Plasmas*, vol. 5, pp. 1991–2000, May 1998.

[52] J. F. Hansen, S. K. P. Tripathi, and P. M. Bellan, "Co- and counter-helicity interaction between two adjacent laboratory prominences," *Physics of Plasmas*, vol. 11, pp. 3177–3185, June 2004.

[53] S. C. Hsu and P. M. Bellan, "Experimental Identification of the Kink Instability as a Poloidal Flux Amplification Mechanism for Coaxial Gun Spheromak Formation," *Physical Review Letters*, vol. 90, p. 215002, May 2003.

[54] L. Arnold, J. Dreher, R. Grauer, H. Soltwisch, and H. Stein, "Three-dimensional magneto-hydrodynamical simulation of expanding magnetic flux ropes," *Physics of Plasmas*, vol. 15, no. 4, p. 042106, 2008.

[55] H. Soltwisch, P. Kempkes, F. Mackel, H. Stein, J. Tenfelde, L. Arnold, J. Dreher, and R. Grauer, "FlareLab: early results," *Plasma Physics and Controlled Fusion*, vol. 52, p. 124030, Dec. 2010.

[56] C. E. Myers, Princeton University, and Department of Astrophysical Sciences, *Laboratory study of the equilibrium and eruption of line-tied magnetic flux ropes in the solar corona.* PhD thesis, 2015. ISBN: 9781321565430 OCLC: 936630881.

[57] C. E. Myers, M. Yamada, H. Ji, J. Yoo, J. Jara-Almonte, and W. Fox, "Laboratory study of low-β forces in arched, line-tied magnetic flux ropes," *Physics of Plasmas*, vol. 23, p. 112102, Nov. 2016.

[58] W. Gekelman, J. Maggs, and H. Pfister, "Experiments on the interaction of current channels in a laboratory plasma: relaxation to the force-free state," *IEEE Transactions on Plasma Science*, vol. 20, pp. 614–621, Dec. 1992.

[59] W. F. Bergerson, C. B. Forest, G. Fiksel, D. A. Hannum, R. Kendrick, J. S. Sarff, and S. Stambler, "Onset and Saturation of the Kink Instability in a Current-Carrying Line-Tied Plasma," *Physical Review Letters*, vol. 96, p. 015004, Jan. 2006.

[60] T. P. Intrator, X. Sun, G. Lapenta, L. Dorf, and I. Furno, "Experimental onset threshold and magnetic pressure pile-up for 3D reconnection," *Nature Physics*, vol. 5, pp. 521–526, July 2009.

[61] E. E. Lawrence and W. Gekelman, "Identification of a Quasiseparatrix Layer in a Reconnecting Laboratory Magnetoplasma," *Physical Review Letters*, vol. 103, p. 105002, Sept. 2009.

[62] I. Furno, T. P. Intrator, D. D. Ryutov, S. Abbate, T. Madziwa-Nussinov, A. Light, L. Dorf, and G. Lapenta, "Current-Driven Rotating-Kink Mode in a Plasma Column with a Non-Line-Tied Free End," *Physical Review Letters*, vol. 97, p. 015002, July 2006.

[63] J. L. Leroy, V. Bommier, and S. Sahal-Brechot, "The Magnetic Field in the Prominences of the Polar Crown," *Solar Physics*, vol. 83, pp. 135–142, Feb. 1983.

[64] S. K. P. Tripathi and W. Gekelman, "Dynamics of an Erupting Arched Magnetic Flux Rope in a Laboratory Plasma Experiment," *Solar Physics*, vol. 286, pp. 479–492, Sept. 2013.

[65] V. Shafranov, "Plasma equilibrium in a magnetic field," *Reviews of plasma physics*, vol. 2, p. 103, 1966.

[66] P. F. Wyper, S. K. Antiochos, and C. R. DeVore, "A universal model for solar eruptions," *Nature*, vol. 544, pp. 452–455, Apr. 2017.

[67] T. Török and B. Kliem, "Confined and ejective eruptions of kink-unstable flux ropes," *The Astrophysical Journal Letters*, vol. 630, no. 1, p. L97, 2005.

[68] P. A. Sturrock, M. Weber, M. S. Wheatland, and R. Wolfson, "Metastable magnetic configurations and their significance for solar eruptive events," *The Astrophysical Journal*, vol. 548, no. 1, p. 492, 2001.

[69] T. Sakurai, "Magnetohydrodynamic interpretation of the motion of prominences," *Publications of the Astronomical Society of Japan*, vol. 28, pp. 177–198, 1976.

[70] M. A. Berger and C. Prior, "The writhe of open and closed curves," *Journal of Physics A: Mathematical and General*, vol. 39, no. 26, p. 8321, 2006.

[71] T. Török, B. Kliem, M. A. Berger, M. G. Linton, P. Demoulin, and L. van Driel-Gesztelyi, "The evolution of writhe in kink-unstable flux ropes and erupting filaments," *Plasma Physics and Controlled Fusion*, vol. 56, no. 6, p. 064012, 2014.

[72] A. Hood and E. Priest, "Critical conditions for magnetic instabilities in force-free coronal loops," *Geophysical & Astrophysical Fluid Dynamics*, vol. 17, no. 1, pp. 297–318, 1981.

[73] V. Shafranov, "The structure of shock waves in a plasma," *Soviet Phys. JETP*, vol. 5, 1957.

[74] M. Kruskal and J. Tuck, "The instability of a pinched fluid with a longitudinal magnetic field," *Proceedings of the Royal Society of London. Series A. Mathematical and Physical Sciences*, vol. 245, no. 1241, pp. 222–237, 1958.

[75] J. P. Freidberg, "Ideal magnetohydrodynamic theory of magnetic fusion systems," *Reviews of Modern Physics*, vol. 54, no. 3, p. 801, 1982.

[76] E. R. Priest, *Solar Magnetohydrodynamics*. Dordrecht: Springer Netherlands, 1982.

[77] B. Kliem and T. Török, "Torus instability," *Phys. Rev. Lett.*, vol. 96, p. 255002, Jun 2006.

[78] G. Bateman, *MHD instabilities*. Cambridge, MA: Massachusetts Institute of Technology Press, 1 1978.

[79] J. E. Vernazza, E. H. Avrett, and R. Loeser, "Structure of the solar chromosphere. iii. models of the euv brightness components of the quiet sun," *The Astrophysical Journal Supplement Series*, vol. 45, pp. 635–725, 4 1981.

[80] B. Pandey and M. Wardle, "Hall magnetohydrodynamics of partially ionized plasmas," *Monthly Notices of the Royal Astronomical Society*, vol. 385, no. 4, pp. 2269–2278, 2008.

[81] J. E. Leake, T. D. Arber, and M. L. Khodachenko, "Collisional dissipation of Alfvén waves in a partially ionised solar chromosphere," *A&A*, vol. 442, pp. 1091–1098, Nov. 2005.

[82] T. D. Arber, G. J. J. Botha, and C. S. Brady, "Effect of solar chromospheric neutrals on equilibrium field structures," *The Astrophysical Journal*, vol. 705, p. 1183, oct 2009.

[83] H. R. Gilbert, V. H. Hansteen, and T. E. Holzer, "Neutral atom diffusion in a partially ionized prominence plasma," *The Astrophysical Journal*, vol. 577, p. 464, sep 2002.

[84] J. L. Ballester, I. Alexeev, M. Collados, T. Downes, R. F. Pfaff, H. Gilbert, M. Khodachenko, E. Khomenko, I. F. Shaikhislamov, R. Soler, E. Vázquez-Semadeni, and T. Zaqarashvili, "Partially Ionized Plasmas in Astrophysics," *Space Sci Rev*, vol. 214, p. 58, Mar. 2018.

[85] J. Barata and C. Conde, "Elastic He+ on He collision cross-sections and Monte Carlo calculation of the transport coefficients of He+ ions in gaseous helium," *Nuclear Instruments and Methods in Physics Research Section A: Accelerators, Spectrometers, Detectors and Associated Equipment*, vol. 619, pp. 21–23, July 2010.

[86] J. Vranjes, S. Poedts, and B. P. Pandey, "Comment on "Heating of the Solar Corona by Dissipative Alfvén Solitons"," *Phys. Rev. Lett.*, vol. 98, p. 049501, Jan. 2007.

[87] E. R. Priest and A. W. Hood, *Advances in solar system magnetohydrodynamics*. Cambridge University Press, 1991.

[88] Y.-H. Zhou, C. Xia, R. Keppens, C. Fang, and P. Chen, "Three-dimensional mhd simulations of solar prominence oscillations in a magnetic flux rope," *The Astrophysical Journal*, vol. 856, no. 2, p. 179, 2018.

[89] P. M. Bellan, *Fundamentals of plasma physics*. Cambridge university press, 2008.

[90] R. T. Gangadhara, V. Krishan, A. K. Bhowmick, and S. M. Chitre, "GENERATION OF MAGNETIC STRUCTURES ON THE SOLAR PHOTOSPHERE," *ApJ*, vol. 788, p. 135, June 2014.

[91] C. M. Cooper and W. Gekelman, "Termination of a Magnetized Plasma on a Neutral Gas: The End of the Plasma," *Physical Review Letters*, vol. 110, p. 265001, June 2013.

[92] C. M. Cooper, W. Gekelman, P. Pribyl, and Z. Lucky, "A new large area lanthanum hexaboride plasma source," *Review of Scientific Instruments*, vol. 81, no. 8, p. 083503, 2010.

[93] W. Gekelman, P. Pribyl, Z. Lucky, M. Drandell, D. Leneman, J. Maggs, S. Vincena, B. Van Compernolle, S. K. P. Tripathi, G. Morales, T. A. Carter, Y. Wang, and T. DeHaas, "The upgraded large plasma device, a machine for studying frontier basic plasma physics," *Review of Scientific Instruments*, vol. 87, no. 2, p. 025105, 2016.

[94] K. U. Riemann, "The bohm criterion and sheath formation," *Journal of Physics D: Applied Physics*, vol. 24, p. 493, apr 1991.

[95] I. H. Hutchinson, *Principles of Plasma Diagnostics*. Cambridge University Press, 2 ed., 2002.

[96] S. Chen and T. Sekiguchi, "Instantaneous Direct-Display System of Plasma Parameters by Means of Triple Probe," *Journal of Applied Physics*, vol. 36, pp. 2363–2375, Aug. 1965.

[97] M. Podestà, A. Fasoli, B. Labit, M. McGrath, S. H. Müller, and F. M. Poli, "Plasma production by low-field side injection of electron cyclotron waves in a simple magnetized torus," *Plasma Physics and Controlled Fusion*, vol. 47, p. 1989, oct 2005.

[98] M. Hudis and L. M. Lidsky, "Directional langmuir probe," *Journal of Applied Physics*, vol. 41, no. 12, pp. 5011–5017, 1970.

[99] T. Wiegelmann and T. Sakurai, "Solar Force-free Magnetic Fields," *Living Reviews in Solar Physics*, vol. 9, 2012.

[100] Török, T., Berger, M. A., and Kliem, B., "The writhe of helical structures in the solar corona," *A&A*, vol. 516, p. A49, 2010.

[101] D. M. Rust and A. Kumar, "Evidence for helically kinked magnetic flux ropes in solar eruptions," *The Astrophysical Journal Letters*, vol. 464, no. 2, p. L199, 1996.

[102] V. Archontis, F. Moreno-Insertis, K. Galsgaard, and A. W. Hood, "The Three-dimensional Interaction between Emerging Magnetic Flux and a Large-Scale Coronal Field: Reconnection, Current Sheets, and Jets," *The Astrophysical Journal*, vol. 635, pp. 1299–1318, Dec. 2005.

[103] T. Yokoyama and K. Shibata, "Numerical Simulation of Solar Coronal X-Ray Jets Based on the Magnetic Reconnection Model," *Publications of the Astronomical Society of Japan*, vol. 48, pp. 353–376, Apr. 1996.

[104] F. Yuan, J. Lin, K. Wu, and L. C. Ho, "A magnetohydrodynamical model for the formation of episodic jets," *Monthly Notices of the Royal Astronomical Society*, vol. 395, pp. 2183–2188, June 2009.

[105] R. Canfield, H. Hudson, and A. Pevtsov, "Sigmoids as precursors of solar eruptions," *IEEE Transactions on Plasma Science*, vol. 28, no. 6, pp. 1786–1794, 2000.

[106] C. R. DeVore and S. K. Antiochos, "Dynamical formation and stability of helical prominence magnetic fields," *The Astrophysical Journal*, vol. 539, pp. 954–963, aug 2000.

[107] A. N. McClymont, L. Jiao, and Z. Mikic, "Problems and Progress in Computing Three-Dimensional Coronal Active Region Magnetic Fields from Boundary Data," *Solar Physics*, vol. 174, pp. 191–218, Aug. 1997.

[108] F. Moreno-Insertis and K. Galsgaard, "PLASMA JETS AND ERUPTIONS IN SOLAR CORONAL HOLES: A THREE-DIMENSIONAL FLUX EMERGENCE EXPERIMENT," *ApJ*, vol. 771, p. 20, June 2013.

[109] J. F. Hansen and P. M. Bellan, "Experimental demonstration of how strapping fields can inhibit solar prominence eruptions," *The Astrophysical Journal*, vol. 563, p. L183, dec 2001.

[110] K. D. Sklodowski, S. Tripathi, and T. Carter, "Evolution of an arched magnetized laboratory plasma in a sheared magnetic field," *Journal of Plasma Physics*, vol. 87, no. 6, p. 905870616, 2021.

[111] F. F. Chen, *Introduction to Plasma Physics and Controlled Fusion*. Cham: Springer International Publishing, 2016.

[112] J. Vranjes and S. Poedts, "Diamagnetic current does not produce an instability in the solar corona," *Astronomy and Astrophysics*, vol. 503, pp. 591–593, Aug. 2009.

[113] H. Saleem, J. Vranjes, and S. Poedts, "Unstable drift mode driven by shear plasma flow in solar spicules," *Astronomy and Astrophysics*, vol. 471, pp. 289–293, Aug. 2007.

[114] C. Greifinger and J. D. Cole, "On cylindrical magnetohydrodynamic shock waves," *The Physics of Fluids*, vol. 4, no. 5, pp. 527–534, 1961.

[115] K. Saito and C. L. Hyder, "A concentric ellipse multiple-arch system in the solar corona," *Solar Physics*, vol. 5, pp. 61–86, 1968.

[116] M. A. Haw, P. Wongwaitayakornkul, H. Li, and P. M. Bellan, "Reverse current model for coronal mass ejection cavity formation," *The Astrophysical Journal Letters*, vol. 862, no. 2, p. L15, 2018.